The Dissertation Committee for SANGWOOK HAN Certifies that this is the approved version of the following dissertation:

Antenna Coupled Infrared Detectors
For Wavelength Selectivity or Broadband Absorption

Committee:

Dean P. Neikirk, Supervisor

Francis X. Bostick

Mircea Driga

Archie Holmes

John T. McDevitt

ANTENNA COUPLED INFRARED DETECTORS FOR WAVELENGTH SELECTIVITY OR BROADBAND ABSORPTION

by

SANGWOOK HAN, M.S.E.E., B.S.E.E.

DISSERTATION

Presented to the Faculty of the Graduate School of
The University of Texas at Austin
in Partial Fulfillment
of the Requirements
for the Degree of

DOCTOR OF PHILOSOPHY

The University of Texas at Austin
May 2006

Acknowledgements

During my time at UT as a graduate student, I have been very fortunate to have had the opportunity to work with people, Team Neikirk who are outstanding individuals both personally and professionally, and I would like to thank them for their help during my time here at UT. This group has almost always been a lot of fun, and has almost always been supportive of my efforts. Within this group I must extend special thanks to Jooyong Kim, Byungki Woo, Junwan Kim, Yoonsuk Park, Matthew Andringa, Praveenkumar Pasupathy, and Joo-Yun Jung. I would like to thank my supervising professor, Dr. Dean P. Neikirk, to whom I am deeply indebted and whose creative insights and suggestions contributed immeasurably to this work.

I wish to thank the members of my committee; Dr. Francis X. Bostick, Dr. Mircea Driga, Dr. Archie Holmes, Dr. John T. McDevitt, and Dr. Joe Campbell, for their patience and support and would like to commend them for their inspirational teaching and excellence in their respective fields.

I would like to thank my parents, Dalsoo Han and Soonja Bae, for their continued enthusiastic support of my education, and parents-in-law, Balkyu Lee and Gumja Park for their encouragement and support. I want to let my son, Taekyung Han, know that I love him dearly and believe in him and his capabilities. I would finally like to thank my wife Jinhee Lee whose support, love, and help made much of this work possible. Her encouragement to me has always been invaluable.

Antenna Coupled Infrared Detectors For Wavelength Selectivity or Broadband Absorption

Publication No._____________

Sangwook Han, Ph.D.
The University of Texas at Austin, 2006

Supervisor: Dean Paul Neikirk

An approach for designing antenna coupled infrared detectors (planar multimode detectors) for wavelength selectivity, and dielectric coated Salisbury Screen and Jaumann Absorber for wavelength selectivity and broad band absorption is presented. Calculations of electromagnetic behaviors of the designs and verifications are presented. These structures offer the possibility of wavelength selectivity or broad band absorption by tailoring its spectral responses. They also offer the possibility of increasing compactness to save space. We present diverse designs to achieve multi-color imaging, bolometers in parallel, vertically stacked bolometers, tuning by changing the distance between bolometric layer and mirror, tuning by lithographically drawn parameters, and so on. We also present thermally improved bolometer arrays to improve responsivity, detectivity, *NEP*, speed, and so on.

Table of Contents

Chapter 1 Microbolomemter Theory 1

1.1 History of Bolometers 1

1.2 Basic Parameters of Bolometers 9

1.2.1 Temperature Coefficient of Resistance (*TCR*) 9

1.2.2 Responsivity 10

1.2.3 Johnson Noise 11

1.2.4 Noise Equivalent Power (*NEP*) 11

1.2.5 Detectivity 12

1.2.6 Noise Equivalent Temperature Difference (*NETD*) 12

1.2.7 Bias Current 17

1.2.8 Power Absorption Efficiency 18

1.3 Thermal Models 19

1.4 Multi-Spectral Microbolometers 23

Chapter 2 Planar Multimode Detector 24

2.1 Multimode Array 24

2.2 Electrical Models 26

2.3 Verification of Eisenhart and Khan Model by HFSS 44

Chapter 3 Wavelength Selective Planar Multimode Detectors 51

3.1 Introduction of Wavelength Selectivity 51

3.2 Genetic Algorithm (GA) 54

3.3 Tuning of Wavelength Selectivity By Mechanical Actuation 56

3.4 Design for Wavelength Selectivity 59

3.4.1 Different Sacrificial Layer Thickness for 3 Different Pixels 59

3.4.2 Same Sacrificial Layer Thickness for 3 Different Pixels 62

Chapter 4 Uncooled and Stacked Microbolometer Array for Multi-Spectral Imaging 65
4.1 Introduction 65
4.2 Stackable Planar Multimode Detectors 66
4.3 Stacked Planar Multimode Detectors 70

Chapter 5 Broad Band Or Wavelength Selective Salisbury Screens And Jaumann Absorbers 75
5.1 Dielectric Coated Salisbury Screen For Broad Band Absorption 75
5.2 Dielectric Coated Jaumann Absorbers For Broad Band Absorption 79
5.3 Dielectric Coated Salisbury Screens 81
5.4 Tuning Of Salisbury Screens By Varying Air Gap 83
5.5 Wavelength Selective 2-Color Jaumann Absorbers 87
5.6 Wavelength Selective 3-Color Jaumann Absorbers 91

Chapter 6 Modified Planar Multimode Detectors for High Sensitivity 94
6.1 Simple Thermal Models 96
6.2 Thermal Model for the Temperature Profile 100
6.2.1 Temperature Rise Due to IR Power Absorption 100
6.2.2 Temperature Rise Due to the Bias Heating 102
6.2.3 Temperature Rise Due to IR Power Absorption and Bias Heating 105
6.3 Characteristics of the Modified Planar Multimode Detectors 107
6.3.1 Characteristics of Microbolometer When N=1 108
6.3.2 Characteristics of Microbolometer When N=3 110
6.3.3 Characteristics of Microbolometer When N=9 112
6.4 Numerical Results 113

Chapter 7 Conclusions 116

Appendix A Planar Multimode Detector with a Mirror (MatLab Code)..........119

References 122

Vita 128

List of Tables

Table 1.1: Applications of infrared imaging systems 3

Table 1.2: List of basic pamameters of bolometers 9

Table 1.3: Temperature coefficient of resistance (*TCR*) of materials...............10

Table 2.1: Specific designs yielding response curves given in Figure 2.8 37

Table 2.2: GA-optimized designs of Salisbury Screen (Figure 2.9) for broad band absorption in 3~13μm band. These results reveal that ‘thin conductors’ are better than ‘lossy dielectrics’ as bolometric material from the perspective of broad band absorption. Refer to Figure 2.9 for their spectral responses...41

Table 3.1: Specific designs yielding response curves given in Figure 3.8 61

Table 5.1: Specific designs yielding responses given Figure 5.1. d_1 and d_2 are thicknesses of the support layer and an air gap. 78

Table 5.2: Specific designs yielding responses given Figure 5.6. d_1 and d_2 are thickness of Ge support layers, and d_3 is thickness of an air gap (refer to Figure 5.2 (a)). 83

Table 5.3: Figure of merits for wavelength selectivity of spectral responses shown in Figure 5.7. 'In-band integrated efficiency' is integrated efficiency in target wavelength ± 1μm band, and 'Selectivity' is 'in-band integrated efficiency' to 'out-of-band integrated efficiency' ratio. Based on the 'Selectivity', designs with 2.0μm and 7.6μm air gap have poor wavelength selectivity. 85

Table 5.4: Figure of merits for wavelength selectivity of spectral responses shown in Figure 5.8 (b). 'In-band integrated efficiency' is integrated efficiency in target wavelength ± 1μm band, and 'Selectivity' is 'in-band integrated efficiency' to 'out-of-band integrated efficiency' ratio. From the comparison of 'Selectivity' in Table 5.3 (Figure 5.7) and that in Table 5.4 (Figure 5.8 (b)), the designs in Figure 5.8 (b) show much better wavelength selectivity. 86

Table 5.5: Specific designs yielding responses given Figure 5.8 (b). d_1 and d_2 are thickness of Ge support layers, and d_3 is thickness of an air gap (refer to Figure 5.8 (a)). 87

Table 5.6: Specific designs yielding responses given Figure 5.10. (refer to Figure 5.2 (b) for notation). 89

Table 5.7: Specific designs yielding responses given Figure 5.14. (refer to Figure 5.2 (c) for notation). 93

Table 6.1: Numerical results of three modified planar multimode detectors (N=1, 3, and 9) when the bias currents are fixed for all three cases. 114

Table 6.2: Numerical results of three modified planar multimode detectors (N=1, 3, and 9) when each design has the maximum bias current, $I_{b,max}$. . 115

List of Figures

Figure 1.1: Application of infrared thermal imaging. (a) Night operation. (b) Battlefield assessment. (c) Nondestructive inspection. (d) Medical diagnostics. 5

Figure 1.2: Industrial configuration of uncooled infrared detector manufacturer in the United States. 7

Figure 1.3: Plot of integrated blackbody power as a function of temperature; solid: integrate Plank's law over LWIR, 8~14μm; dotted: integrate MWIR, 3~5μm. 14

Figure 1.4: Plot of *dP*/*dT* as a function of temperature; solid: integrate LWIR, 8~14μm; dotted: integrate MWIR, 3~5μm. 15

Figure 1.5: Plot of *dP*/*dT* as a function of temperature; solid: integrate LWIR, 8~14μm; dotted: LWIR *dP*/*dT* for 300K; dash-dot-dot: integrate MWIR, 3~5μm; dash-dot: 5~8μm integration; dotted: 3~14μm integration; dashed: integrate over all wavelengths. 16

Figure 1.6: Microbolometer pixel structure consisting of sensing element, thermal links, and heat sink. 20

Figure 1.7: Simple thermal models of the thermal link 20

Figure 1.8: Temperature and power in phase at low frequency. 22

Figure 1.9: Temperature and power out of phase (45º) at high frequency. 23

Figure 2.1: Air-bridge microbolometer combined with bow-tie antenna 24

Figure 2.2: (a) Single mode antenna with a point source. $P=S\cdot A_e$. (b) A multimode antenna can be used to collect a large amount of power from distributed sources. $P=n\cdot k_B\cdot T$. 26

Figure 2.3: (a) Configuration of a period of the planar multimode detector, consisting of a grid of wide metal sheets connected by narrow resistive bolometer layers. (b) Array of cells. 28

Figure 2.4: Equivalent transmission line models of the planar multimode detector shown in Figure 2.3. 29

Figure 2.5: Configuration of a pixel of the planar multimode detector. 35

Figure 2.6: Configuration of a pixel with supportive layers and legs on the substrate. 35

Figure 2.7: Focal plane array (FPA) using the planar multimode detectors. 36

Figure 2.8: Design of multimode detectors with unity absorption at center wavelength 10μm, but widely varying bandwidths. Bandwidth can be wide as the Salisbury Screen (dashed line), and narrow enough to construct multiple channels within the 7~14μm IR band (solid line). All specific design geometries are given in Table 2.1. 37

Figure 2.9: Broad band absorptions by 'thin conductors' (solid curve, design 1 in Table 2.2) and 'lossy dielectrics' (dashed and dotted curves). The dashed curve (design 9 in Table 2.2) is the broadest but simulated with unrealistic dielectric constant. From the comparison between the solid (thin conductors) and dotted (lossy dielectrics, design 15 in Table 2.2) curves, 'thin conductors' are better than 'lossy dielectrics' as bolometer layers for broad band absorption. 38

Figure 2.10: Transmission model when a pland wave strikes a finite thick layer in between free space. 42

Figure 2.11: Transmission model approximately equivalent with the model in Figure 2.9. Finite thick bolometer layers can be represented by the infinitely thin conductive sheets. 44

Figure 2.12: (a) HFSS configuration designed to generate a resonance at 30THz. (b) The HFSS-simulated results (solid curve) show good resonance at 30THz, in agreement with the simple transmission line plane wave model (dashed curve). 46

Figure 2.13: HFSS simulation (solid curve) of an array with period a=6.9μm, resistive post width w=6.0μm, gap g=6.0μm, and air gap thickness d=2.5μm; this is almost the same as simple Salisbury screen. Agreement between Eisenhart and Khan (dashed curve) and HFSS (solid curve) is good. 47

Figure 2.14: HFSS simulation of an array with wavelength selectivity, period a=5.3μm, gap g=1.0μm, resistive post width w=0.96μm, distance to mirror d=3.61μm, and bolometer sheet resistance R_S=30Ω; agreement between 'Eisenhart and Khan' and 'HFSS' is again reasonably good. 48

Figure 2.15: HFSS simulation (solid curve) of an array with wavelength selectivity compared to calculations from the Eisenhart and Khan model (dashed curve), both compared to conventional Salisbury screen (dotted curve). This full-wave finite element calculation confirms the grid produces wavelength selectivity. 49

Figure 2.16: HFSS simulation of an array with and without a resistive element; the dip in the red curve is the wavelength selective absorption of power by the bolometric element. 50

Figure 3.1: Salisbury Screens. (a) Standard 50µm bridge. (b) 39µm bridge for high density linear array. 52

Figure 3.2: Ideal power absorption efficiencies for 3-color detection in 7~14µm band 54

Figure 3.3: Block diagrams of the simple Genetic Algorithm 55

Figure 3.4: Tunable wavelenth selective focal plane array using the planar multimode detectors by mechanical actuation..................................57

Figure 3.5: The contour plots of the power absorption efficiencies versus wavelength and the distance to the mirror *d*. Tuning wavelength selectivity can be achieved by mechanical actuation. Here *a*, *g*, *w*, and R_s are 6.90µm, 0.20µm, 3.0µm, and 53.49Ω, respectively. 57

Figure 3.6: Successful accomplishment of the wavelength selectivity tuning by only changing the distance to the mirror *d*, which can be achieved by the simple actuation, on the planar multimode detectors with same *a*, *g*, *w*, and R_s: *a*=5.07µm, *g*=1.42µm, *w*=0.74µm, and R_s=21.04Ω. 59

Figure 3.7: Pixels located in parallel for wavelength selectivity which does not require mechanical actuation. (a) Perspective view. (b) Front view. 60

Figure 3.8: Three-color design found by optimizing three different multimode pixel geometires, each with different lighographically drawn dimensions *a*, *g*, and *w*, *d*, and R_s. Power absorption efficiencies are almost unity at designated wavelengths while each pixel would have enough wavelength selectivity to clearly distinguish three colors. All specific design geometries are given in Table 3.1. 61

Figure 3.9: Pixels located in parallel for wavelength selectivity which does not require mechanical actuation. (a) Perspective view. (b) Front view. 64

Figure 3.10: Three-color design found by optimizing three different multimode pixels in Figure 3.9, each with different lithographically drawn dimensions *a*, *g*, and *w*, with identical *d* and R_s. *a*, *g*, *d*, and R_s are 6.80μm, 0.20μm, 3.14μm, and 56.6Ω, respectively. 64

Figure 4.1: (a) Schematic view of stacked quantum well infrared photo-detectors (QWIP). (b) Top view of 2-color focal plane array pixels. 66

Figure 4.2: Planar multimode detector without a mirror. 68

Figure 4.3: Transmission line model of the geometry in Figure 4.2 when the planar multimode detector without the mirror is located in between the free space. 68

Figure 4.4: Ideal power absorption efficiencies for in-band absorption and out-of-band transmission using the configuration in Figure 4.2. These are assumed for 2-color detection. Notice that maximum power absorption efficiency is 0.5. 69

Figure 4.5: Spectral response of the planar multimode detector without a mirror. The solid, dashed, and dotted lines are power absorption efficiency, power transmission efficiency, and power reflection efficiency, respectively. (*a*=6.9µm, *g*=3.5µm, *w*=2.5µm, R_s=60Ω) 69

Figure 4.6: Stacked planar multimode detectors for the 2-color wavelength selectivity. Each layer absorbs its own designated wavelength band. 70

Figure 4.7: Transmission line model of the stacked planar multimode detectors in Figure 4.6. 71

Figure 4.8: Two-color design found by optimizing stacked two different planar multimode detectors. Power absorption efficiencies are strong at the designated center wavelengths while each stacked multimode array would have enough wavelength selectivity to clearly distinguish two colors, a_1, g_1, w_1, R_{s1}, d_1, a_2, g_2, w_2, R_{s2}, and d_2 are 5.85µm, 4.25µm, 3.98µm, 980.9Ω, 2.10µm , 5.74µm, 3.38µm, 0.35µm, 37.4Ω, 4.25µm, respectively. 73

Figure 4.9: Design of two-spectral infrared detection using the conventional Salisbury Screens located in parallel. The solid line is designed to absorb a band centered at 8.5µm wavelength while the dashed line is designed to absorb a band centered at 12.5µm. It is not suitable for the wavelength selectivity because of the ambiguity of absorbed wavelengths over 7 to 9µm and 10 to 12µm. The sheet resistance of the absorption layer for both microbolometer is 377Ω, and the distance to the mirror for 8.5µm and 12.5µm center wavelengths are 6.38µm and 9.38µm, respectively. 74

Figure 5.1: Effects of supporting material on broad band absorption of bolometric layer. Corresponding GA-optimized integrated efficiencies to $\varepsilon'=1, 4, 8, 12$, and 16 (Germanium) are 88%, 88%, 86%, 83%, and 80% (Germanuium), respectively. As ε' goes up, broad band absorption deteriorates. The thick solid curve is broad band absorption without a support layer providing 88% of integrated efficiency. 76

Figure 5.2: Configuration of broad band or wavelength selective pixels: (a) Dielectric-coated Salisbury Screen; (b) Two color dielectric-coated Jaumann Absorber; (c) Three color dielectric-coated Jaumann Absorber. 77

Figure 5.3: GA-optimized Salisbury Screens supported by lossy Si_3N_4 layer. Absorption by Si_3N_4 (dotted line) due to Si-N stretching vibrations deteriorates the absorption by the bolometric layer (dashed line) especially in a long wavelength region in a given range. The solid line is the sum of power absorption by both the bolometric layer and Si_3N_4 support layer. R_s, d_1, and d_2 are 320Ω/□, 0.1μm, and 1.2μm, respectively. Integrated efficiency = 88%. Solid: absorbed by the bolometric layer. Dotted: absorbed by the lossy Si_3N_4 support layer. 79

Figure 5.4: Optimized power absorption efficiencies of dielectric-coated Jaumann Absorbers producing integrated absorption of 93% over the 3~13μm band...80

Figure 5.5: Salisbury Screens located in parallel for 2-color infrared detection. (a) Perspective view. (b) Front View. 82

Figure 5.6: GA-optimized designs to absorb 3 colors centered at 8, 10, and 12μm wavelengths. Dashed, solid, and dotted curves are from calculations using the ABCD transmission line matrix method. Polygons are from Ansoft HFSS. 82

Figure 5.7: Tuning of the design illustrated in Figure 5.6 (solid line) by varying air gap thickness. From the perspective of multi-color wavelength selectivity, these are very poor designs. The dotted line is tuned to absorb 8μm wavelength by varying d_3 from 5.0μm to 2.0μm. The dashed line is tuned to absorb 12μm wavelength by varying air gap thickness d_3 from 5.0μm to 7.6μm. Here d_1=2.5μm, R_{s1}=459Ω/□, d_2=0.6μm, d_{31}=2.0μm, d_{32}=5.0μm, and d_{33}=7.6μm (refer to Figure 5.8 (a) for the notations). 84

Figure 5.8: Tunable Salisbury Screen. To achieve tuning of absorption wavelength, thicknesses of Ge support layers are fixed for all three designs prepared to absorb 8, 10, and 12μm wavelengths. (a) Configuration. (b) Spectral responses of optimized designs. Dashed, solid, and dotted curves are calculated from ABCD matrix analysis. Polygons are calculated from Ansoft HFSS and provided as verification of ABCD matrix analysis. 85

Figure 5.9: Jaumann Absorber for 2-color wavelength selectivity. Each layer absorbs its own designated wavelength band. 88

Figure 5.10: GA-optimized vertically stacked pixels to absorb 2 colors centered at 8.5 and 12.5μm wavelengths. Solid: absorbed by top absorbing layer. Dashed: absorbed by bottom absorbing layer. 88

Figure 5.11: Sum of power absorption by the design described in Figure 5.10. Solid curve is calculated using the ABCD matrix analysis, and circles are from Ansoft HFSS calculations. 89

Figure 5.12: 2-color design found by optimizing Jaumann Absorbers in 3~5μm wavelengths, mid IR band. 90

Figure 5.13: 2-color design found by optimizing Jaumann Absorbers in 3~13μm wavelengths, mid and long IR band. One color is for mid IR band, 3~5μm, and the other is for long IR band, 8-12μm. 91

Figure 5.14: GA-optimized vertically stacked pixels to absorb 3 colors centered at 8, 10, and 12μm wavelengths. Dotted: absorbed by top pixel. Solid: absorbed by middle pixel. Dash-dotted: absorbed by bottom pixel. 92

Figure 5.15: Sum of power absorption by the design described in Figure 5.14. Solid curve is calculated using ABCD matrix analysis, and circles are simulated from Ansoft HFSS for verification. 93

Figure 6.1: Air-bridge microbolometer when *N*=1, where *N* is the number of thermal sources along each absorbing resistive bar. 95

Figure 6.2: Air-bridge microbolometer when *N*=3. 95

Figure 6.3: Air-bridge microbolometer when *N*=9. 96

Figure 6.4: Simple thermal model of the air-bridge bolometer with only conduction path to the heat sinks. 97

Figure 6.5: Temperature rise $\phi(x)$ along a bar. The bolometer material is Bismuth and *l* is 2.4μm, *w*=1.0μm, and *t*=0.1μm. 98

Figure 6.6: Thermal model for the air-bridge resistive bar in Figure 6.2. 101

Figure 6.7: Electrical model for the air-bridge resistive bar converted from the thermal model in Figure 6.6. 101

Figure 6.8: Discretized resistive bar to consider the feedback temperature rise due to temperature dependent conductivity. 103

Figure 6.9: Temperature profile along the bar due to IR power absorption and the bias heating. Temperature dependent conductivity has been considered. 107

Figure 6.10: Equivalent electrical model of the grid part in Figure 6.1. The air-gap between absorbing resistive sheets and metal can be represented as the capacitor C_{air}. 108

Figure 6.11: Equivalent circuit model representing the interwoven grid of the thermally improved planar multimode detectors when N=1. The whole geometry including the mirror is shown in Figure 6.1. 110

Figure 6.12: Three areas along each resistive bar are thermally heated due to the antenna structure, i.e. N=3. Focused and detailed from Figure 6.2. 111

Figure 6.13: Equivalent circuit model of the thermally improved planar multimode detectors shown in Figure 6.2. 111

Figure 6.14: Nine areas along each resistive bar are thermally heated due to the antenna structure, i.e. N=9. Focused and detailed from Figure 6.3. 113

Chapter 1: Microbolometer Theory

1.1 HISTORY OF BOLOMETERS

There are currently a large number of optical sensors whose spectral ranges span from the *x*-ray range to the far infrared region. In the visible region, silicon semiconductor systems dominate the sensor field. For example, Charge Coupled Devices (CCDs) are now available commercially which exhibit extraordinarily high sensitivity values and large dynamic ranges. When combined with color selective filters, these CCD systems exhibit spectral response features similar to those exhibited by the human eye. Unfortunately, the band gap limitation of silicon precludes its use for wavelengths greater than ~1.1μm. However, for a number of important applications as shown in Table 1.1 and Figure 1.1, it would be desirable to create sensor arrays which display the capacity to respond to infrared (IR) wavelengths.

The origins of modern infrared sensing technology date back to anti-missile defense of World War II and its evolution as well as the associated development of IR materials continues to be driven primarily by military need to see the battlefield at night without the need for any form of illumination, whether from natural (moonlight, starlight, etc.) or artificial sources. In the U.S., it was the Vietnam War that caused the military services to develop a means of tracking thermal emissions from terrain, vehicles, buildings and people. The result was the Common Modular FLIR system (developed by what is now the U.S. Army CECOM Night Vision and Electronic Sensors Directorate), which was based on linear arrays of HgCdTe pixels cooled to 77K [1].

Methods for detecting infrared radiation fall into two major categories – photon detection and thermal detection. According to Rogalski [2], since about 1930 the development of IR technology has been dominated by the photon detectors such as cryogenically cooled semiconductor devices (HgCdTe, InSb, GaAs/AlGaAs, PtSi, etc), in which the absorption of an IR photon of sufficient energy frees an electron or hole or both to increase electrical conductivity or to generate a voltage at a potential barrier internal to the material. They can provide higher sensitivity and a faster response time than the thermal detectors. However, the photon detectors require cryogenic cooling to prevent the thermal generation of charge carriers. The thermal transitions compete with the optical ones, making non-cooled devices very noisy. The cooled thermal camera usually uses a helium Sterling cycle cooler, which is the most expensive component in the photon detector IR camera, and the cooler's life time is only around 2000 hours [2]. Cooling requirements are the main obstacle to the widespread use of IR systems based on semiconductor photon detectors, making them bulky, heavy, expensive, and inconvenient to use.

In contrast to photon detection, thermal detection relies on the increase in temperature of a material upon absorbing incident IR radiation, which can be detected by a change in electrical conductivity (resistance bolometer), generation of a voltage (thermoelectric effect, thermocouple), change in the electrical polarization (pyroelectric effect), or movement of a surface (Golay cell). Although these effects are much slower than photon detection mechanisms, they do not require cryogenic operation, since the dark current resulting from the thermal generation of charge carriers in photon detectors does not affect them.

Military, Law Enforcement, and Rescue	Industrial	Medical (Figure 1.1 (d))	Scientific
• Night operations (Figure 1.1 (a)) • Reconnaissance and surveillance • Fire fighting and rescue in smoke • Submarine detection • Detect underground missile sites, personnel, vehicles, weapons, mines and encampments • Damage assessment • Night-time landing aids • Missile guidance and proximity fusing	• Industrial surveillance and crime prevention • Process control • Nondestructive inspection of manufacture items such as thermal insulators, photographic film and infrared materials (Figure 1.1 (c)) • Hidden piping location • Microwave field display • Diseased tree and crop detection	• Early detection and identification of cancer • Optimum site for amputation determination • Placental site location • Efficiency of arctic clothing studies • Early diagnosis of incipient stroke and vein blockage • Wound healing monitoring • Onset of infection detection without removing bandages	• Satellite earth resource surveying • Gulf stream location and mapping • Volcano studies • Water pollution detection and studies • Crevasse and sea-ice reconnaissance studies • Crop detection • Forgery detection • Nocturnal animal studies • Remote sensing of weather conditions • Heat transfer in plant studies

• Earthquake victim locations • Hidden law violator location • Forest fire detection • Battle field assessment (Figure 1.1 (b))	• Hot spot detection, e.g., hot boxes on railroad cars and power lines • Brake lining, cutting tool, weld and ingot temperature measurement • Clear-air turbulence detection • Organic chemicals and gas analysis • Pipeline leak detection • Oil spill detection		• Earth’s heat balance measurements • Farming techniques improvements

Table 1.1: Applications of infrared imaging systems [3].

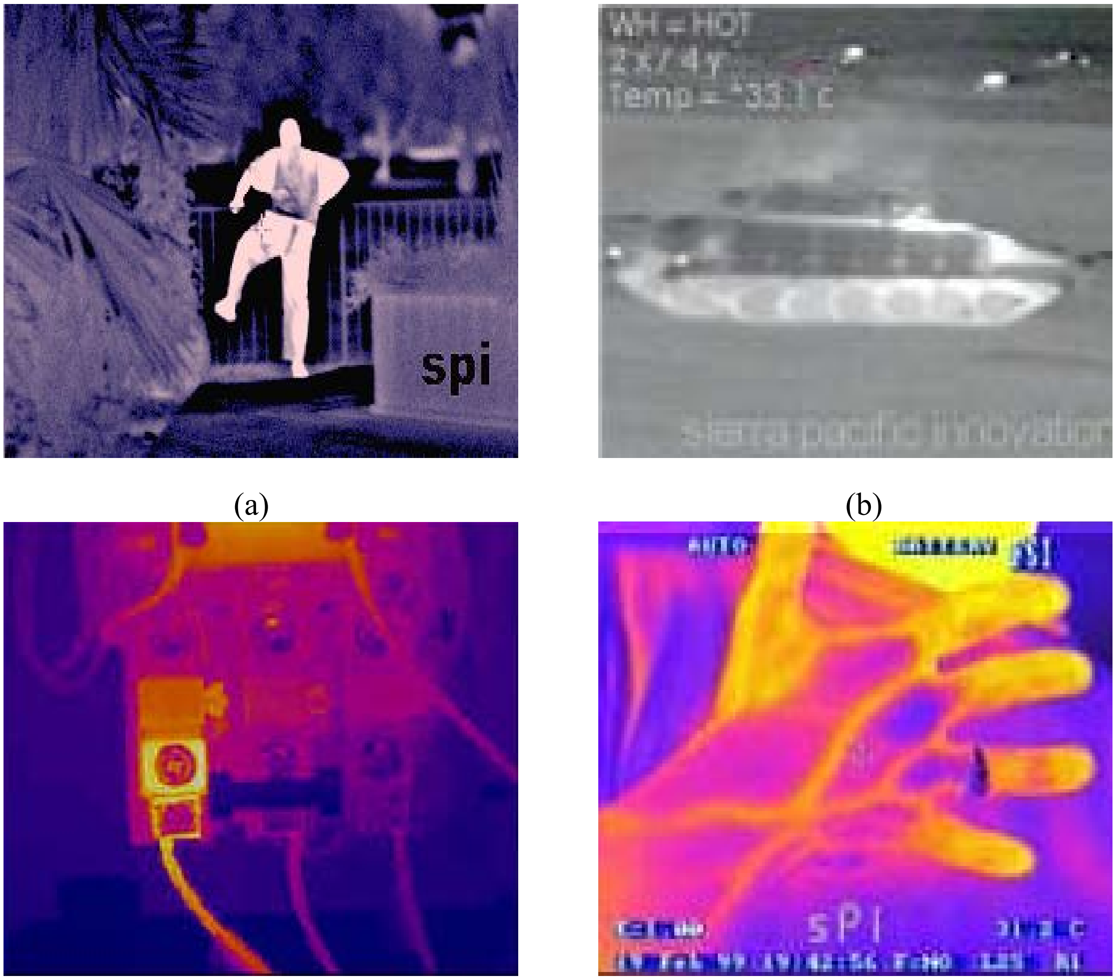

(a) (b)

(c) (d)

Figure 1.1: Application of infrared thermal imaging [4]. (a) Night operation. (b) Battlefield assessment. (c) Nondestructive inspection. (d) Medical diagnostics.

The use of thermal detectors for IR imaging has been the subject of research and development for many decades (Figure 1.2). However, in comparison with photon detectors, thermal detectors have been considerably less exploited in commercial and military systems. The reason for this disparity is that thermal detectors are popularly believed to be rather slow and insensitive in comparison with photon detectors. As a result, the worldwide effort to develop thermal detectors has been extremely small relative to that of photon detectors. Recently, however, it has been shown that extremely good imagery can be obtained from large thermal detector arrays operating uncooled at TV frame rates [2]. In contrast to photon detectors, which are sensitive only to wavelengths shorter than the cutoff, thermal detectors such as a conventional bolometer are, in principle, sensitive to all wavelengths. The absorption of light raises the temperature of the device and this in turn results in changes in a temperature-dependent parameter such as electrical conductivity. As a consequence, the output of a conventional bolometer is usually proportional to the amount of energy absorbed per unit of time by the detector and, provided the absorption efficiency is the same for all wavelengths, is independent of the wavelength of the light. In addition, dark current does not limit thermal detectors. Therefore, they can be operated inexpensively at room temperature. Room temperature microbolometers arrays have become widely available for use in infrared imaging systems. The use of micromachining to reduce thermal mass and increase thermal resistance, combined with a CMOS compatible process, has allowed the development of sensitive, large pixel count, low cost focal plane imaging arrays. However, these arrays have provided only thermal information. Even though some of the images from these arrays are colored like Figure 1.1 (c) and (d), those colors have no special meaning except how hot the objects are. For instance, white, red, green, blue, black may represent how hot they are in the order of temperature. Therefore, these arrays are actually mono-colored. On the other hand, multi-spectral arrays can provide information of both temperature and spectral signatures. The spectral signatures can help to determine the presence of specific molecules. Therefore, the colors of multi-spectral arrays have real meaning unlike those of conventional arrays. Multi-spectral arrays will be discussed in Chapter 3 in detail. The development of tunable multi-spectral capability with functionality in the infrared region would have a profound influence on a number of military/civilian applications. The speed of thermal detectors is quite adequate for non-scanned images with two-dimensional detectors. The thermal detectors are classified according to the operating scheme: bolometer scheme, thermopile scheme, and pyroelectric scheme.

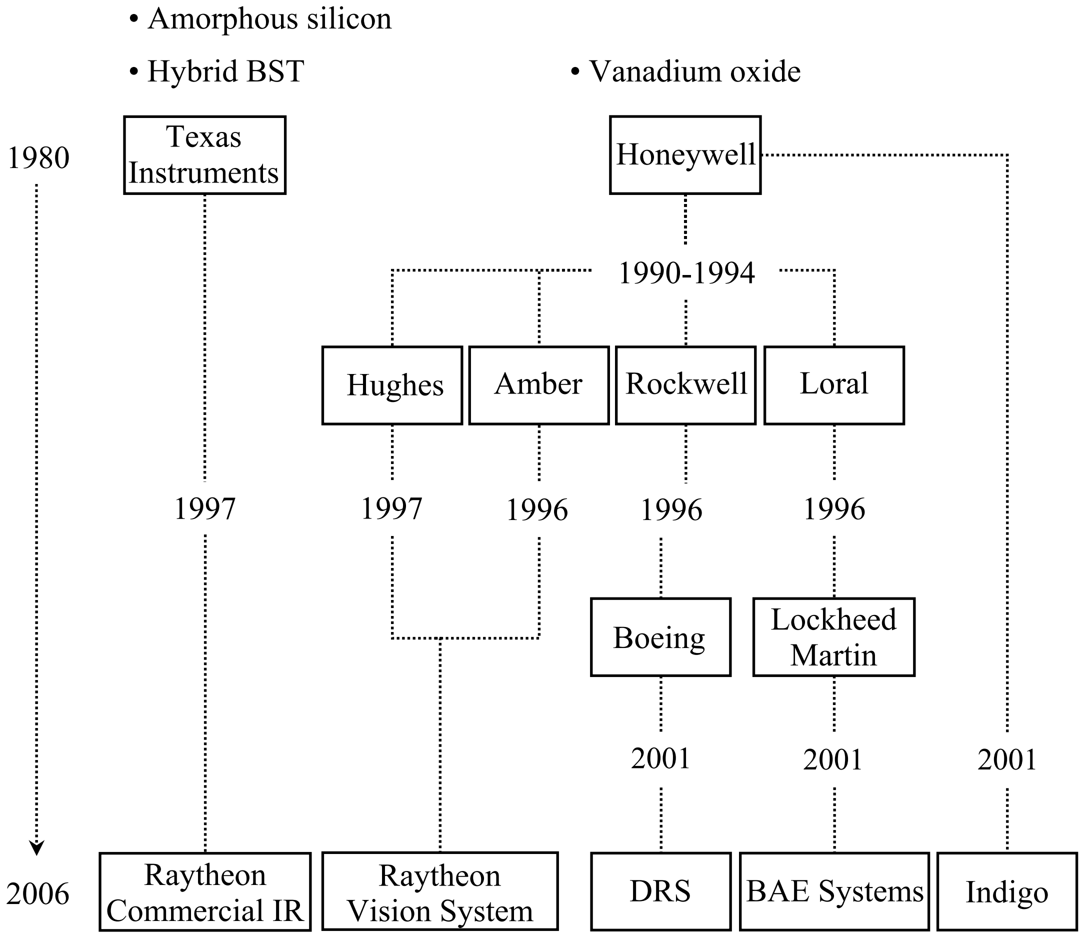

Figure 1.2: Industrial configuration of uncooled infrared detector manufacturer in the United States [5].

The bolometer is a resistive element constructed from a material with a large temperature coefficient of resistance so that the absorbed radiation produces a large change in resistance. The device is typically operated by passing an accurately controlled bias current through the detector, and monitoring the output voltage. The change in resistance is like to the photoconductor, however, the basic detection mechanisms are different. In the case of a bolometer, radiant power produces heat within the material, which in turn produces the resistance change. There is no direct photo-electron interaction. The first bolometer designed in 1880 by American astronomer S. P. Langley for solar observations [6], used a blackened platinum absorber element and a simple Wheatstone-bridge sensing circuit. Although other thermal devices have been developed since that time, the bolometer remains one of the most used infrared detectors.

Originally the term microbolometer was referred to bolometers that were smaller than a wavelength. To increase thermal resistance, decreasing the cross sectional area and increasing the length of the thermal link is required. Microbolometer design can be separated into two parts. One is optimizing the sensing of resultant temperature, and the other is the absorption of radiation. In an ideal device, the absorber must provide total absorption of the incoming radiation and, furthermore, it must convert the electromagnetic radiation into heat.

1.2 BASIC PARAMETERS OF BOLOMETERS

Name	Unit	Parameter
detectivity	$cm\sqrt{Hz}\,/\,W$	D^*
Johnson noise	V	$V_{Johnson}$
noise equivalent power	W	NEP
noise equivalent temperature difference	K	$NETD$
responsivity	V/W	$\Re$
temperature coefficient of resistance	K^{-1}	α
thermal capacity	J/K	$C_{thermal}$
thermal resistance	K/W	$R_{thermal}$
thermal time constant	sec	τ
bias current	A	I_b
power absorption efficiency		η

Table 1.2: List of basic parameters of bolometers.

1.2.1 Temperature Coefficient of Resistance (*TCR*)

The simple analysis of bolometers assumes that the temperature increase ΔT of the bolometer due to the absorption of IR radiation is small enough that the resistance change ΔR is linear with ΔT, that is

$$\Delta R = R_{bol}\Delta T \qquad \text{Eq. 1.1}$$

where R_{bol} is the bolometer resistance. It is possible to express the change in resistance in terms of α, the temperature coefficient of resistance. Thus

$$\Delta R = \alpha R_{bol}\Delta T \qquad \text{Eq. 1.2}$$

where

$$\alpha = \frac{1}{R_{bol}} \frac{dR_{bol}}{dT} = \frac{1}{\rho_{bol}} \frac{d\rho_{bol}}{dT} \qquad \text{Eq. 1.3}$$

where ρ_{bol} is the bolometer material resistivity. The temperature coefficient of resistance (*TCR*) α is the relative change of the resistance of a material for a given change in temperature. *TCR* can be either positive or negative. A positive value of α indicates that R increases with temperature, and a negative value of α indicates R decreases with temperature; and zero α indicates that R is constant regardless of temperature. For typical metals at room temperature α is positive. For semiconductors at room temperature it is usually negative. For superconductors at their transition edge (superconducting bolometers), which even for high temperature superconductors is well below 300K, it is positive [3]. The followings are *TCR*s of some materials.

Materials	α [K^{-1}]
Vanadium Oxide (VO_x)	-0.02 ~ -0.03 [8-9]
Semiconducting YBCO	-0.0299 ~ -0.0337 [10-11]
Y-Ba-Cu-O (YBCO)	0.5 ~ 1
Ag	0.0037
Ni	0.005
Au	0.0036
Bi	-0.003

Table 1.3: Temperature coefficient of resistance (*TCR*) of materials.

1.2.2 Responsivity

The responsivity $\Re$ of an IR pixel is defined as the output signal (voltage or current) divided by the input radiant power falling on the pixel. Assume that the output signal is voltage *V*. Then the output voltage (*ΔV*) due to the spectral radiant incident power ($P_{incident}$) is determined as

$$\Delta V = I_b \cdot \Delta R = I_b \cdot \frac{dR}{dT} \cdot \Delta T = I_b \cdot \frac{dR}{dT} \cdot \frac{dT}{dP} \cdot P_{absorbed} \qquad \text{Eq. 1.4}$$

where I_b is the bias current through the pixel, and *ΔR* is the difference of the electrical resistance due to the incident IR power. The responsivity (exactly voltage responsivity $\Re_v$) is given by

$$\Re = \frac{\Delta V}{P_{incident}} = I_b \cdot \frac{dR}{dT} \cdot \frac{dT}{dP} \cdot \frac{P_{absorbed}}{P_{incident}} = I_b \cdot \left(\alpha \cdot R_{bolo}\right) \cdot Z_{thermal} \cdot \eta \qquad \text{Eq. 1.5}$$

The responsivity depends on the bias current I_b, temperature coefficient of resistance α, bolometer resistance R_{bolo}, device thermal impedance $Z_{thermal}$, and coupling efficiency η.

$$Z_{thermal} = \frac{dT}{dP} \qquad \text{Eq. 1.6}$$

$$\eta = \frac{P_{abs}}{P_{inc}} \qquad \text{Eq. 1.7}$$

1.2.3 Johnson Noise

The true measure of a detector’s performance is how well it extracts a signal from the surrounding noise. Johnson noise is associated with bolometer resistance and is a result of random movement of charge carriers in a resistor. Since electron movement increases with temperature, Johnson noise is also called thermal noise. For a simple resistive bolometer the lowest noise level is Johnson noise defined as

$$V_{johnson} = \sqrt{4k_B \cdot T \cdot R_{bolo} \cdot BW} \qquad \text{Eq. 1.8}$$

where *BW* is the post detection bandwidth.

1.2.4 Noise Equivalent Power (*NEP*)

Figure of merit is really the minimum detectable input power named noise equivalent power (*NEP*) and is defined as

$$NEP = \frac{V_{noise}}{\Re} \approx \frac{\sqrt{4k_B \cdot T \cdot R_{bolo} \cdot BW}}{I_b \cdot Z_{thermal} \cdot \alpha \cdot R_{bolo} \cdot \eta} = \sqrt{4k_B \cdot T \cdot BW} \cdot \frac{1}{I_b} \cdot \frac{1}{\alpha\sqrt{R_{bolo}}} \cdot \frac{1}{Z_{thermal}} \cdot \frac{1}{\eta} \qquad \text{Eq. 1.9}$$

NEP is inversely proportional to the responsivity.

1.2.5 Detectivity

The detectivity *D* is the reciprocal of *NEP*.

$$D = \frac{1}{NEP} \qquad \text{Eq. 1.10}$$

It was found by R. C. Jones [12] that for many detectors the *NEP* is proportional to the square root of the detector signal that is proportional to the detector area. This means that both *NEP* and detectivity are functions of electrical bandwidth and detector. Therefore, a normalized detectivity D^* suggested by R. C. Jones is defined as

$$D^* = \frac{\sqrt{A_d \Delta f}}{NEP} \qquad \text{Eq. 1.11}$$

where A_d is a detector area. The importance of D^* is that this figure of merit permits comparisons of detectors of the same type, but having different areas.

1.2.6 Noise Equivalent Temperature Difference (*NETD*)

The noise equivalent temperature difference (*NETD*) is the smallest temperature change in object space that can be resolved assuming a unit signal to noise ratio. The power incident on a detector form a target at temperature T_t assuming emissivity=1:

$$P_0 = \frac{\tau_{lens}}{4 \cdot F^2} \cdot A_{detector} \cdot \left(\frac{dP}{dT}\right)_{\lambda 1-\lambda 2} \cdot T_t \qquad \text{Eq. 1.12}$$

where $A_{detector}$ is the area of the detector, *F* is the f number of the optics, τ_{lens} is the transmission of the optics, and $(dP/dT)_{\lambda 1-\lambda 2}$ is the slope of the function $P(T_t)$ where *P* is power radiated per unit area by a blackbody target within the spectral band from $\lambda 1$ to $\lambda 2$. The power needed to get 1:1 signal to noise is just the *NEP* multiplied by a term related to the post detection bandwidth *BW* (that sets the noise). Normally the lower limit for resistive devices is Johnson noise, in which case the noise is proportional to $(BW)^{1/2}$.

From this, if the NETD is the temperature of an object needed to produce this much power, then

$$NEP \cdot \sqrt{BW} = P_{\min} = \frac{\tau_{lens}}{4 \cdot F^2} \cdot A_{detector} \cdot \left(\frac{dP}{dT}\right)_{\lambda 1 - \lambda 2} \cdot NETD \qquad \text{Eq. 1.13}$$

or

$$NETD = \frac{NEP \cdot \sqrt{BW}}{\frac{\tau_{lens}}{4F^2} \cdot A_{decector} \cdot \left(\frac{dP}{dT}\right)_{\lambda 1 - \lambda 2}} = \frac{4F^2 \cdot NEP \cdot \sqrt{BW}}{\tau_{lens} \cdot A_{decector} \cdot \left(\frac{dP}{dT}\right)_{\lambda 1 - \lambda 2}} \qquad \text{Eq. 1.14}$$

NETD is in [*K*], $NEP \cdot \sqrt{BW}$ is power in [*W*], *F* and *τ* are both dimensionless; so $(dP/dT)_{\lambda 1 - \lambda 2}$ needs to be *W*/(*K·area*). In terms of *D**, since $NEP = \sqrt{area} / D*$, the NETD can also be expressed as:

$$NETD = \frac{4F^2 \cdot \left(\sqrt{A_{decector}} / D*\right) \cdot \sqrt{BW}}{\tau_{lens} \cdot A_{decector} \cdot \left(\frac{dP}{dT}\right)_{\lambda 1 - \lambda 2}} = \frac{4F^2 \cdot \sqrt{BW}}{\tau_{lens} \cdot \sqrt{A_{decector}} \cdot D* \cdot \left(\frac{dP}{dT}\right)_{\lambda 1 - \lambda 2}} \qquad \text{Eq. 1.15}$$

If we had a system that integrated over all wavelengths, then we could make use of the Stefan –Boltzman law to evaluate $(dP/dT)_{\lambda 1 - \lambda 2}$. The total power radiated from an object of area A_{object} at temperature T_{object} is

$$P_{total} = \sigma \cdot T^4 \cdot A_{object} \qquad \text{Eq. 1.16}$$

where $\sigma = 5.67 \times 10^{-8} watt/m^2 K^4$. For a “unit area” 300K object, this gives a total power of $4.59 \times 10^{-2} W \cdot cm^{-2}$.

If instead we integrate over only a finite range of wavelengths we will need to use Plank’s Law for the spectral irradiance *S* from a blackbody:

$$S = \frac{2 \cdot \pi \cdot c^2 \cdot h}{\lambda^5} \cdot \frac{1}{\exp\left(\frac{h \cdot c}{\lambda \cdot k \cdot T}\right) - 1} \qquad \text{Eq. 1.17}$$

(unit: watts/are per $\delta\lambda$, where $\delta\lambda$ is the bandwidth, i.e., overall units are watts/distance^3).

This shows how choice of wavelength band influences how much power you can get;

$$P_{\lambda 1-\lambda 2} = A_{object} \cdot \int_{\lambda 1}^{\lambda 2} \frac{2 \cdot \pi \cdot c^2 \cdot h}{\lambda^5} \cdot \frac{1}{\exp\left(\frac{h \cdot c}{\lambda \cdot k \cdot T}\right) - 1} d\lambda \qquad \text{Eq. 1.18}$$

For a 300K object of area $1cm^2$ you get:

$$P_{8\mu m\text{-}14\mu m} = 1.72 \times 10^{-2} watt \cdot cm^{-2} \qquad \text{Eq. 1.19}$$

$$P_{3\mu m\text{-}5\mu m} = 0.058 \times 10^{-2} watt \cdot cm^{-2} \qquad \text{Eq. 1.20}$$

Hence the decrease in MWIR performance is mainly due to the smaller integrated power from a 300K object over that band.

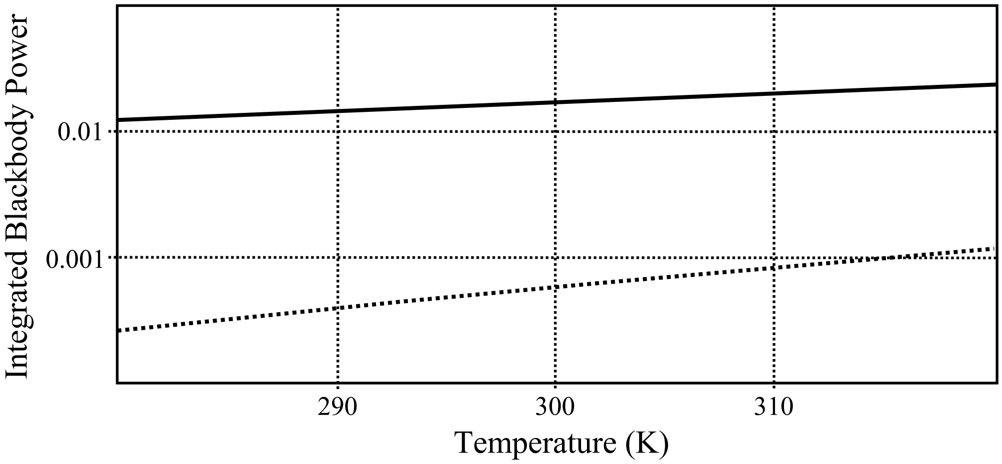

Figure 1.3: Plot of integrated blackbody power as a function of temperature; Solid: integrate Plank's law over LWIR, 8~14μm; Dotted: integrate MWIR, 3~5μm

From this we can now obtain the factor $(dP/dT)_{\lambda 1\text{-}\lambda 2}$ we need for the NETD calculation. If we had a system that integrated over all wavelengths, we would have

$$\left(dP/dT\right)_{0-\infty} = \sigma \cdot 4 \cdot T^3 \qquad \text{Eq. 1.21}$$

from $P_{total} = \sigma \cdot T^4 \cdot A_{object}$. Eq. 1.22

From a 300K object, this gives

$$\left(dP/dT\right)_{0-\infty} = 6.12\times10^{-4} W\cdot cm^{-2}\cdot K^{-1} \qquad \text{Eq. 1.23}$$

for all wavelength detection (The fact that this is exactly two orders of magnitude less than the total power is a coincidence of selecting 300K rather than some other temperature). If instead we integrate over only a finite range of wavelengths we will use Plank's Law for the spectral irradiance S from a blackbody, and then take the derivative of the integral. From a reference, they give for 8~14µm band:

$$(dP/dT)_{8\mu m\text{-}14\mu m}=2.62W\cdot m^{-2}\cdot K^{-1}=2.62\times10^{-4}W\cdot cm^{-2}\cdot K^{-1}, \qquad \text{Eq. 1.24}$$

That is about half of what you get if you integrated over all wavelengths. Using my own calculations this is also what I get at T=300K, or very close. dP/dT does increase with T: at 310K, I get about 2.85. Shifting to the MWIR band decreases by about a factor of ten:

$$(dP/dT)_{3\mu m\text{-}5\mu m}=2.1\times10^{-5}W\cdot cm^{-2}\cdot K^{-1} \qquad \text{Eq. 1.25}$$

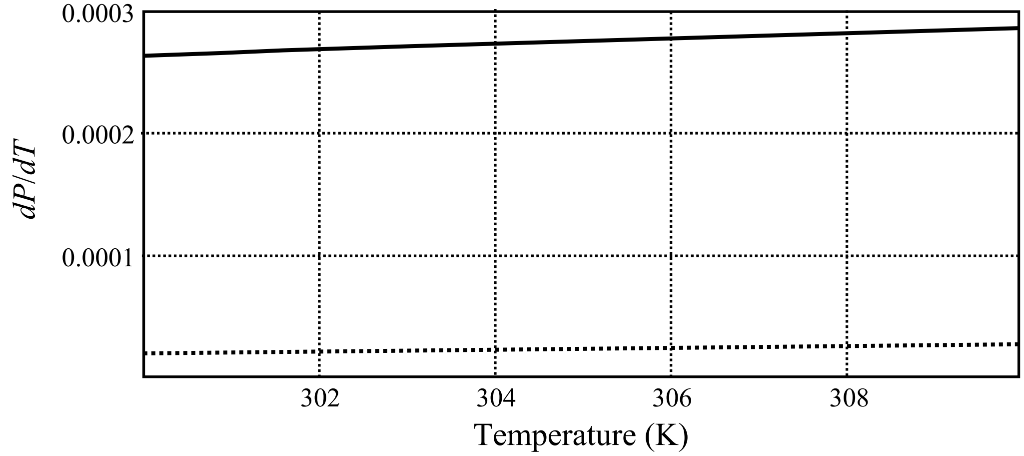

Figure 1.4: Plot of dP/dT as a function of temperature; Solid: integrate LWIR, 8~14µm; dotted: integrate MWIR, 3~5µm.

We can also look at dP/dT for the MWIR and LWIR bands as a function of object temperature. As temperature increases the blackbody power spectral density curve increases at all wavelengths, and the peak shifts to shorter wavelengths. The impact on dP/dT is shown below; the MWIR $(dP/dT)_{3\mu m\sim 5\mu m}$ at about 425K is equal to the LWIR $(dP/dT)_{3\mu m\sim 5\mu m}$ at 300K. By about 490K the MWIR $(dP/dT)_{3\mu m\sim 5\mu m}$ is greater than the LWIR $(dP/dT)_{8\mu m\sim 14\mu m}$ at the same temperature.

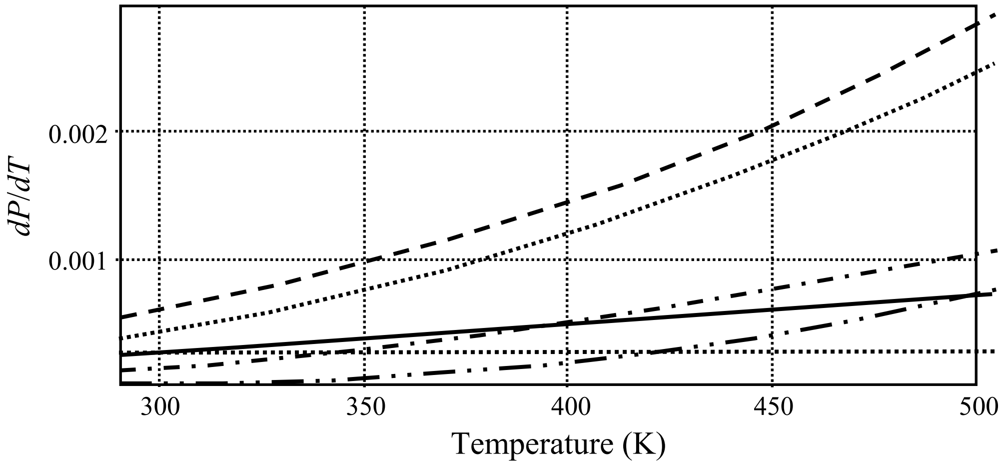

Figure 1.5: Plot of *dP*/*dT* as a function of temperature; Solid: integrate LWIR, 8~14μm; dotted: LWIR *dP*/*dT* for 300K; dash-dot-dot: integrate MWIR, 3~5μm; dash-dot: 5~8μm integration; dotted: 3~14μm integration; dashed: integrate over all wavelengths.

Now back to NETD calculations.

$$NETD = \frac{4F^2 \cdot NEP \cdot \sqrt{BW}}{\tau_{lens} \cdot A_{detector} \cdot (dP/dT)_{\lambda 1-\lambda 2}} = \frac{4F^2 \cdot \sqrt{BW}}{\tau_{lens} \cdot \sqrt{A_{detector}} \cdot D^* \cdot (dP/dT)_{\lambda 1-\lambda 2}} \qquad \text{Eq. 1.26}$$

Let's reference an f1 system, no loss in the optics, and 1Hz post detection bandwidth.

Then we will get:

$$NETD\left(\text{per } \sqrt{Hz}\right) = \frac{4}{(dP/dT)_{\lambda 1-\lambda 2}} \cdot \frac{NEP}{A_{detector}} = \frac{4}{(dP/dT)_{\lambda 1-\lambda 2}} \cdot \frac{1}{\sqrt{A_{detector}} \cdot D^*} \qquad \text{Eq. 1.27}$$

Assuming 300K and LWIR band this gives

$$(NETD)_{8\mu m\sim 14\mu m}\left(\text{per }\sqrt{Hz}\right)=\frac{4}{2.62\times10^{-4}}\cdot\frac{NEP\,(\text{in } W\ per\sqrt{Hz})}{A_{detector}\ (\text{in } cm^2)}$$
$$=1.5\times10^{-4}\cdot\frac{NEP\,(\text{in } W\ per\sqrt{Hz})}{A_{detector}\ (\text{in } cm^2)} \qquad \text{Eq. 1.28}$$

Working backwards, to get 50mK NETD using a 50×50μm^2 pixel would require an *NEP* of

$$\frac{50mK\cdot\left(50\times10^{-4}cm\right)^2}{1.5\times10^4}=NEP\,(\text{in } W \text{ per }\sqrt{Hz}) \qquad \text{Eq. 1.29}$$

or

$$NEP\approx 8\times10^{-11}\cdot\left(\frac{W}{\sqrt{Hz}}\right) \qquad \text{Eq. 1.30}$$

or

$$D^*=\frac{50\times10^{-4}cm}{8\times10^{-11}W/\sqrt{Hz}}=6\times10^7 \qquad \text{Eq. 1.31}$$

Example numbers: *NETD* for a good microbolometer is about 0.05K; pixel size is about 20×20μm.

$$\frac{50mK\cdot\left(20\times10^{-4}cm\right)^2}{1.5\times10^4}=NEP\,(\text{in } W \text{ per }\sqrt{Hz}) \qquad \text{Eq. 1.32}$$

or

$$NEP\approx 1.3\times10^{-11}\cdot\left(\frac{W}{\sqrt{Hz}}\right) \qquad \text{Eq. 1.33}$$

or

$$D^*=\frac{20\times10^{-4}cm}{1.3\times10^{-11}W/\sqrt{Hz}}=1.5\times108 \qquad \text{Eq. 1.34}$$

1.2.7 Bias Current

From the derived responsivity relationship, by increasing the bias current a higher responsivity can be achieved. The maximum bias current is likely to be limited by one of the following factors which lead to microbolometer failure: thermally induced current due to Joule heating, high filament current density which leads to electromigration failure in the detector element, and detector instability. Lewis described these microbolometer bias current limitations in more detail [13].

The power dissipated in the microbolometer detector consists of incoming radiation and Joule heating from the bias current. However, the power dissipated in the detector is predominantly due to Joule heating from the bias source. Therefore, the maximum allowable detector bias current can be restricted according to the maximum allowed temperature rise ΔT_{max}:

$$\Delta T_{\max} = T_{\max} - T_{amb} = P_{\max} \cdot Z_{thermal} = I_{\max}^2 \cdot R_{bolo} \cdot Z_{thermal} \qquad \text{Eq. 1.35}$$

where T_{max} is the maximum allowable temperature, T_{amb} is the ambient temperature, P_{max} is the maximum allowable *DC* bias power, and I_{max} is the maximum allowable bias current determined by the maximum allowed temperature rise. Hence the maximum allowable detector bias current is

$$I_{\max} = \sqrt{\frac{\Delta T_{\max}}{R_{bolo} \cdot Z_{thermal}}} \qquad \text{Eq. 1.36}$$

1.2.8 Power Absorption Efficiency

The quantity η ($P_{absorbed}/P_{incident}$) is the power absorption efficiency for the microbolometer detector. By maximizing the power absorption efficiency an absorption enhanced device can be fabricated. By modulating absorption of the incoming optical signal, the amount of absorbed power by the device can be adjusted, and the construction of a wavelength selective device is possible. There are two different approaches to control the power absorption efficiency. The first is to use a microbolometer material that responds to a specific wavelength [14]. The second is to alter the structure of the microbolometer to make the power absorption efficiency a function of wavelength [15].

1.3 THERMAL MODELS

The bolometer is a basic thermal radiation detector and can be divided into three parts: sensing element with thermal heat capacity $C_{thermal}$, heat sink, and thermal link connecting sensing element and heat sink with $R_{thermal}$. $C_{thermal}$ is the amount of heat required to increase the temperature of an isolated object. The bolometer converts incident electromagnetic radiation to heat and the converted heat is conducted via thermal resistance $R_{thermal}$. In the simplest case, the thermal time constant τ (also known as a characteristic thermal response time) is determined as a product of thermal resistance $R_{thermal}$ and thermal heat capacity $C_{thermal}$.

$$\tau = R_{thermal} \cdot C_{thermal} \qquad \text{Eq. 1.37}$$

At DC the temperate at the bolometer is determined as

$$T_{bolo} = T_{ambient} + \Delta T = T_{ambient} + P_{bolo} \cdot R_{thermal} \qquad \text{Eq. 1.38}$$

Therefore the temperature at the bolometer can be maximized by maximizing thermal resistance $R_{thermal}$ between the bolometer and heat sink. The structure described in Figure 1.6 is known as the Salisbury Screen. Originally the Salisbury Screen, consisting of a resistive sheet spaced a quarter wavelength from a conductive ground, was introduced as an electromagnetic absorber in World War II by W. W. Salisbury at the MIT Radiation Laboratory [16]. The Salisbury Screen has been adopted for the uncooled microbolometers by Honeywell [17].

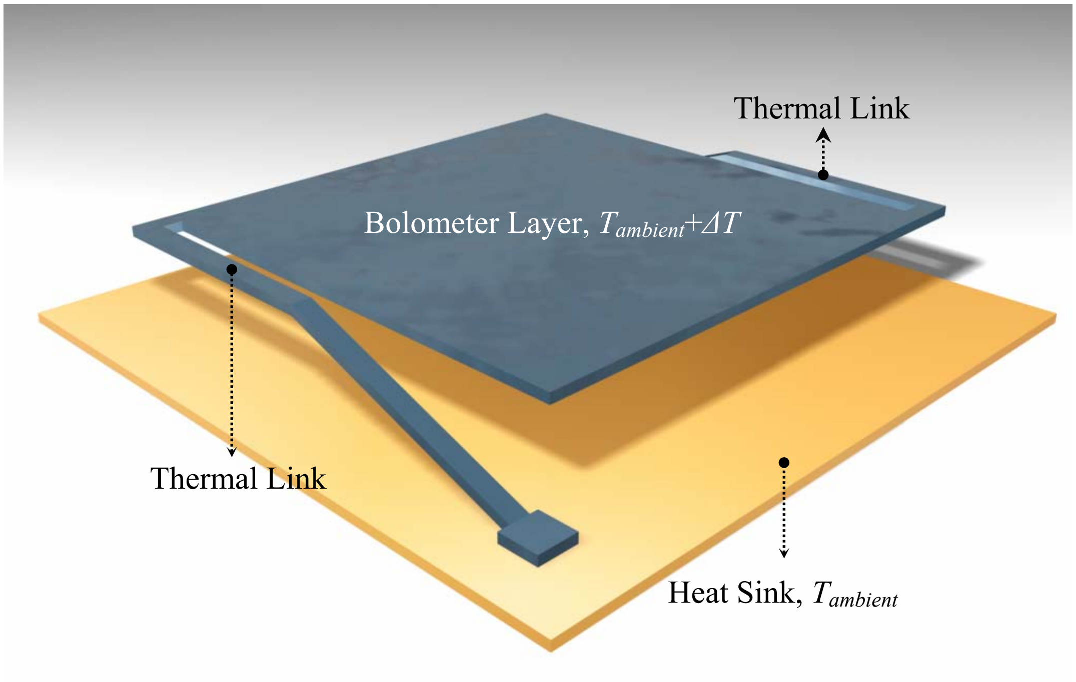

Figure 1.6: Microbolometer pixel structure consisting of sensing element, thermal links, and heat sink.

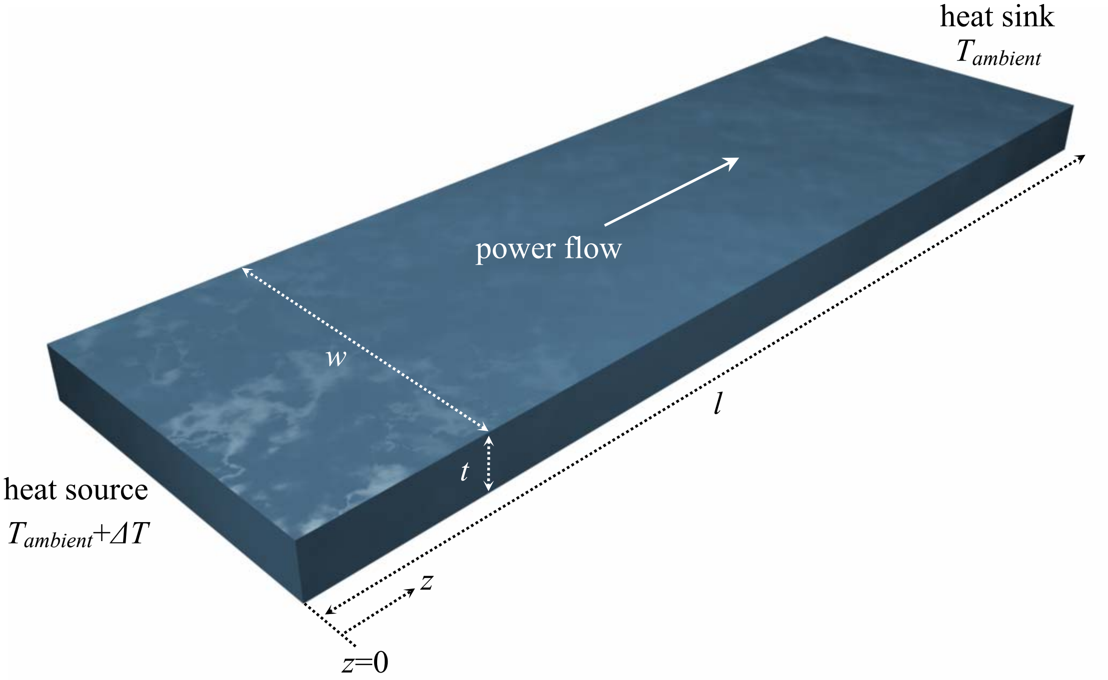

Figure 1.7: Simple thermal models of the thermal link.

A microbolometer's performance can be improved by increasing its thermal resistance. The air-bridge bolometer does this by suspending the device using thermal links like Figure 1.6. The only conduction path is now out the ends of the detector into heat sinks. We can model this thermal link in a particularly simple manner: a uniform bar of material (Figure 1.7). The thermal diffusion equation describing the temperature rise ϕ is

$$\nabla^2 \phi = \frac{\rho C}{\kappa} \cdot \frac{\partial \phi}{\partial t} \qquad \text{Eq. 1.39}$$

The 1-D thermal diffusion equation for the device shown in Figure 1.7 can be expressed as

$$\frac{\partial^2 \phi}{\partial z^2} = \frac{\rho C}{\kappa} \cdot \frac{\partial \phi}{\partial t} \qquad \text{Eq. 1.40}$$

where ρ, κ, and C are density, thermal conductivity, and specific heat of the bolometer material, respectively. Assuming that the power flowing from the source end of the bar is sinusoidally varying in time, the temperature rise ϕ can be defined as

$$\phi(z) = \phi_0 e^{j\omega t - \gamma z} \qquad \text{Eq. 1.41}$$

Applying this equation to the 1-D thermal diffusion equation, propagation constant γ can be solved as

$$\gamma = \sqrt{\frac{j\omega\rho C}{\kappa}}. \qquad \text{Eq. 1.42}$$

Now temperature rise $\phi_{z=0}$ can be expressed as

$$\phi_{z=0} = P \cdot Z_{thermal} = \frac{P}{tw}\sqrt{\frac{1}{j\omega\kappa\rho C}} \cdot \tanh\left(\sqrt{\frac{j\omega\rho C}{\kappa}} \cdot l\right) \qquad \text{Eq. 1.43}$$

At low frequency the thermal diffusion length is much longer than a bar,

$$\gamma l = \frac{1}{L_{thermal}} = \sqrt{\frac{j\omega\rho C}{\kappa}} \cdot l << 1 \qquad \text{Eq. 1.44}$$

and temperature rise $\phi_{z=0}$ can be approximated as

$$\phi_{z=0}^{low\ frequency} \approx \frac{P}{tw}\sqrt{\frac{1}{j\omega\kappa\rho C}} \cdot \sqrt{\frac{j\omega\rho C}{\kappa}} \cdot l = \frac{P}{tw} \cdot \frac{l}{\kappa} \qquad \text{Eq. 1.45}$$

which is just the thermal resistance of a bar with thermal conductivity κ. The actual input power looks like

$$P_{in} = P_{ave} \cdot [1 + \cos(\omega t)]. \qquad \text{Eq. 1.46}$$

so that the temperature rise at $z=0$ at low frequency is in phase with the input power (Figure 1.8). Consequently, temperature rises as the input power increases, and falls as the input power decreases.

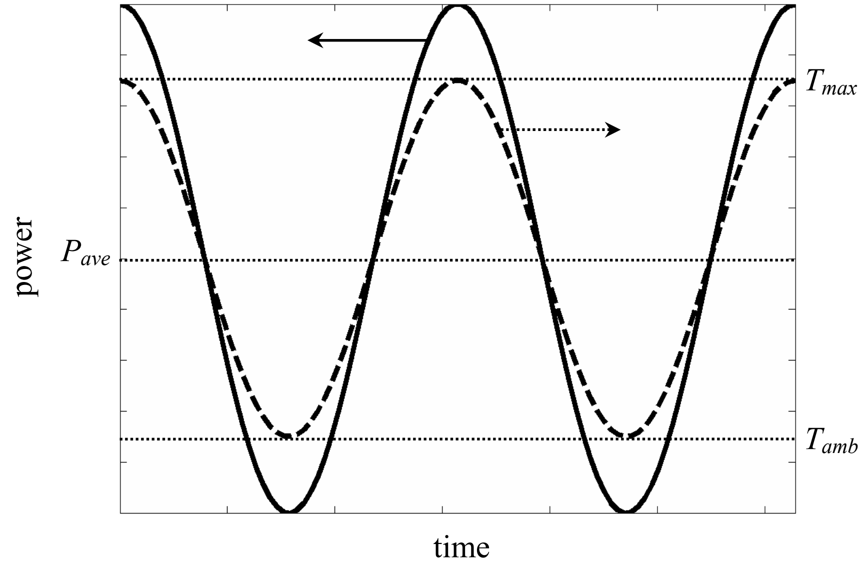

Figure 1.8: Temperature and power in phase at low frequency.

At high frequency the thermal diffusion length is much smaller than a bar,

$$\gamma l = \frac{1}{L_{thermal}} = \sqrt{\frac{j\omega\rho C}{\kappa}} \cdot l >> 1 \qquad \text{Eq. 1.47}$$

and temperature rise $\phi_{z=0}$ can be approximated as

$$\phi_{z=0}^{\text{high}\ frequency} \approx \frac{P}{tw}\sqrt{\frac{1}{j\omega\kappa\rho C}} = \frac{P}{tw} \cdot \frac{L_{thermal}}{\kappa} = \frac{P}{tw} \cdot \sqrt{\frac{1}{2\omega\kappa\rho C}} \cdot (1-j) \qquad \text{Eq. 1.48}$$

The temperature lags the power by 45°. As the frequency increases the magnitude of the temperature change decreases as $\sqrt{\omega}$ (Figure 1.9).

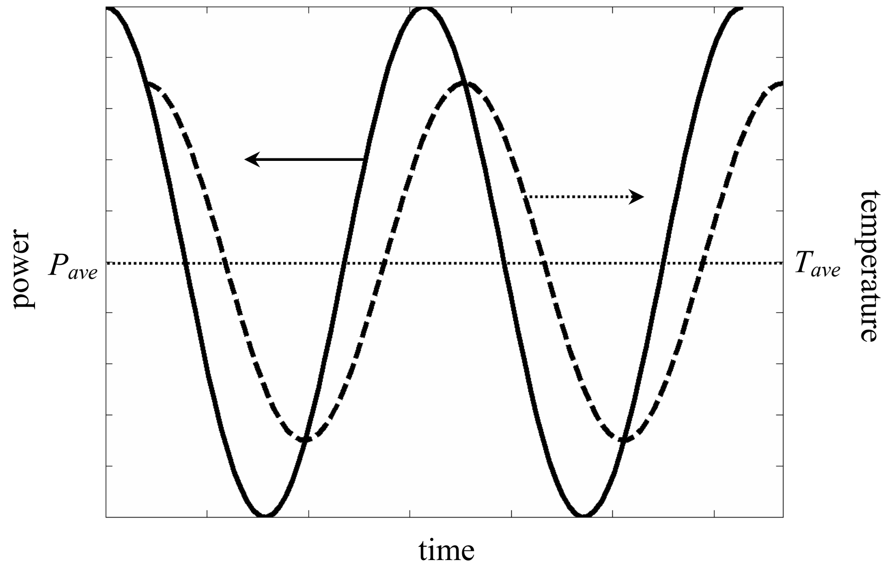

Figure 1.9: Temperature and power out of phase (45°) at high frequency.

1.4 MULTI-SPECTRAL MICROBOLOMETERS

According to Caulfield of Raytheon Vision Systems [18], one of the great features required for the next or 3rd generation IR sensors is the ability to sense multiple IR spectrums. Indeed, the infrared region provides a vast amount of information regarding the chemical composition of the absorbing media. Nearly all organic compounds and most inorganic compound exhibit species specific IR-based absorbances that are routinely exploited for their identification and quantification. Thus, the development of a multi-spectral capability with functionality in the infrared region would have a profound influence on a number of medical/environmental/processing applications.

Chapter 2: Planar Multimode Detector

2.1 MULTIMODE ARRAY

It is important to compare the detector size relative to an operating wavelength. A classical absorbing sheet (typical figure of merit: detectivity D^*) is much larger than the wavelength, and is its own "antenna". On the other hand, the micro-detector (typical figure of merit: *NEP*) is much smaller than the wavelength causing very poor coupling. For this reason, antenna structure has been combined with the micro-detector to enhance the electromagnetic coupling. Figure 2.1 is an air-bridge microbolometer combined with a bow-tie antenna published by D. P. Neikirk in 1984 [19].

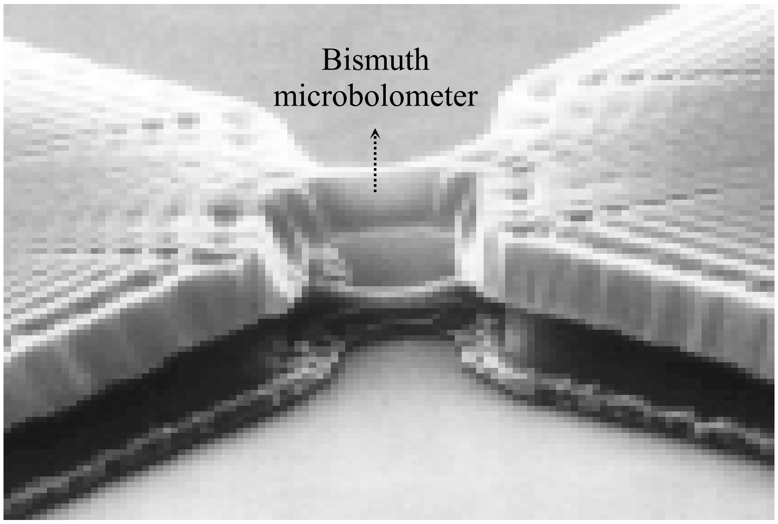

Figure 2.1: Air-bridge microbolometer combined with bow-tie antenna [19].

When the radiation source is a point source or its equivalent (Figure 2.2 (a)), the received power P is proportional to the power density of the source S and the effective antenna size A_e.

$$P=S\cdot A_e \qquad \text{Eq. 2.1}$$

In this case, the received power can be made as large as necessary by increasing the effective area of the single mode antenna A_e. According to Balanis [20], the effective area is defined as "the ratio of the available power at the terminals of a receiving antenna to the power flux density of a plane wave incident on the antenna from that direction, the wave being polarization matched to the antenna. If the direction is not specified, the direction of maximum radiation intensity is implied." In equation form it is written as

$$A_e = \frac{\text{power delivered to the load [W]}}{\text{power density of incident wave [W/m}^2\text{]}} \qquad \text{Eq. 2.2}$$

However, when the source is distributed (Figure 2.2 (b)), the received power can not be enhanced any more by simply increasing the effective area of the single mode antenna since the beamwidth narrows at the same time. This issue can be resolved by adding more antennas with a lens to focus the source on the array of antennas. In many cases, the elements of the array are identical because it is often convenient, simple, and practical even though it is not necessary [20]. Now the received power can be determined as

$$P=n \cdot k_B \cdot T \qquad \text{Eq. 2.3}$$

where n is the number of antennas, k_B is Boltzmann's constant, and T is the effective brightness temperature of the distributed source. According to Rutledge and Schwarz [21], this is the same as the power available from a terminated waveguide supporting n nodes so that they referred to the collection of antennas as an n-mode array. One of the advantages of multimode arrays is that the actual detection can be performed by small devices such as microbolometers while conventional absorbers need to be large to absorb enough power.

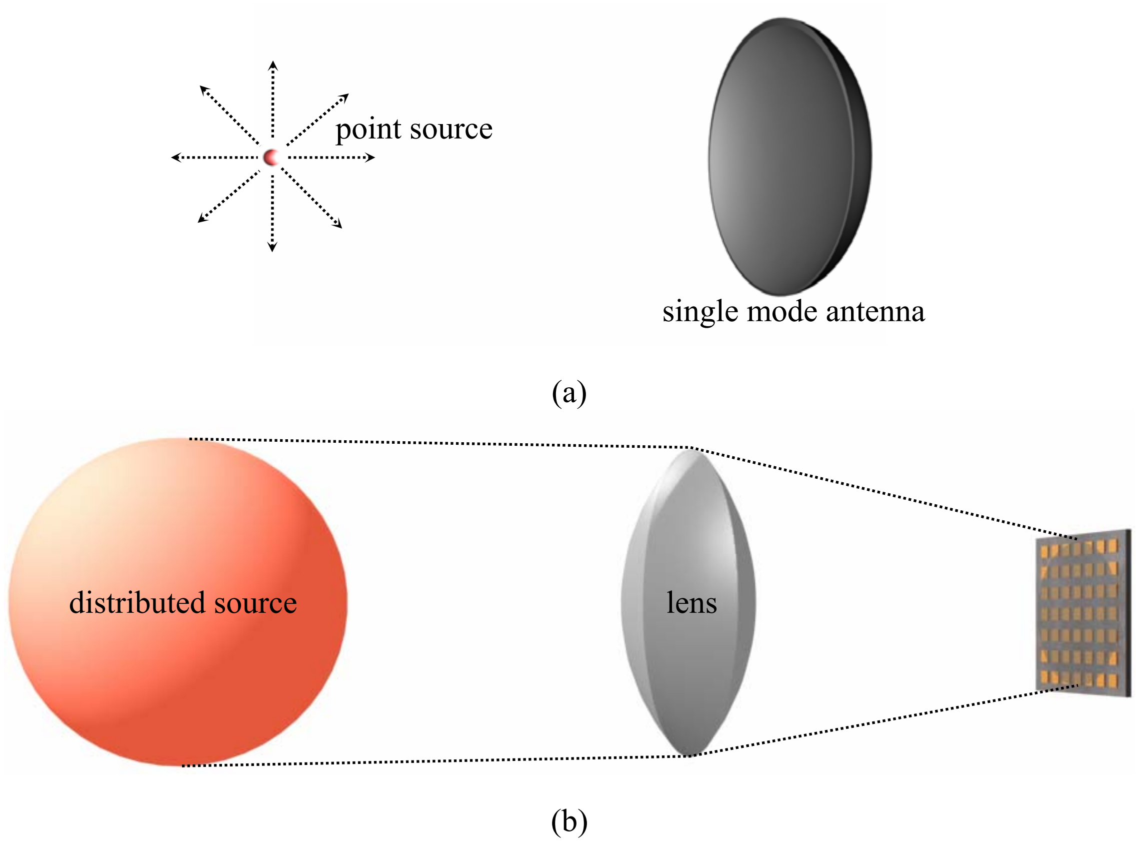

Figure 2.2: (a) Single mode antenna with a point source. $P = S \cdot A_e$. (b) A multimode antenna can be used to collect a large amount of power from distributed sources. $P = n \cdot k_B \cdot T$.

2.2 ELECTRICAL MODELS

The planar multimode antenna (Figure 2.3) has been extensively studied for infrared and millimeter wave detection by Rutledge and Schwarz [21]. In this structure, the power absorption efficiency is wavelength dependent, and is a function of the array period a, the capacitive gap width g, the inductive post width w, the distance to the mirror d, and the sheet resistance of the bolometer layer R_s (Figure 2.3 (a)). The mirror generates interference with above absorbing layers, and blocks interference with the behind readout integrated circuitry (ROIC) that could include sequential addressing of the pixels, some form of signal processing such as amplification, integration, multiplexing, and digitization.

According to Rutledge and Schwarz, there is an upper limit on the spacing that can exist between rows or columns of the periodic structure imposed by the possibility that the structure may act as a grating. To avoid this, we restrict our designs so that the array period *a* is less than the shortest wavelength considered in a given design.

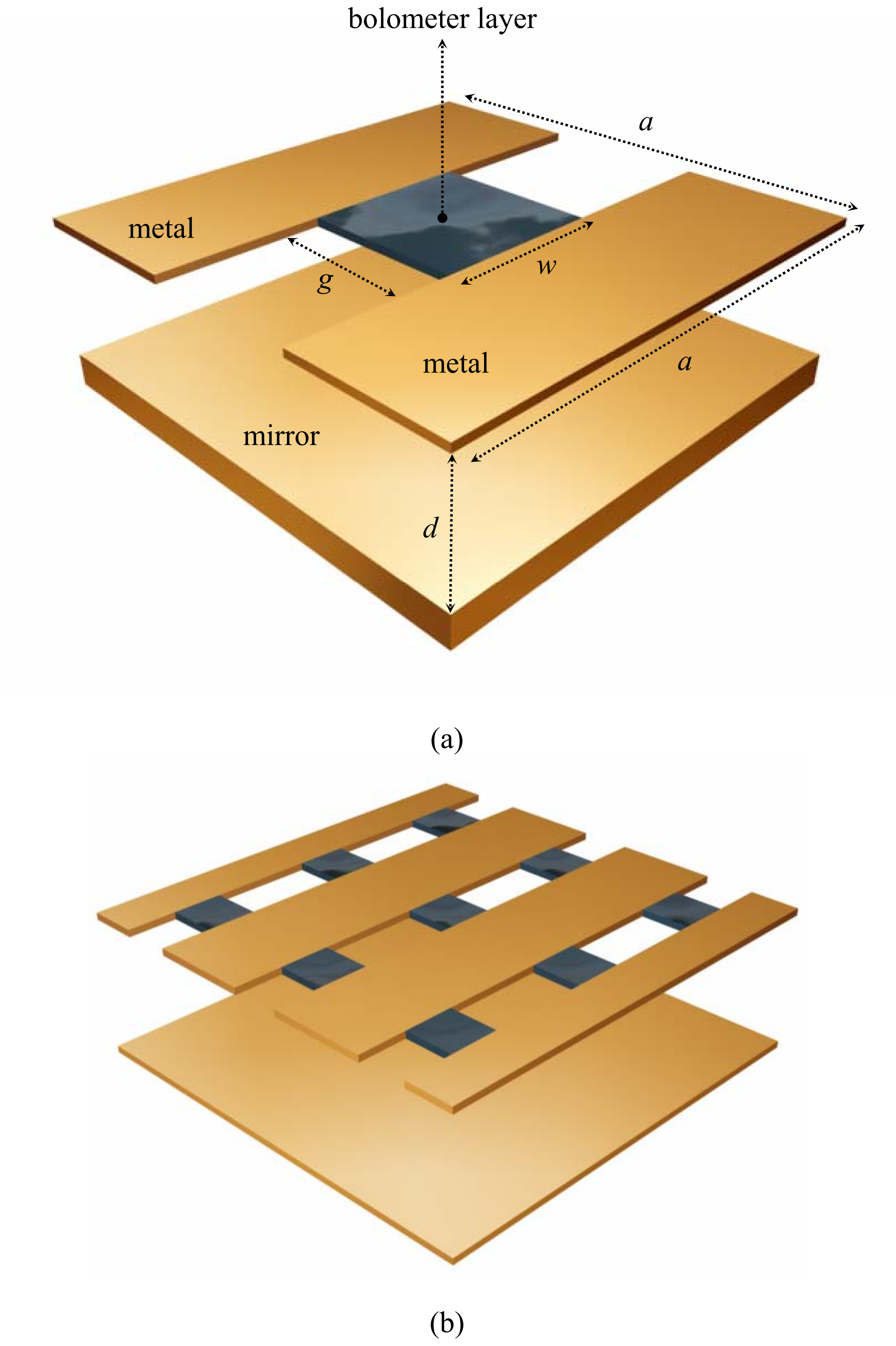

(a)

(b)

Figure 2.3: (a) Configuration of a unit cell of the planar multimode detector, consisting of a grid of wide metal sheets connected by narrow resistive bolometer layers. (b) Array of cells.

The electromagnetic behavior of this array can be analyzed using a modification of waveguide post-mount analysis [21-22] and ABCD matrix analysis [23]. The air gap between metal "bars" (gap distance: *g*) is represented by a normalized capacitive susceptance B_c. Parallel to this is a normalized inductive susceptance of the "post" B_l in series with the detector conductance G_d. The parasitic capacitance parallel to the detector is neglected. Behind the air gap (gap distance: *d*) is a mirror that acts as a shorting plane. This short, together with the section of transmission line in front of it, acts as an adjustable susceptance. We wish to choose the gap and the lead width so that the detector acts as a susceptance *B* in parallel with a conductance *G* that is nearly equal to unity. The transmission line model of the planar multimode detector is shown in Figure 2.4.

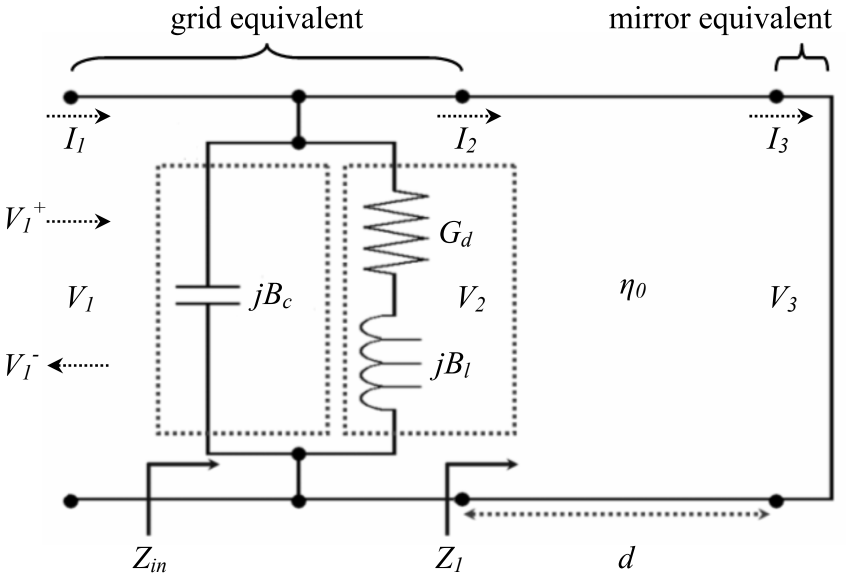

Figure 2.4: Equivalent transmission line models of the planar multimode detector shown in Figure 2.3.

Eisenhart and Khan calculated and verified the value of the circuit parameters in Figure 2.4 in two ways [22]. The first is a quasi-static method that is simple, but only accurate enough for preliminary calculation. The second is a modification of the EMF method that is accurate, but not simple. In both analyses they reduce the array to a single waveguide bounded on the top and bottom by electric walls and on the sides by magnetic walls. Their quasi-static analysis was as follows. The capacitance of the gap is assumed to be unaffected by the presence of the post, by shorting plane, or by the fact that the air gap has only a finite thickness. It is then calculated by conformal mapping. The result is

$$B_c = \frac{2k_0 a}{\pi}\left(\frac{1+\varepsilon_r}{2}\right)\ln\csc\left(\frac{\pi g}{2a}\right) \qquad \text{Eq. 2.4}$$

where k_0 is the propagation constant of free space. Applying Babinet's principle and duality to the capacitive slot, the inductance can be obtained as

$$B_l = -\left(\frac{k_0 g}{2\pi}\ln\csc\frac{\pi w}{2a}\right)^{-1} \qquad \text{Eq. 2.5}$$

For the modification of the EMF method, they analyzed a gap-post configuration in a metal waveguide. Their features of the calculation are as follows. First of all, the waveguide has magnetic side walls rather than metal side walls, which results in the changes of the modes in the metal waveguide. Secondly it is a slot configuration rather than a post configuration, which requires Babinet's principle and duality. Finally, the problem is complicated by the presence of the dielectric substrate. It is assumed that, in the slot, only the y-component for the electric field exists. They, therefore, excite only modes that are *TE* to the x axis and, by symmetry, only those that have even symmetry about the x and y axes. The y-component of the electric field of the mode with indexes m, n of the form

$$E_y \propto \cos\frac{2m\pi x}{a}\cos\frac{2n\pi y}{a} \qquad \text{Eq. 2.6}$$

Note that, unlike the case of a hollow metal waveguide, solutions exist for all nonnegative integers m and n. The H_x component is given by

$$H_x = -Y_{mn}E_y \qquad \text{Eq. 2.7}$$

where Y_{mn} is the admittance of the *m*, *n*th mode given by Harrington:

$$Y_{mn} = \frac{k^2 - (2m\pi/a)^2}{\omega\mu\sqrt{k^2 - (2m\pi/a)^2 - (2n\pi/a)^2}} \qquad \text{Eq. 2.8}$$

Here *k* is the propagation constant of plane waves in the material. We find that the susceptance of the gap is given by

$$jB_c \cdot Z_0 = -2Y_0^{-1}\left(1 - \frac{g}{a}\right)\sum_{n=1}^{\infty}\left(\frac{\sin n\pi g/a}{n\pi g/a}\right)^2 \left(Y_{on}^{+} + Y_{on}^{-}\right) \qquad \text{Eq. 2.9}$$

where the Y_{on}^{+} are the admittances looking in the +*z* direction, the Y_{on}^{-} are the admittances looking in the –*z* direction, and $Y_0 = \sqrt{\varepsilon_0/\mu_0}$ is the characteristic admittance of free space.

$$Y_{on}^{+} = \frac{k_{+}^2}{\omega\mu\sqrt{k_{+}^2 - \left(\frac{2n\pi}{a}\right)^2}} = -j\frac{a}{\lambda}\sqrt{\frac{\varepsilon_0}{\mu_0}}\frac{1}{\sqrt{n^2 - (a/\lambda)^2}} \qquad \text{Eq. 2.10}$$

$$\text{where } k_{+} = 2\pi/\lambda . \qquad \text{Eq. 2.11}$$

$$Y_{on}^{-} = -j\frac{a}{\lambda/\sqrt{\varepsilon_r}}\sqrt{\frac{\varepsilon_0\varepsilon_r}{\mu_0}}\frac{1}{\sqrt{n^2 - \left(\frac{a}{\lambda/\sqrt{\varepsilon_r}}\right)^2}} = -j\frac{a}{\lambda}\sqrt{\frac{\varepsilon_0}{\mu_0}}\frac{\varepsilon_r}{\sqrt{n^2 - \left(\frac{a}{\lambda/\sqrt{\varepsilon_r}}\right)^2}} \qquad \text{Eq. 2.12}$$

Therefore the normalized capacitive susceptance is

$$jB_c = j\sqrt{\frac{\varepsilon_0}{\mu_0}} \cdot 2 \cdot \left(1 - \frac{g}{a}\right) \cdot \frac{a}{\lambda} \cdot \sum_{n=1}^{\infty}\left(\frac{\sin n\pi g/a}{n\pi g/a}\right)^2 \cdot \left[\frac{1}{\sqrt{n^2 - \left(\frac{a}{\lambda}\right)^2}} + \frac{\varepsilon_r}{\sqrt{n^2 - \left(\frac{a}{\lambda/\sqrt{\varepsilon_r}}\right)^2}}\right]$$

Eq. 2.13

The factor (1-*g*/*a*) is a phenomenological quantity that Eisenhart and Khan found necessary to insert in order for their theory to agree with experimental results [22]. The lead susceptance is given by

$$\left(jB_l \cdot Z_0\right)^{-1} = -2Y_0 \sum_{m=1}^{\infty} \left[\frac{\left(\frac{\sin \frac{m\pi w}{a}}{\frac{m\pi w}{a}} \right)^2}{\sum_{n=0}^{\infty} \varepsilon_n \left(\frac{\sin \frac{n\pi g}{a}}{\frac{n\pi g}{a}} \right)^2 \left(Y_{mn}^{+} + Y_{mn}^{-}\right)} \right] \qquad \text{Eq. 2.14}$$

where ε_n is the Neumann factor

$$\varepsilon_n = \begin{cases} \varepsilon_n = 1 & \text{if } n = 0 \\ \varepsilon_n = 2 & \text{otherwise} \end{cases}$$

$$Y_{mn}^{+} = \frac{\left(\frac{2\pi}{\lambda}\right)^2 - \left(\frac{2m\pi}{a}\right)^2}{2\pi \frac{c}{\lambda} \mu \sqrt{\left(\frac{2\pi}{\lambda}\right)^2 - \left(\frac{2m\pi}{a}\right)^2 - \left(\frac{2n\pi}{a}\right)^2}} = \frac{\lambda}{a} \sqrt{\frac{\varepsilon_0}{\mu_0}} \frac{\left(\frac{a}{\lambda}\right)^2 - m^2}{\sqrt{\left(\frac{a}{\lambda}\right)^2 - m^2 - n^2}} \qquad \text{Eq. 2.15}$$

$$Y_{mn}^{-} = \frac{\lambda / \sqrt{\varepsilon_r}}{a} \sqrt{\frac{\varepsilon_0 \varepsilon_r}{\mu_0}} \frac{\left(\frac{a}{\lambda / \sqrt{\varepsilon_r}}\right)^2 - m^2}{\sqrt{\left(\frac{a}{\lambda / \sqrt{\varepsilon_r}}\right)^2 - m^2 - n^2}} \qquad \text{Eq. 2.16}$$

Therefore the normalized inductive susceptance is

$$\left(jB_l\right)^{-1} = -\frac{2a}{\lambda} \cdot \sqrt{\frac{\varepsilon_0}{\mu_0}} \cdot \sum_{m=1}^{\infty} \frac{\left(\frac{\sin \frac{m\pi w}{a}}{\frac{m\pi w}{a}} \right)^2}{\sum_{n=0}^{\infty} \varepsilon_n \left(\frac{\sin \frac{n\pi g}{a}}{\frac{n\pi g}{a}} \right)^2 \cdot \left(\frac{\left(\frac{a}{\lambda}\right)^2 - m^2}{\sqrt{\left(\frac{a}{\lambda}\right)^2 - m^2 - n^2}} + \frac{\left(\frac{a}{\lambda / \sqrt{\varepsilon_r}}\right)^2 - m^2}{\sqrt{\left(\frac{a}{\lambda / \sqrt{\varepsilon_r}}\right)^2 - m^2 - n^2}} \right)}$$

Eq. 2.17

The admittance of the grid (planar multimode detector without a mirror) is

$$Y_{grid} = jB_c + (jB_l) // G_d = jB_c + \frac{jB_l \cdot G_d}{jB_l + G_d} \qquad \text{Eq. 2.18}$$

$$\text{where the conductance } G_d = \left(R_s \cdot \frac{g}{w} \right)^{-1}. \qquad \text{Eq. 2.19}$$

Using ABCD matrices, voltage, current, and power at each boundary can be determined. The ABCD matrix analysis is very useful especially at the cascade connection of the two-port networks since whole networks can be characterized by the simple product of ABCD matrices representing the individual two-ports. The ABCD matrix of the grid part can be expressed as

$$ABCD_{grid} = \begin{pmatrix} 1 & 0 \\ Y_{grid} & 1 \end{pmatrix} \qquad \text{Eq. 2.20}$$

where Y_{grid} is the admittance of the grid. The air gap between the grid and the mirror can also be characterized using ABCD matrix as

$$ABCD_{air} = \begin{pmatrix} \cos\beta d & j\eta_0 \sin\beta d \\ \frac{j}{\eta_0}\sin\beta d & \cos\beta d \end{pmatrix}. \qquad \text{Eq. 2.21}$$

So the voltage and current at the boundaries are

$$\begin{pmatrix} V_2 \\ I_2 \end{pmatrix} = ABCD_{air} \begin{pmatrix} V_1 \\ I_1 \end{pmatrix} \qquad \text{Eq. 2.22}$$

$$\begin{pmatrix} V_1 \\ I_1 \end{pmatrix} = ABCD_{grid} \begin{pmatrix} V_2 \\ I_2 \end{pmatrix} \qquad \text{Eq. 2.23}$$

V_3 is set to zero since the mirror acts as a shorting plane.

Incoming V_1^+ and outgoing V_1^- voltages at the topmost boundary are determined as

$$V_1^+ = \frac{1}{2}(V_1 + Z \cdot I_1) \qquad \text{Eq. 2.24}$$

$$V_1^- = \frac{1}{2}(V_1 - Z \cdot I_1) \qquad \text{Eq. 2.25}$$

so the power absorbed by the bolometer layer is

$$P_1 - P_2 = \frac{1}{2}\mathrm{Re}\left(V_1 I_1^*\right) - \frac{1}{2}\mathrm{Re}\left(V_2 I_2^*\right) \qquad \text{Eq. 2.26}$$

Consequently the power absorption efficiency η is

$$\eta\left(a, g, w, d, R_s, \lambda\right) = \frac{P_{absorbed}}{P_{incident}} = \frac{P_1 - P_2}{\frac{1}{2}\left(\frac{\left|V_1^+\right|^2}{Z}\right)} = \frac{\mathrm{Re}\left(V_1 I_1^*\right) - \mathrm{Re}\left(V_2 I_2^*\right)}{\frac{\left|V_1^+\right|^2}{Z}} \qquad \text{Eq. 2.27}$$

Figure 2.5 shows a conceptual illustration of a single pixel consisting of the array of the planar multimode detectors. A pixel is the smallest single individual image element of detection on the thermal imaging sensor. For example, in the case of the imaging sensor having 320×240 resolution, it consists of 320×240 pixels. In Figure 2.5, metal layers act as antennas as well as heat sinks and help to focus IR radiation into a narrow resistive sheet like a lens. The absorbed IR power changes the resistance of the resistive sheets, and then output voltage is changed under the fixed bias current I_b. However, thin layers can not be physically self-supportive so they require supportive layers. Figure 2.6 shows the configuration of a pixel with supportive layers and legs on the substrate. Figure 2.7 illustrates the whole focal plane arrays (FPA) using the planar multimode detectors. The focal plane array is a group of pixels organized into a rectangular grid. The size of the focal plane array is measured by multiplying the horizontal number of pixels by the vertical number of pixels.

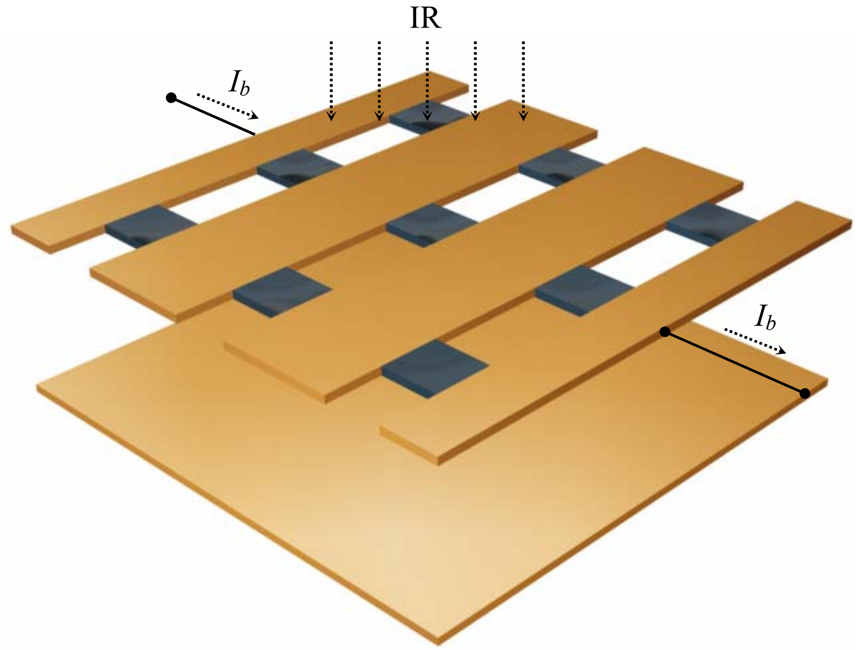

Figure 2.5: Configuration of a pixel of the planar multimode detector.

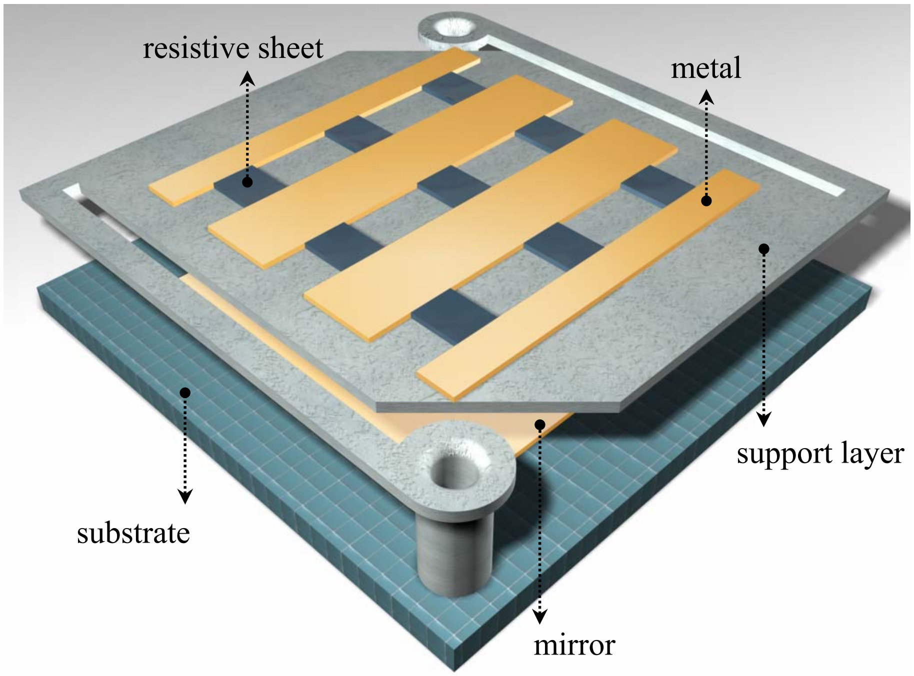

Figure 2.6: Configuration of a pixel with supportive layers and legs on the substrate.

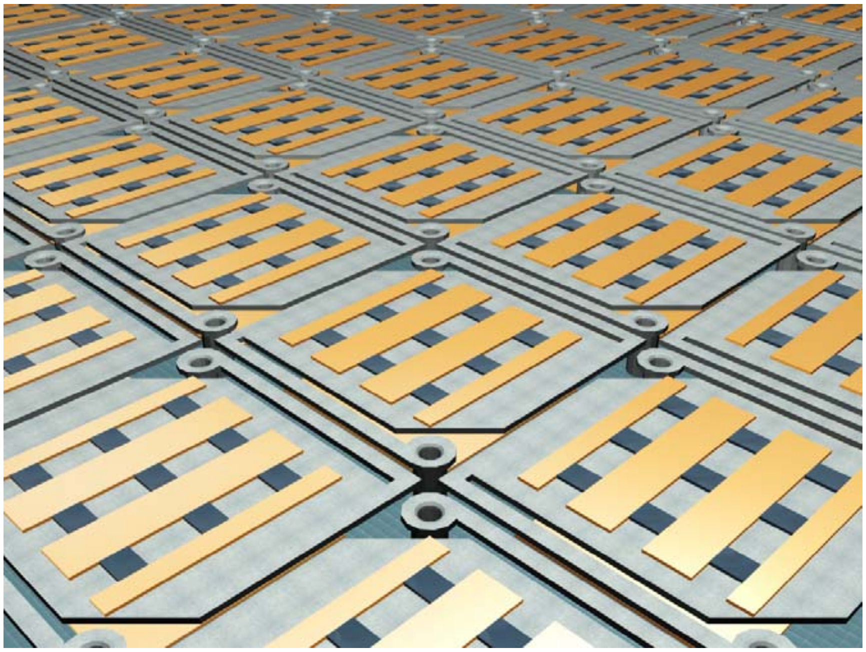

Figure 2.7: Focal plane array (FPA) using the planar multimode detectors.

There are many combinations of array dimensions, a, g, w, and d, and microbolometer material sheet resistance R_s that can produce a detector with high absorption at a designated wavelength. Figure 2.8 shows calculated array responses using the modified post-mount model combined with an ABCD matrix analysis. The behavior of the array approaches that of a simple Salisbury Screen when g and w approach a, and R_s approaches 377Ω; in this case the array bandwidth is as wide as the Salisbury Screen.. Other designs can produce much narrower bandwidths, narrow enough to construct multiple channels within the 7-14μm infrared band. The diversity of the solutions is an advantage of this multimode detector, allowing a search for desired characteristics. The genetic algorithm (GA) was adopted as an optimization scheme. The GA will be introduced in section 3.2. In Figure 2.8, the design goal is to maintain strong absorption at a specified wavelength (10μm) within the 7-14μm IR band with diverse bandwidth.

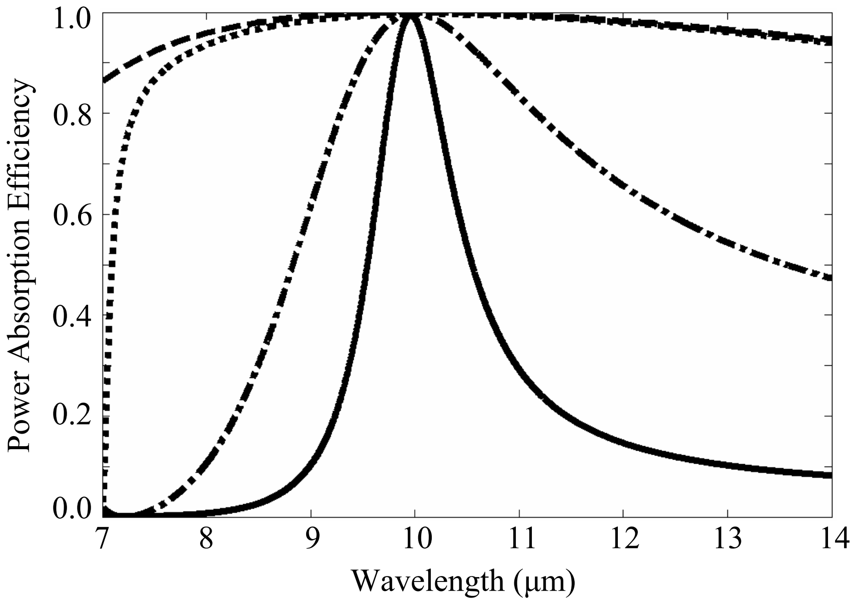

Figure 2.8: Design of multimode detectors with unity absorption at center wavelength 10μm, but widely varying bandwidths. Bandwidth can be wide as the Salisbury Screen (dashed line), and narrow enough to construct multiple channels within the 7~14μm IR band (solid line). All specific design geometries are given in Table 2.1.

	Salisbury Screen	Planar Multimode Detector		
	Dashed	Dotted	Dash-Dot	Solid
a	N/A	7.00μm	5.33μm	6.90μm
g	N/A	5.00μm	1.00μm	0.20μm
w	N/A	4.50μm	0.96μm	3.00μm
d	2.50μm	2.50μm	3.61μm	3.29μm
R_s	377Ω	377Ω	30Ω	53.49Ω

Table 2.1: Specific designs yielding response curves given in Figure 2.8.

Here the bolometer layers are assumed as infinitely thin conductive sheets. The bolometer layer material can be characterized at the angular frequency ω using their permittivity ε, and conductivity σ, recalling that the complex ε is

$$\varepsilon = \varepsilon' - j\varepsilon'' = \varepsilon' - j\frac{\sigma}{\omega}. \qquad \text{Eq. 2.28}$$

Depending on their relaxation frequency $\sigma/\omega\varepsilon$, the material falls into two categories: conductors and dielectrics. Possible materials to absorb the incoming radiation would be 'thin conductors' and 'lossy dielectrics'. To evaluate which material is better for the bolometer layers, we set up the Salisbury Screen as shown in Figure 2.9 and GA-optimize it for the broad band absorption in 3 to 13µm band.

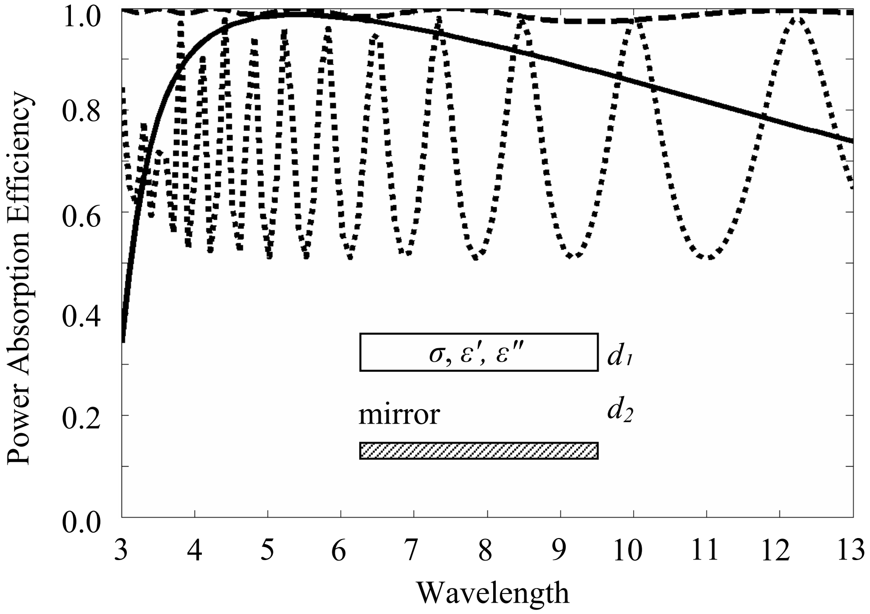

Figure 2.9: Broad band absorptions by 'thin conductors' (solid curve, design 1 in Table 2.2) and 'lossy dielectrics' (dashed and dotted curves). The dashed curve (design 9 in Table 2.2) is the broadest but simulated with unrealistic dielectric constant. From the comparison between the solid (thin conductors) and dotted (lossy dielectrics, design 15 in Table 2.2) curves, 'thin conductors' are better than 'lossy dielectrics' as bolometer layers for broad band absorption.

For simplicity, we assume $\varepsilon''=0$ (if $\sigma\neq0$ then $\varepsilon''\neq0$). In this optimization process, conductivity of the bolometer layer σ and air gap thickness d_2 are free parameters corresponding to fixed thickness (d_1) and ε' of bolometer layer. The optimized results are listed in Table 2.2. For ε', we use 1, 4, and 7.5 for fictitious materials. First of all, we evaluate designs with $\varepsilon'=1$ (designs 1 to 9 in Table 2.2) chosen for simplicity. Their bolometer layer thickness d_1s are sampled from 1nm to 10μm. From the results, we can say that the optimized bolometer layers of designs 1 to 4 are good conductors because their $\sigma/\omega\varepsilon$ are much greater than 1. Also their thicknesses are much less than their skin depth δ. Therefore, designs 1 to 4 are 'thin conductors'. On the other hand, the optimized bolometer layers of designs 7 to 9 are 'lossy dielectrics' because their $\sigma/\omega\varepsilon$ are less than 1. Also note that their thicknesses are bigger than or comparable to their absorption length δ. In Table 2.2, the figure of merit is 'integrated efficiency', which varied from 0% (no power absorption in a given band) to 100% (perfect power absorption in a given band) and expressed as

$$\text{integrated efficiency}=\frac{\int_{3\mu m}^{13\mu m}\text{PAE}(\lambda)\;d\lambda}{\int_{3\mu m}^{13\mu m}1\quad d\lambda}\times100\,(\%) \qquad \text{Eq. 2.29}$$

where PAE stands for power absorption efficiency. The figure of merit, integrated efficiency, reveals that power absorptions by 'lossy dielectrics' broaden rapidly as d_1 gets thick, while those by 'good conductors' are pretty similar as d_1 thickens. This means that 'lossy dielectrics' are better than 'thin conductors' as bolometer layers for the broad band absorption. Recall that ε' for the bolometer layer is fictitious 1. For 'thin conductor', ε' does not affect its characteristic impedance much because σ is much greater than $j\omega\varepsilon$. Thus, the results of thin conductor (design 1 to 4 in Table 2.2) are realistic. However, ε' affects much characteristic impedance of 'lossy dielectric', and 'lossy dielectrics' with $\varepsilon'=1$ do not exist. To be more realistic with 'lossy dielectric', we replace ε' of 'lossy dielectric' from 1 to 4 (designs 10 to 12 in Table 2.2) or 7.5 (designs 13 to 15 in Table 2.2). The figures of merit, integrated efficiencies, show that power absorptions by 'lossy dielectrics' get worse as ε' increases. Integrated efficiencies of 'lossy dielectrics' corresponding to ε'=1, 4, and 7.5 are 99.9% (design 9), 85.5% (design 12), and 72.3% (design 15), respectively. Therefore, the integrated efficiency of a more realistic 'lossy dielectric' is 85.5% or 72.3% rather than 99.9%. Regardless of ε', the integrated efficiencies of 'thin conductors' are ~88% (designs 1 to 4). Consequently, we can say that 'thin conductors' are better than 'lossy dielectric' as bolometer layers. Figure 2.9 is the power absorption efficiencies of 'thin conductor'(solid line, design 1 in Table 2.2) and 'lossy dielectrics'(dashed and dotted line). The dashed line in Figure 2.9 results from 'lossy dielectric' with an unrealistic ε' (design 9 in Table 2.2), while the dotted one results from 'lossy dielectric' with a more realistic ε' (design 15 in Table 2.2). Therefore, it would be more reasonable to compare the solid line (thin conductor) and the dotted line (lossy dielectric) rather than the solid line (thin conductor) and the dashed line (lossy dielectric). Figure 2.9 clearly illustrates that 'thin conductors' are better than 'lossy dielectrics' as bolometer layers for broad band absorption. In addition 'thin conductor' would be better because thick bolometer layers result in high thermal capacitance and lower speed. Based on this observation, in subsequent designs the bolometer/absorbing layers are assumed to be thin finite conductivity layers.

Design	ε_r	d_1(μm)	σ(S/m)	d_2(μm)	Integrated Efficiency (%)	$\sigma/\omega\varepsilon$		$\delta=1/\alpha$ (μm)		$\lambda_{dielectric}$ (μm)		
						λ=3μm	λ=13μm	λ=3μm	λ=13μm	λ=3μm	λ=13μm	
1	1	0.001	3.3×10^6	1.35	88.3	598	2,590	0.028	0.058	0.17	0.36	$d_1 \ll \delta$
2		0.003	1.1×10^6	1.35	88.4	200	866	0.048	0.099	0.30	0.62	$d_1 \ll \delta$
3		0.01	3.3×10^5	1.35	88.4	60	259	0.080	0.18	0.54	0.11	$d_1 \ll \delta$
4		0.03	1.1×10^5	1.33	88.4	20	86	0.16	0.31	0.93	2.0	$d_1 \ll \delta$
5		0.1	3.3×10^4	1.30	88.5	6	26	0.30	0.59	1.6	3.5	$d_1<\delta$
6		0.3	1.1×10^4	1.20	89.0	2	9	0.60	1.0	2.4	5.9	$d_1<\delta$
7		1	3.7×10^3	1.00	92.7	0.7	2.9	1.5	2.0	2.9	9.1	$d_1\approx\delta$
8		3	1.7×10^3	0.11	98.2	0.3	1.3	3.1	3.6	3.0	11	$d_1\approx\delta$
9		10	7.6×10^2	0.06	99.9	0.1	0.6	7.0	7.3	3.0	13	$d_1>\delta$
10	4	1	3.7×10^3	1.00	74.4	0.7	2.9	2.9	3.0	1.5	6.2	$d_1\approx\delta$
11		3	1.7×10^3	0.11	75.1	0.3	1.3	6.2	6.3	1.5	6.4	$d_1\approx\delta$
12		10	7.6×10^2	0.06	85.5	0.1	0.6	14.0	14.0	1.5	6.5	$d_1\approx\delta$
13	7.5	1	3.7×10^3	1.00	49.6	0.7	2.9	3.9	4.0	1.1	4.7	$d_1\approx\delta$
14		3	1.7×10^3	0.11	68.5	0.3	1.3	8.5	8.5	1.1	4.7	$d_1\approx\delta$
15		10	7.6×10^2	0.06	72.3	0.1	0.6	19.1	19.2	1.1	4.7	$d_1\approx\delta$

Table 2.2: GA-optimized designs of Salisbury Screen (Figure 2.9) for broad band absorption in 3~13μm band. These results reveal that ‘thin conductors’ are better than ‘lossy dielectrics’ as bolometric material from the perspective of broad band absorption. Refer to Figure 2.9 for their spectral responses.

The preceding discussion shows that the best possible situation is one in which the absorption length in the bolometer material is very small, and the thickness of the layer is less than its absorption length. For a conducting layer this corresponds to the case where the layer thickness is much less than the skin depth. Hence, the sheet resistance of the conductive layer can be approximated by $(\sigma l)^{-1}$, where l is the thickness and σ the conductivity of the conductive layer. For example, let's assume the Salisbury Screen consists of an absorbing bolometer layer and a mirror. When a plane wave strikes a bolometer layer much less than an absorption length at normal incidence, the equivalent transmission model can be expressed as Figure 2. 10.

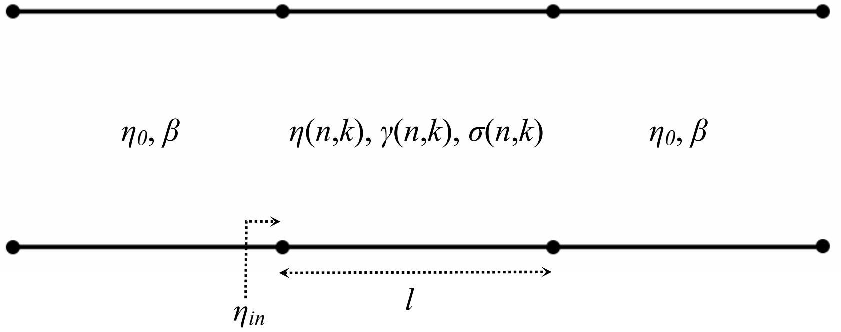

Figure 2.10: Transmission model when a plane wave strikes a finite thick layer in between free space.

In this model, input characteristic impedance is determined as

$$\eta_{in} = \eta \frac{\eta_0 + \eta \tanh(\gamma l)}{\eta + \eta_0 \tanh(\gamma l)}$$

$$= \frac{1}{\sigma\delta}(1+j) \cdot \frac{\sqrt{\frac{\mu_0}{\varepsilon_0}} + \frac{1}{\sigma\delta}(1+j)\tanh\left\{\frac{1}{\delta}(1+j)\cdot l\right\}}{\frac{1}{\sigma\delta}(1+j) + \sqrt{\frac{\mu_0}{\varepsilon_0}}\tanh\left\{\frac{1}{\delta}(1+j)\cdot l\right\}} \qquad \text{Eq. 2.30}$$

When $l << \delta$

$$\tanh\left\{\frac{l}{\delta}(1+j)\right\} \approx \frac{l}{\delta}(1+j) \qquad \text{Eq. 2.31}$$

Above input characteristic impedance is now expressed as

$$\eta_{in} = \frac{1}{\sigma l} \cdot \frac{\sqrt{\frac{\mu_0}{\varepsilon_0}} + \frac{l}{\sigma \delta^2}(2j)}{\frac{1}{\sigma l} + \sqrt{\frac{\mu_0}{\varepsilon_0}}} \qquad \text{Eq. 2.32}$$

In the numerator,

$$\left|\frac{l}{\sigma \delta^2}(2j)\right| = \frac{l}{\delta} \cdot \frac{1}{\sigma \delta} \cdot 2 \qquad \text{Eq. 2.33}$$

$$\frac{1}{\sigma \delta} = \frac{1}{\sigma \sqrt{\frac{2}{\omega \mu_0 \sigma}}} = \sqrt{\frac{\omega \mu_0}{2\sigma}} << \sqrt{\frac{(\sigma / \varepsilon_0)\mu_0}{2\sigma}} = \sqrt{\frac{\mu_0}{2\varepsilon_0}} \approx \sqrt{\frac{\mu_0}{\varepsilon_0}} \qquad \text{Eq. 2.34}$$

l/δ is small and $(\sigma\delta)^{-1}$ is also much smaller than $\sqrt{\mu_0 / \varepsilon_0}$. Therefore, the input characteristic impedance can be approximated as

$$\eta_{in} \approx \frac{\frac{1}{\sigma l}\sqrt{\frac{\mu_0}{\varepsilon_0}}}{\frac{1}{\sigma l} + \sqrt{\frac{\mu_0}{\varepsilon_0}}} = \frac{R_s \cdot \eta_0}{R_s + \eta_0} \qquad \text{Eq. 2.35}$$

$$R_s = \frac{1}{\sigma l} \qquad \text{Eq. 2.36}$$

These results are the same as the results from the transmission models in Figure 2.11.

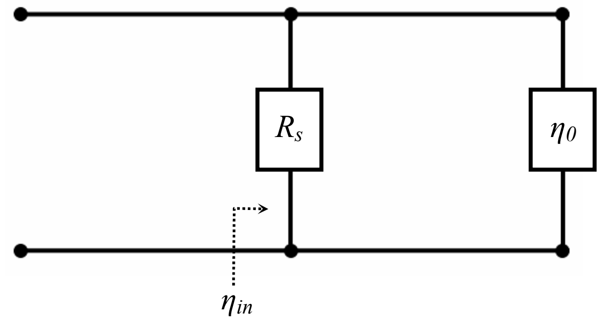

Figure 2.11: Transmission model approximately equivalent with the model in Figure 2.10. Finite thick bolometer layers can be represented by the infinitely thin conductive sheets.

Consequently the infinitely thin conductive sheets can represent finite thick bolometer layers, and its sheet resistance can be realized by a combination of the electric conductivity σ and the thickness l. For the applications of infrared detection, materials with small conductivity such as vanadium oxide are required since the thickness of materials with large conductivity to satisfy the designed sheet resistance is physically too thin.

2.3 VERIFICATION OF EISENHART AND KHAN MODEL BY 'HFSS [24]'

One of the primary goals of this dissertation is the demonstration of a planar multimode antenna that can substantially improve the wavelength selectivity of an infrared microbolometer. Our prior work has focused on the use of a Genetic Algorithm (GA) as an optimization scheme. Since a typical grid has at least five design parameters (the distance d between the multimode array pixels and the mirror, the array period a, the gap width g, the post width w, and the bolometer sheet resistance R_s, Figure 2.3) a key requirement when performing such optimizations is the numerical efficiency of the electromagnetic model. For that reason we have used a somewhat simplified modematching technique (the so-called Eisenhart and Khan model [21, 22]) for the array design. Typical results from such a model are shown in Figure 2.8.

We have recently completed extensive full wave electromagnetic simulations to verify the wavelength selective multi-mode antenna designs previously found using the Eisenhart and Kahn model. We have used the commercial finite element full wave simulation program Ansoft HFSS [24]. To verify that the boundary set-up of the HFSS simulation is correct, we first simulated the spectral responses of a simple Salisbury Screen (i.e., the conventional structure used for a micromachined microbolometer) and compared the finite element results against those from well-known transmission line theory for plane waves. Figure 2.12 (a) illustrates the HFSS simulation space, and Figure 2.12 (b) shows the comparison between the HFSS calculation and simple plane wave analysis; the agreement is excellent, demonstrating that the finite element boundaries have not introduced spurious reflection.

Next we simulated the electromagnetic behavior of the planar multimode detectors and compared them to the results from the modified post mount analysis of Eisenhart and Khan. One of the advantages of the Eisenhart and Kahn model is that its calculation time is very fast compared to full-wave electromagnetic simulations such as the FEM (Finite Element Method) used in HFSS. If the Eisenhart and Kahn model is reliable, it would be very useful in the time consuming calculation used for numerical optimizations. For our first comparison a set of dimensions was selected in which the metal part is very small compared to the array period, while the resistive “post” is quite large. Thus, its spectral response is similar to those of a Salisbury Screen (as in Figure 2.12 (b)). Figure 2.13 shows the results; based upon the good agreement between the results of the Eisenhart and Kahn model and HFSS, we can say that the Eisenhart and Kahn model is reliable for this geometry.

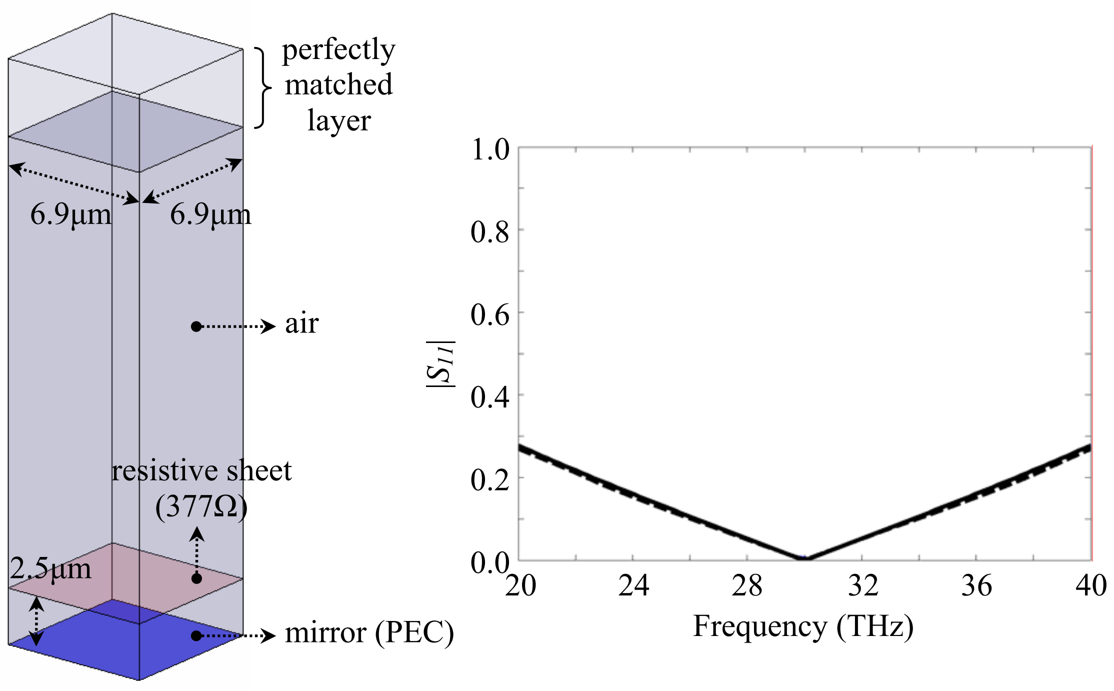

(a) (b)

Figure 2.12: (a) HFSS configuration designed to generate a resonance at 30THz. (b) The HFSS-simulated results (solid curve) show good resonance at 30THz, in agreement with the simple transmission line plane wave model (dashed curve).

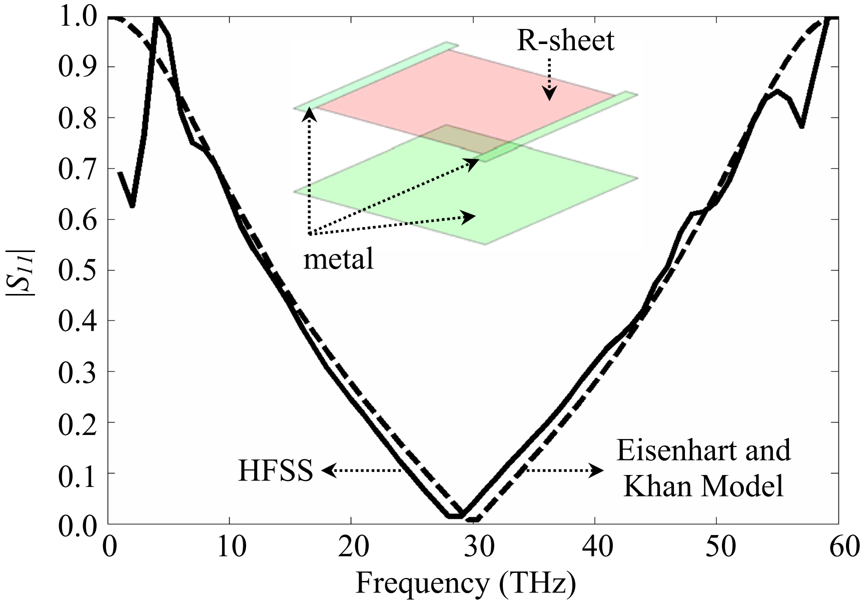

Figure 2.13: HFSS simulation (solid curve) of an array with period a=6.9μm, resistive post width w=6.0μm, gap g=6.0μm, and air gap thickness d=2.5μm; this is almost the same as a simple Salisbury screen. Agreement between Eisenhart and Khan (dashed curve) and HFSS (solid curve) is good.

We then selected one of the designed wavelength selective grids in Figure 2.8. As shown in Figure 2.14, both the size of the resonance in absorbed power and the line shape again show reasonably good agreement between the HFSS calculation and the Eisenhart and Kahn model. To confirm that the grid designs produce narrower spectral absorption than a Salisbury screen (i.e., exhibit higher spectral selectivity than current micromachined microbolometers) we tested another set of dimensions, with results shown in Figure 2.15. In this case there is some difference between the Eisenhart and Kahn model and the HFSS calculations, although the overall trends still match. To confirm that power is in fact absorbed by the resistive microbolometers another HFSS calculation was performed to compare the reflected power with and without a resistor present in the simulation. Figure 2.16 clearly shows that if the resistor is removed then essentially no power is absorbed by the grid. The ripples present in the simulation are due to the finite precisions with which the finite element model can represent these structures.

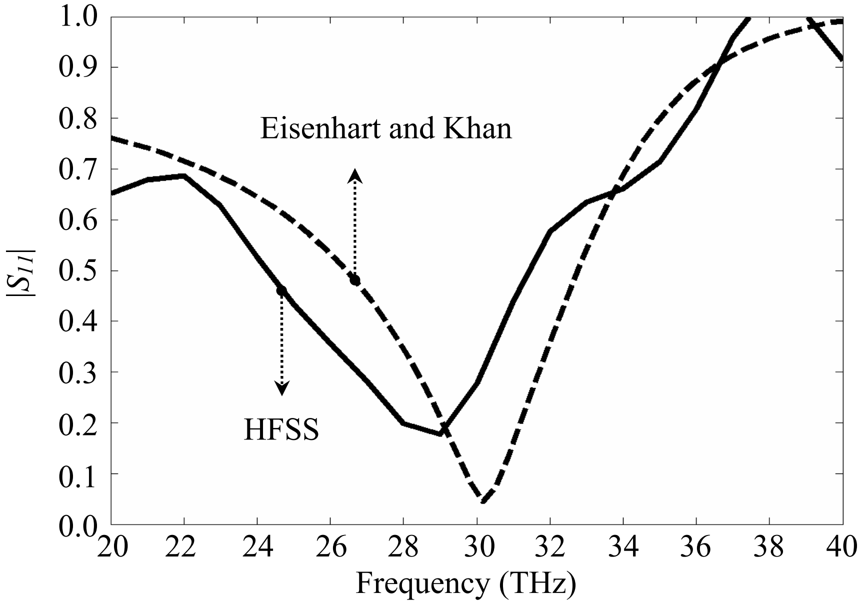

Figure 2.14: HFSS simulation of an array with wavelength selectivity, period a=5.3μm, gap g=1.0μm, resistive post width w=0.96μm, distance to mirror d=3.61μm, and bolometer sheet resistance R_S=30Ω; agreement between 'Eisenhart and Khan' and 'HFSS' is again reasonably good.

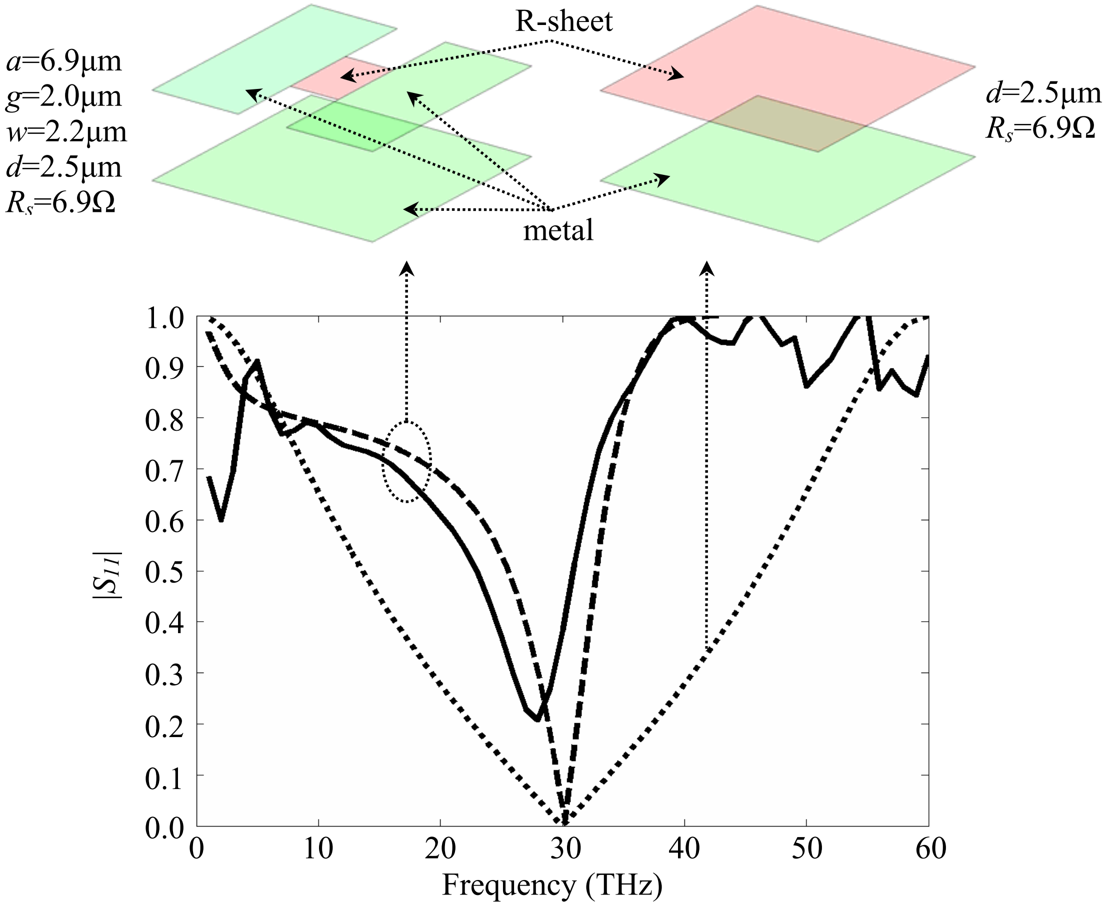

Figure 2.15: HFSS simulation (solid curve) of an array with wavelength selectivity compared to calculations from the Eisenhart and Khan model (dashed curve), both compared to conventional Salisbury screen (dotted curve). This full-wave finite element calculation confirms the grid produces wavelength selectivity.

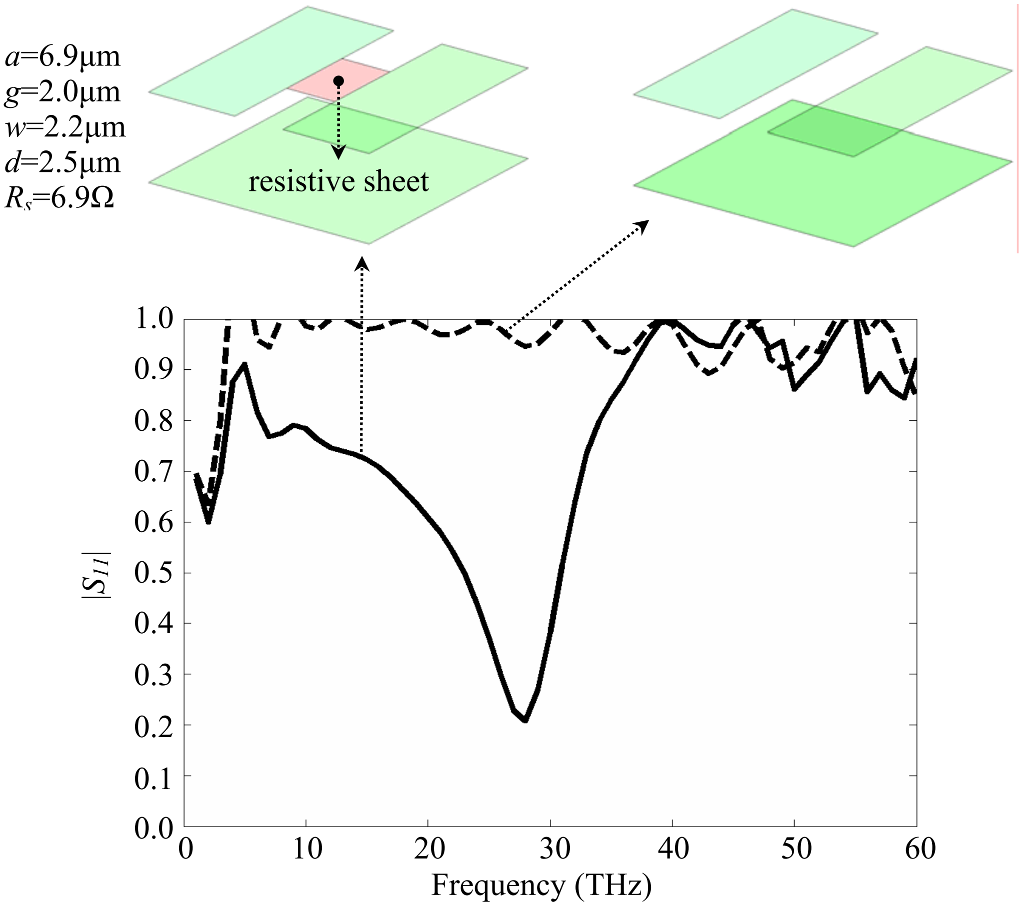

Figure 2.16: HFSS simulation of an array with and without a resistive element; the dip in the red curve is the wavelength selective absorption of power by the bolometric element.

Chapter 3: Wavelength Selective Planar Multimode Detectors

Multimode microbolometers for wavelength-selective infrared detection have been designed using a Genetic Algorithm and an electromagnetic model of the planar antenna [15, 25]. Wavelength selectivity can be varied by mechanical actuation or changing lithographically drawn parameters, with bandwidth narrower than the Salisbury Screens. The design of a three color system covering the 7-14μm band is presented.

3.1 INTRODUCTION OF WAVELENGTH SELECTIVITY

Multi-channel, wavelength selective infrared detection has been of interest because it permits rapid and efficient understanding of the scene in a variety ways. It can discriminate both absolute temperature and unique spectral signatures of objects in the scene so as to subtract spurious information leaving only the objects of interest. Hence it has been extensively studied for numerous applications such as target acquisition, battlefield assessment, missile guidance and defense, surveillance, night vision, thermal imaging, nondestructive detection, medical diagnostics, remote sensing, and so on. Furthermore, the 7~14μm infrared band of the electromagnetic spectrum is known as the "fingerprint" region since it exhibits an abundance of molecular resonances: vibration, rotational, and low-lying electronic transitions which provide highly detailed and precise information. Consequently the multi-spectral infrared detection over 7~14μm infrared band can give information that a single-spectral infrared detection can not give.

For the wavelength selectivity, a narrow bandwidth is required. In cooled ways, the narrow bandwidth has been achieved by using quantum-well infrared photodetectors (QWIPs) [26], quantum-dot infrared photodetectors (QDIPs) [27], or infrared bandpass filters in front of microbolometers [28]. For conventional uncooled micromachined infrared microbolometers integrating wavelength selectivity into the detector itself is somewhat harder to achieve. The most common approach to both enhance coupling and produce some degree of wavelength selectivity is the use of the Salisbury Screen, consisting of a microbolometer placed in front of a mirror [29-31]. However, a simple Salisbury Screen (Figure 3.1) produces a fairly broad spectral response. Here we use the planar multimode detectors that can substantially improve the wavelength selectivity of a microbolometer.

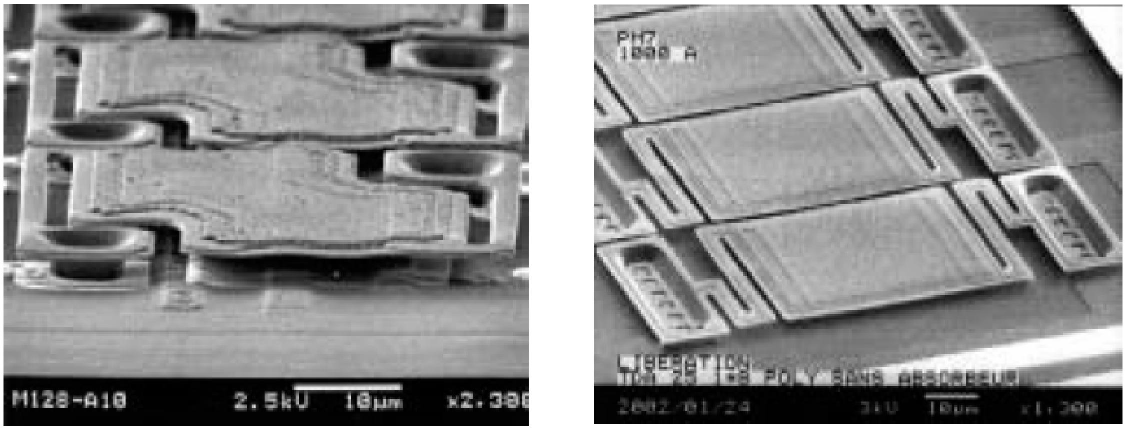

(a) (b)

Figure 3.1: Salisbury Screens [32]. (a) Standard 50µm bridge. (b) 39µm bridge for high density linear array.

As discussed in Chapter 2, the diversity of the solutions is an advantage of the planar multimode detectors, allowing a search for desired characteristics. Here the genetic algorithm (GA) was adopted as an optimization scheme. The design goal for the wavelength selectivity is to maintain strong absorption at a specified wavelength within the 7~14µm infrared band while minimizing the absorption bandwidth of the antenna about that wavelength. To locate narrow bandwidth array designs that couple strongly at a desired wavelength, we have used a cost definition for the GA that seeks at least 99% power absorption at a specified wavelength, while minimizing the power absorbed at other wavelengths. This is accomplished by minimizing the area under the absorption curve.

$$\begin{cases} \text{if } \eta \,\big|_{\text{designated } \lambda} > 0.99 & cost = \int_{7\mu m}^{14\mu m} \eta(\lambda) d\lambda \\ \quad \text{otherwise} & cost = \infty \end{cases} \qquad \text{Eq. 3.1}$$

where η is the power absorption efficiency. The narrowest bandwidth curve in Figure 2.8 (solid line) is the result found by the GA using the above cost function for a center wavelength of 10µm.

Figure 3.2 shows the ideal power absorption efficiencies for 3-color detection in a given wavelength band. These shapes indicate that each pixel has unity absorption over its designated wavelength band, and zero absorption over other wavelength bands. There are no overlapped regions which would make it hard to identify the incoming wavelength. Identifying incoming wavelengths can give an abundance of information such as what a given material is composed of. Notice that as the wavelength bandwidth narrows, the number of channels increases and the information becomes more detailed.

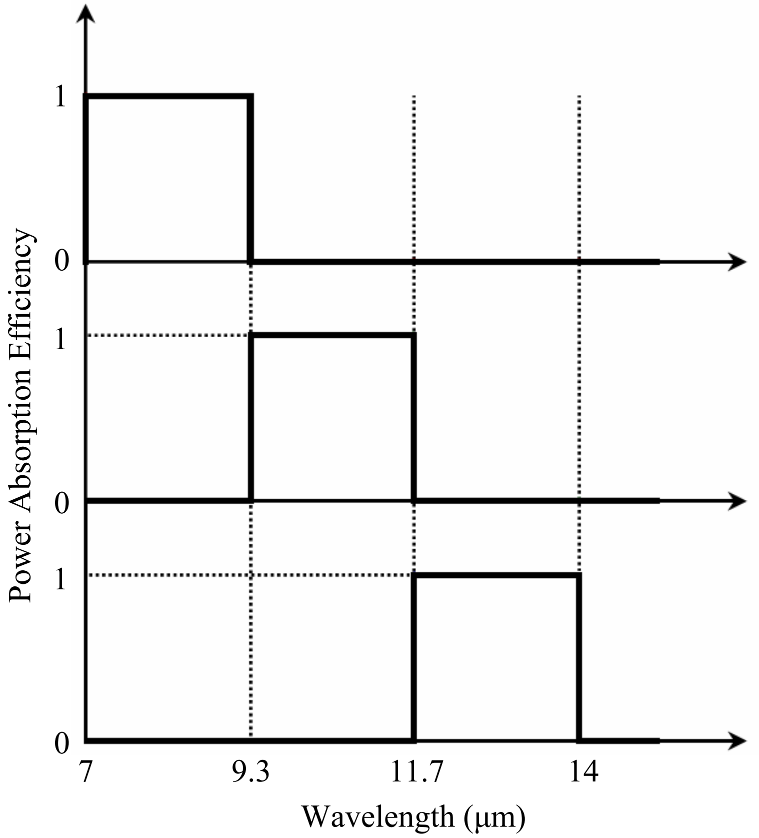

Figure 3.2: Ideal power absorption efficiencies for 3-color detection in 7~14µm band.

3.2 GENETIC ALGORITHM (GA)

Recently, the Genetic Algorithm (GA) has been used in many applications since it can provide a mechanism for global search, simplicity, and ease of implementation when compared to gradient-based search procedures, and results in a number of high-performance designs rather than a single solution as offered by other techniques [33-35]. The concept of the GA is formalized by Holland [36], and extended to functional optimization by De Jong [37]. The GA is a stochastic search procedure modeled on the Darwinian concepts of natural selection and evolution. In GA, a set population (set of trial solutions) of potential solutions is to evolve toward a global optimal solution. Evolution toward a global optimum occurs as a result of pressure exerted by a fitnessweighted selection process. Exploration of the solution space is accomplished by recombination (also known as crossover) and mutation of existing characteristics present in the current population [38]. Figure 3.3 shows block diagrams of the simple GA.

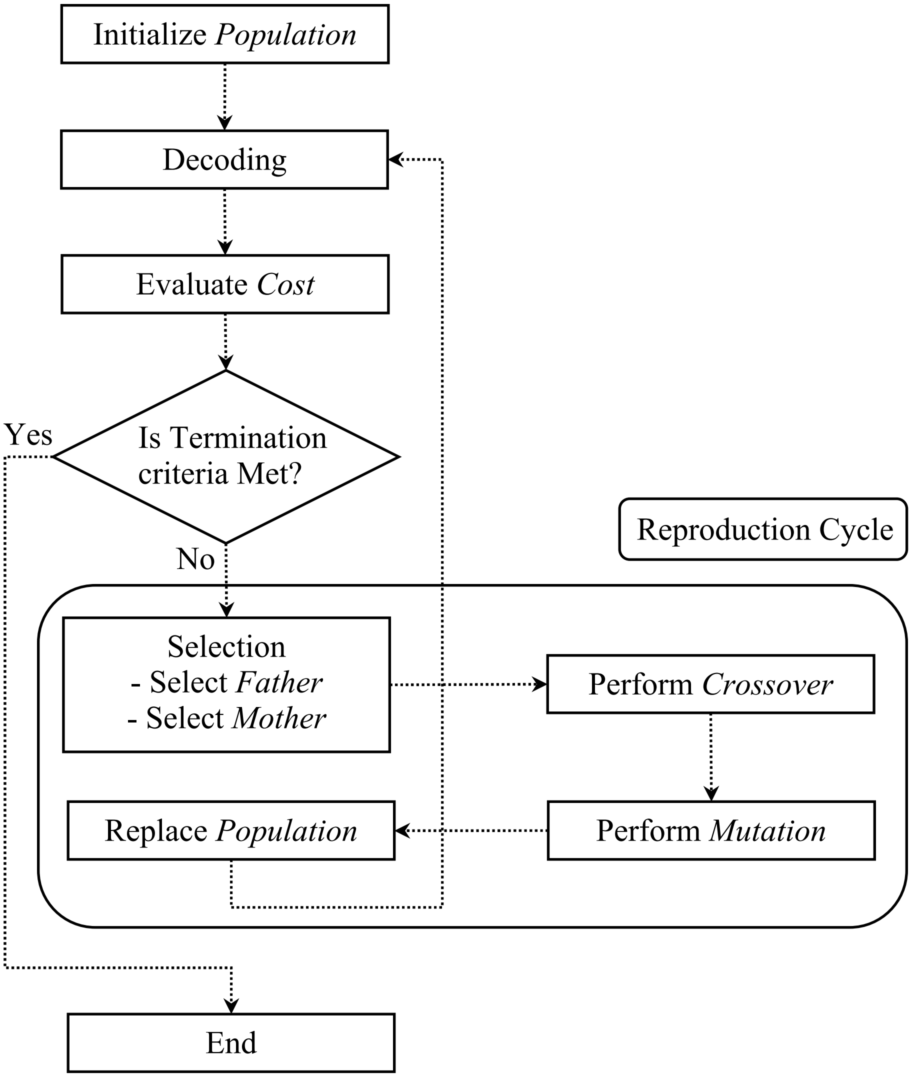

Figure 3.3: Block diagrams of the simple Genetic Algorithm [38].

3.3 TUNING OF WAVELENGTH SELECTIVITY BY MECHANICAL ACTUATION

Based on the array behavior of the planar multimode detector discussed in Chapter 2, we consider tuning wavelength selectivity by changing the distance to the mirror *d*, which could be performed using mechanical actuation (Figure 3.4). Here, we set three wavelengths, 8μm, 10μm, and 12μm, as the designated wavelengths that should be reached using the tuning mechanism.

First of all, we fix the array dimension (*a*, *g*, *w*, and R_s) and then sweep *d* to see how *d* affects the power absorption efficiency η. The design used except *d* is the same as that which produced the solid line in the Figure 2.8. Figure 3.5 shows the contour plots of the power absorption efficiency versus wavelength and distance to the mirror *d* for the fixed array dimension above. As seen in the solid line in Figure 2.8, it has decent power absorption efficiency at 10μm wavelength when *d* is about 3μm. Similarly, we can make the high absorption at 12μm wavelength by approaching *d* to about 5.7μm. However, this shift results in unnecessary high absorption around 10μm wavelength, which makes it hard to identify the incident waves. In addition, the power absorption at 8μm wavelength achieved by setting *d*=0.2μm is way too low. Consequently, redundant and ambiguous power absorption resulting from long wavelength absorption and low power absorption at short wavelength region make tuning by the distance *d* unattractive even though the mechanical actuation of planar multimode detectors provides better wavelength selectivity than the conventional Salisbury Screen.

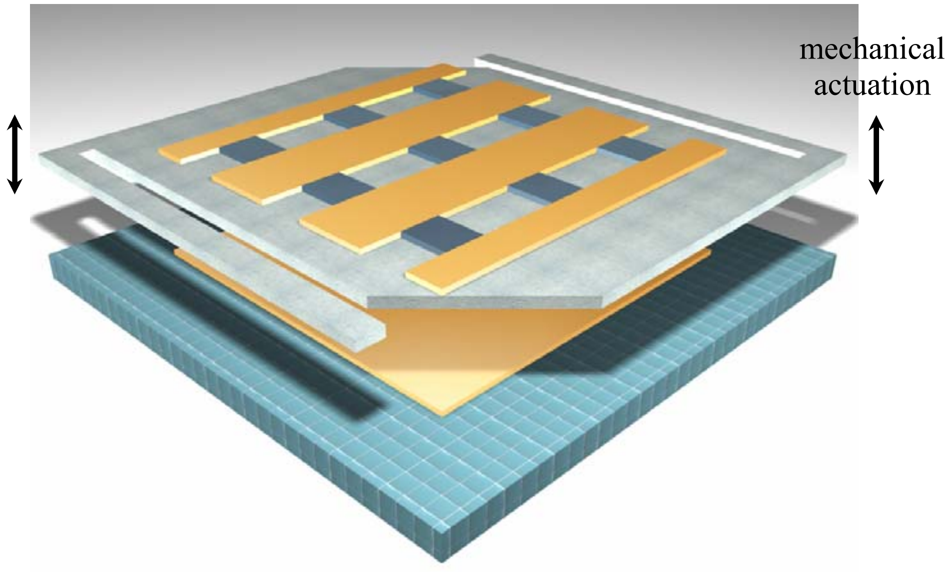

Figure 3.4: Tunable wavelength selective focal plane array using the planar multimode detectors by mechanical actuation.

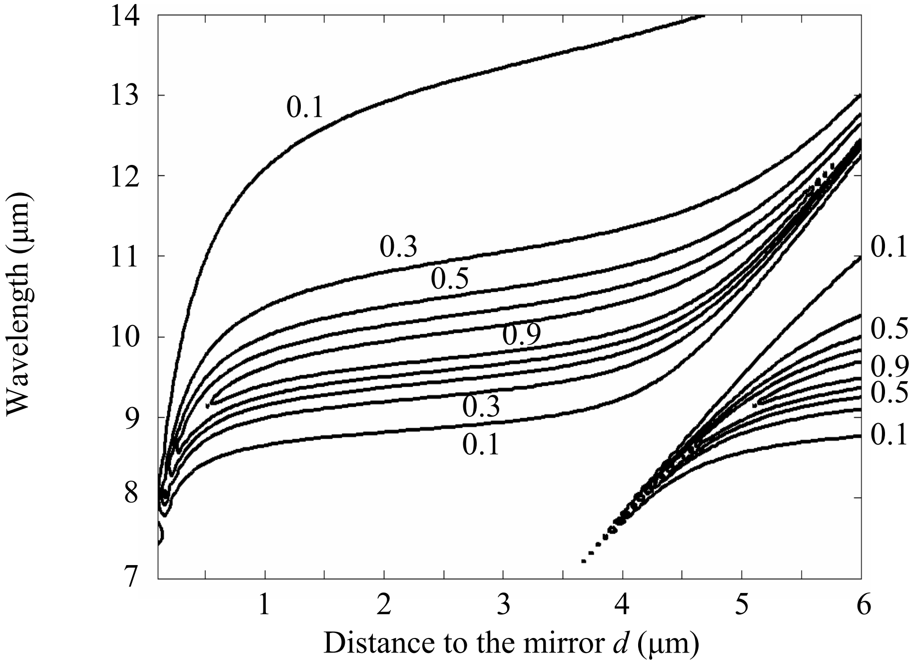

Figure 3.5 The contour plots of the power absorption efficiencies versus wavelength and the distance to the mirror *d*. Tuning wavelength selectivity can be achieved by mechanical actuation. Here *a*, *g*, *w*, and R_s are 6.90μm, 0.20μm, 3.0μm, and 53.49Ω, respectively.

It is possible, however, to find a set of array dimensions that does allow tunable wavelength selective coupling using only the distance to the mirror as a tuning variable. Here we optimize for a fixed dimension array (*a*, *g*, *w*, and R_s all fixed) but with three different distances from the mirror each selected to maximize absorption at three designated wavelengths, 8μm, 10μm, and 12μm, using the following cost definition. This cost definition makes each channel as narrow as possible to identify the incident wavelengths, and as high as possible at the designated wavelength to absorb more power. Figure 3.6 shows the optimized results. By changing only *d* from 1.65μm to 5.10μm, each channel has high absorption at its own designated wavelength and its bandwidth is reasonably narrow. Here, the optimized *a*, *g*, *w*, and R_s for tuning by the distance *d* are 5.07μm, 1.42μm, 0.74μm and 21.04Ω, respectively.

$$\begin{cases} \text{if } C_1 > 0 \text{ and } C_2 > 0 \text{ and } C_3 > 0 \\ \quad cost = \dfrac{1}{C_1 + C_2 + C_3} \\ \qquad C_1 = \eta_{8\mu m}(8\mu m) - \max\left(\eta_{10\mu m}(8\mu m), \eta_{12\mu m}(8\mu m)\right) \\ \qquad C_2 = \eta_{10\mu m}(10\mu m) - \max\left(\eta_{8\mu m}(10\mu m), \eta_{12\mu m}(10\mu m)\right) \\ \qquad C_3 = \eta_{12\mu m}(12\mu m) - \max\left(\eta_{8\mu m}(12\mu m), \eta_{10\mu m}(12\mu m)\right) \\ \text{otherwise} \\ \quad cost = \infty \end{cases} \qquad \text{Eq. 3.2}$$

where $\eta_{\text{designated}\,\lambda}(\lambda)$ is power absorption efficiency at λ designed for the designated λ.

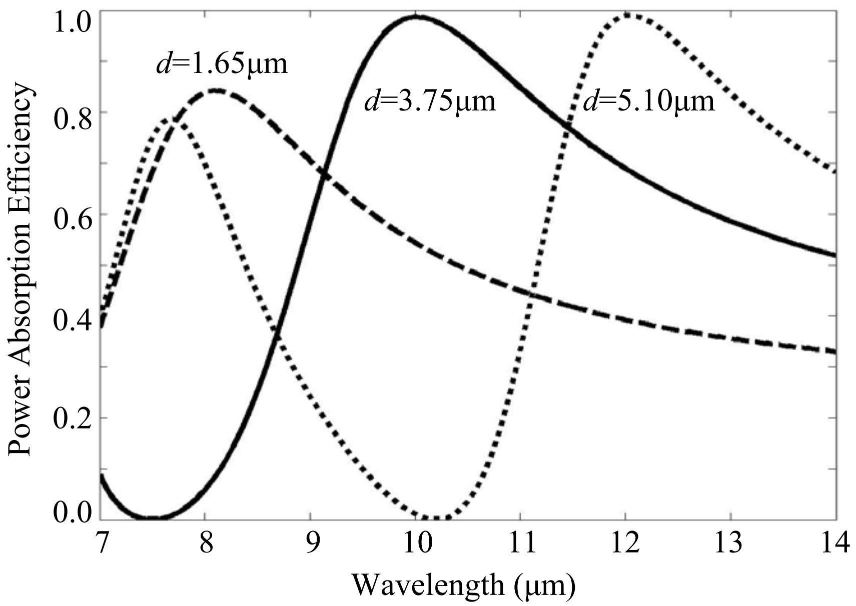

Figure 3.6: Successful accomplishment of the wavelength selectivity tuning by only changing the distance to the mirror *d*, which can be achieved by the simple actuation, on the planar multimode detectors with same *a*, *g*, *w*, and R_s: *a*=5.07μm, *g*=1.42μm, *w*=0.74μm, and R_s =21.04Ω.

3.4 DESIGN FOR WAVELENGTH SELECTIVITY

3.4.1 Different Sacrificial Layer Thicknesses for 3 Different Pixels

Next we design three separate pixels, each with peak spectral response at a different wavelength, each located at their optimum distance from the tuning mirror (Figure 3.7). This could be used to produce a three color array, but would require a process using different sacrificial layer thicknesses for each of the pixels. For each pixel, our design goal is to maintain strong absorption at a specified wavelength within the 7~14μm infrared band while minimizing the absorption bandwidth of the antenna about that wavelength. To locate narrow bandwidth array designs that couple strongly at a desired wavelength, we have used a cost definition for the GA that seeks at least 99% power absorption at a specified wavelength, while minimizing the power absorbed at other wavelengths. This is accomplished by minimizing the area under the absorption curve, as given by

$$\left\{\begin{array}{l} \text{if Power Absorption Efficiency}\Big|_{designated\ \lambda} > 0.99 \\ \qquad cost = \int_{7\mu m}^{14\mu m} \text{Power Absorption Efficiency}\left(\lambda\right) d\lambda \\ \text{otherwise} \\ \qquad cost = \infty \end{array}\right. \qquad \text{Eq. 3.3}$$

Figure 3.8 illustrates the optimized results for three pixels. All power absorption efficiencies are high at the desired wavelengths and narrow enough to distinguish infrared colors independently. Specific design geometries for Figure 3.8 are given in Table 3.1. Here the most dominant factor for shifting an absorption wavelength is a post width *w*. Notice that *a*, *g*, *d*, and R_s are similar for all three designs. The narrowest bandwidth curve in Figure 3.8 (solid line) is the result found by the GA using the cost function given above for a center wavelength of 10µm.

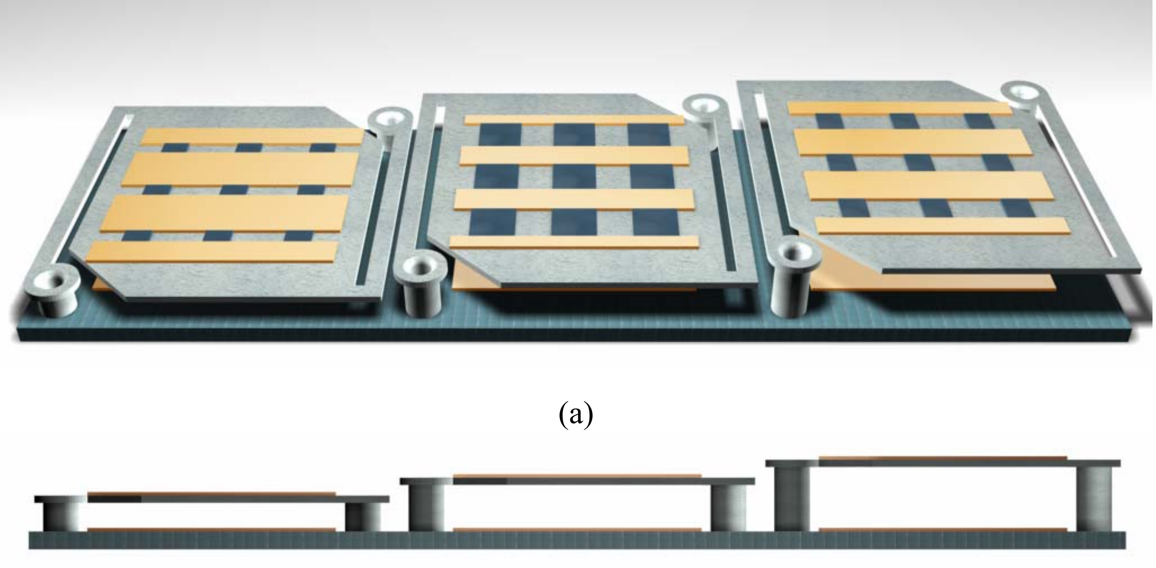

(a)

(b)

Figure 3.7: Pixels located in parallel for wavelength selectivity which does not require mechanical actuation. (a) Perspective view. (b) Front view.

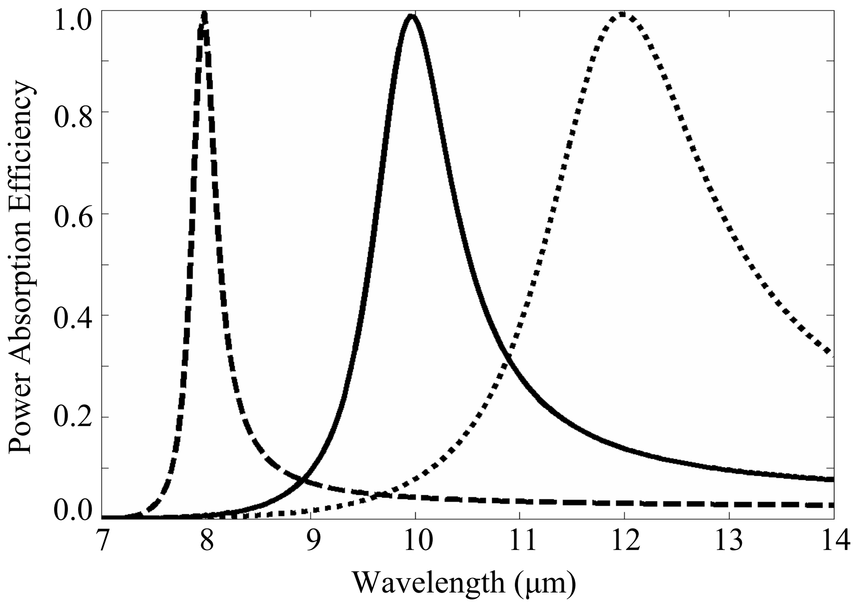

Figure 3.8: Three-color design found by optimizing three different multimode pixel geometries, each with different lithographically drawn dimensions *a*, *g*, and *w*, *d*, and R_s. Power absorption efficiencies are almost unity at designated wavelengths while each pixel would have enough wavelength selectivity to clearly distinguish three colors. All specific design geometries are given in Table 3.1.

	dashed	solid	dotted
a	6.90μm	6.90μm	6.90μm
g	0.18μm	0.20μm	0.18μm
w	4.77μm	3.00μm	1.50μm
d	3.00μm	3.29μm	3.31μm
R_s	55.18Ω	53.49Ω	62.94Ω

Table 3.1: Specific designs yielding response curves given in Figure 3.8

3.4.2 Same Sacrificial Layer Thickness for 3 Different Pixels

From a fabrication perspective it would be very useful if it were possible to produce three pixels with desired spectral response but all using an identical value for *d* (the distance between the bolometer and the mirror) like Figure 3.9. The only method available for changing wavelength selectivity in a conventional Salisbury Screen is by changing the distance *d* between the bolometer and the mirror. Hence, to construct a multi-wavelength focal plane array (i.e., one in which different pixels have different wavelength selectivities) would require a fabrication process with different sacrificial layer thicknesses under different pixels in the array. This could result in a complex process and high cost. Here we study only designs with identical distance *d* between the multimode array pixels and the mirror, changing the wavelength selectivity of each pixel by changing only the lithographically drawn parameters: the array period *a*, the capacitive gap width *g*, and the inductive post width *w*. To further simplify the fabrication of such a multi-color focal plane array, we have also constrained the bolometer sheet resistance R_s to be constant for all pixels, allowing the use of a single bolometric material.

To find a three color design, the cost function for the GA is modified as follows. We require that three different multimode pixels, each with different dimensions *a*, *g*, and *w*, be found such that each pixel absorbs at least 99% at its designated center wavelength, while total out of band power absorption be minimized; this leads to an eleven parameter design search, a_1, g_1, w_1, a_2, g_2, w_2, a_3, g_3, w_3, d, and R_s. Here we selected the center wavelengths of 8, 10 and 12μm. The corresponding cost function for the GA is given by

$$\begin{cases} \text{if } \eta_{8\mu\text{m}}(8\mu m) > 0.99 \text{ and } \eta_{10\mu\text{m}}(10\mu m) > 0.99 \text{ and } \eta_{12\mu\text{m}}(12\mu m) > 0.99 \\ \qquad cost = \int_{7\mu m}^{14\mu m} \left\{\eta_{8\mu\text{m}}(\lambda) + \eta_{10\mu\text{m}}(\lambda) + \eta_{12\mu\text{m}}(\lambda)\right\} d\lambda \\ \text{otherwise} \\ \qquad cost = \infty \end{cases} \qquad \text{Eq. 3.4}$$

where $\eta_{\text{designated}\,\lambda}(\lambda)$ is the power absorption efficiency at the designated center wavelengths.

Figure 3.10 shows the GA optimized results. The GA selected an array to mirror distance *d* of 3.14µm, bolometer sheet resistance of 56.6Ω, the same array period *a* and gap width *g* for all three different wavelength selective pixels (6.8µm and 0.20µm, respectively), with the only difference being in the post width *w*: the 8 micron pixel would have a post width of 4.57µm: the 10 micron pixel would have a post width of 2.80µm: and the 12 micron pixel would have a post width of 1.30µm. Power absorption efficiencies are almost unity at the designated wavelengths while each pixel would have enough wavelength selectivity to clearly distinguish three colors.

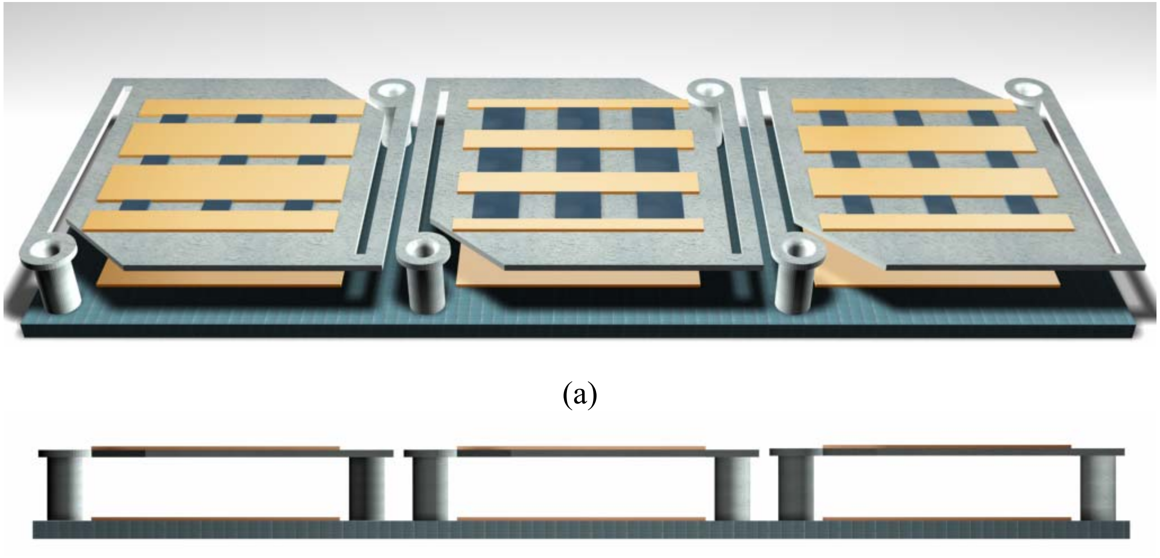

(a)

(b)

Figure 3.9: Pixels located in parallel for wavelength selectivity which does not require mechanical actuation. (a) Perspective view. (b) Front view.

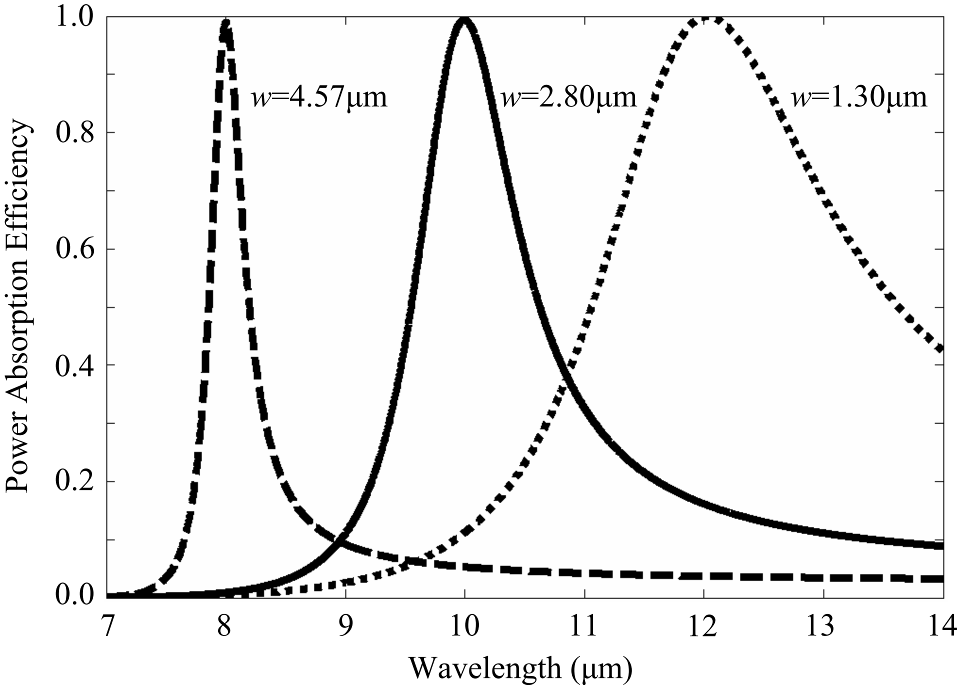

Figure 3.10: Three-color design found by optimizing three different multimode pixels in Figure 3.9, each with different lithographically drawn dimensions *a*, *g*, and *w*, with identical *d* and R_s. *a*, *g*, *d*, and R_s are 6.80μm, 0.20μm, 3.14μm, and 56.6Ω, respectively.

Chapter 4: Uncooled and Stacked Microbolometer Array for Multi-Spectral Imaging

In this chapter we present the stacked planar multimode detectors designed for 2-color wavelength selectivity in 7~14μm band.

4.1 INTRODUCTION

In Chapter 3, the wavelength selective tiled microbolometers have been introduced for multi-spectral imaging. Another approach to achieve multi-spectral imaging capabilities using microbolometer arrays would be the use of a ‘stackable’ array. In cooled ways, multi-color infrared detection has been constructed by vertical stacking using quantum well infrared photodetectors (QWIPs) or quantum dot infrared photodetectors (QDIPs) [39-41]. Figure 4.1 shows a schematic view of stacked QWIPS for 2-color detection and a top view of actual pixels [39]. Ideally in the stacked configuration, each ‘layer’ would absorb a narrow band of wavelengths, while allowing all other wavelengths to be transmitted. This is a very challenging problem from an electromagnetics perspective. It is fundamentally difficult to produce a layer that is strongly absorbing over only a narrow band while being ‘transparent’ out-of-band. We have performed initial designs using the planar multimode detectors discussed in Chapter 2 in an attempt to produce a stackable system. The basic requirements are that a given layer strongly absorbs the target wavelengths, while strongly transmitting out-of-band wavelengths, and while not reflecting out-of-band wavelengths since reflections will cause interference with other layers above.

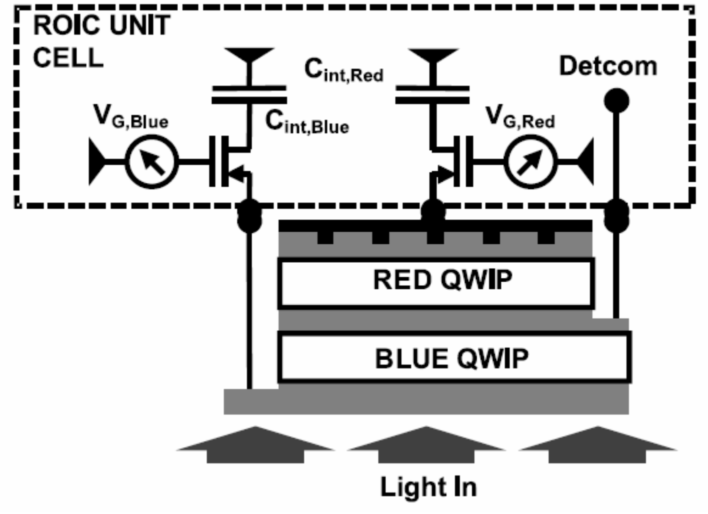

(a)

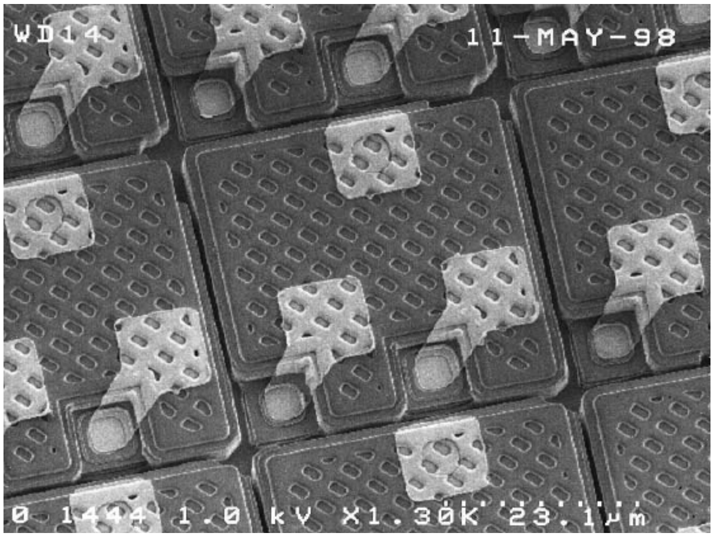

(b)

Figure 4.1: (a) Schematic view of stacked quantum well infrared photo-detectors (QWIP) [39]. (b) Top view of 2-color focal plane array pixels [39].

4.2 STACKABLE PLANAR MULTIMODE DETECTORS

The planar multimode detector without a mirror (Figure 4.2) can be positive in the 'stacked' scheme for multi-spectral imaging since it can provide the basic requirement for vertical stacking, in-band absorption and out-of-band transmission. When an absorbing sheet with an impedance Z is located in between the free space, there is a natural limit of the power absorption efficiency. Figure 4.3 illustrates the transmission line model of Figure 4.2. In Figure 4.3, the input impedance Z_{in} is defined as

$$Z_{in} = Z // \eta_0 \qquad \text{Eq. 4.1}$$

and the reflection coefficient Γ is

$$\Gamma = \frac{Z_{in} - \eta_0}{Z_{in} + \eta_0} = -\frac{\eta_0}{\eta_0 + 2Z} \qquad \text{Eq. 4.2}$$

$$|\Gamma| = \frac{\eta_0}{\eta_0 + 2Z} \qquad \text{Eq. 4.3}$$

The power absorption efficiency can be determined as

$$\begin{aligned} &\text{power absorption efficiency} = 1 - \left(|\Gamma|^2 + |T|^2 \right) \\ &= 1 - \left[|\Gamma|^2 + (1 - |\Gamma|)^2 \right] = -2\left(|\Gamma| - \frac{1}{2} \right)^2 + \frac{1}{2} \end{aligned} \qquad \text{Eq. 4.4}$$

Consequently the maximum power absorption efficiency is 0.5 when |Γ| is 0.5, i.e., Z=0.5η_0. Based on this observation, ideal power efficiencies for in-band absorption and out-of-band transmission using the configuration in Figure 4.2 can be plotted as Figure 4.4. Figure 4.4 is prepared for 2-color detection as a reference to compare against Figure 4.5.

Figure 4.5 shows absorbed, transmitted, and reflected power efficiencies as a function of wavelength for the planar multimode detector without the mirror. The curve shapes in Figure 4.5 are reasonably comparable with ideal shapes in Figure 4.4 even though the power reflection efficiencies at long wavelength region in Figure 4.5 are a bit high compared to those in Figure 4.4. Note that the highest efficiency at longer wavelength region is power absorption efficiency, and the highest efficiency at shorter wavelength region is power transmission efficiency in a given 7~14μm band. This means that the absorption is strong at longer wavelength region and reasonably transmissive at shorter wavelengths in 7~14μm band. Therefore, the planar multimode detectors are stackable for the wavelength selectivity.

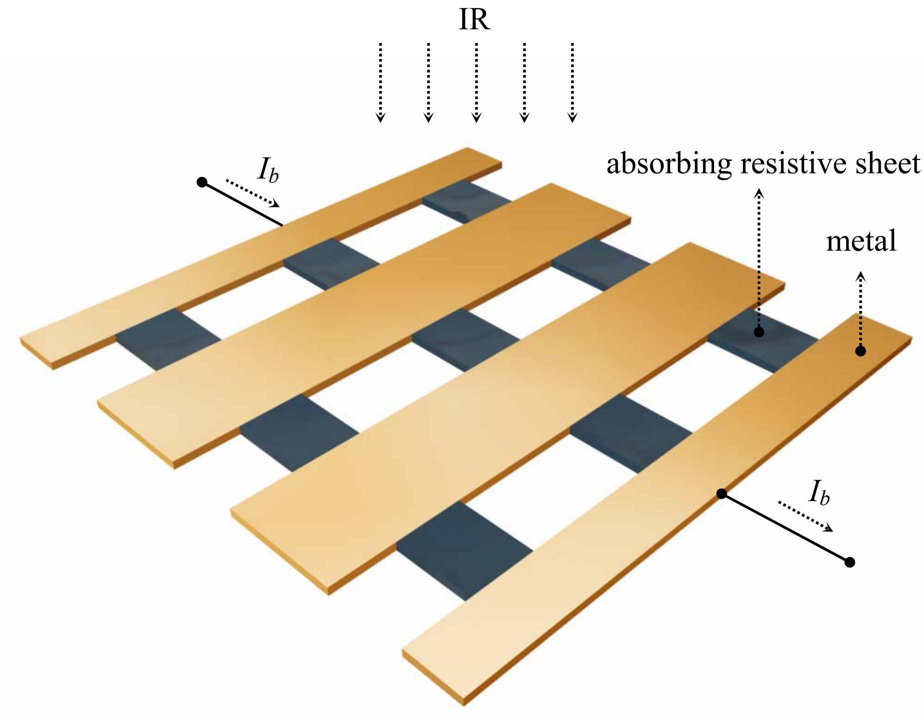

Figure 4.2: Planar multimode detector without a mirror.

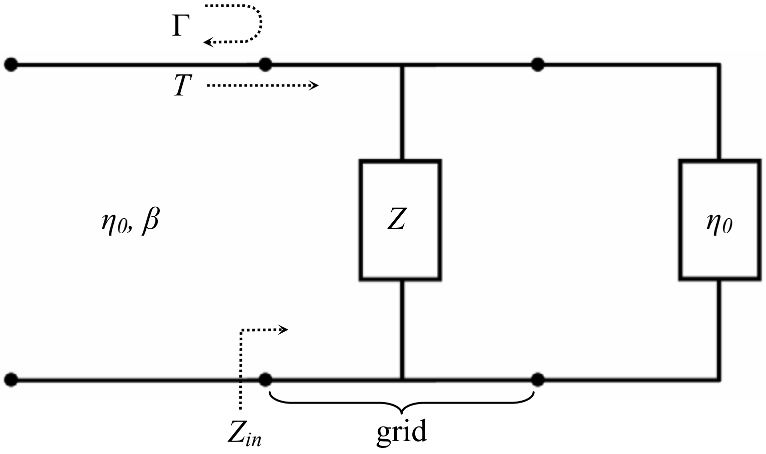

Figure 4.3: Transmission line model of the geometry in Figure 4.2 when the planar multimode detector without the mirror is located in between the free space.

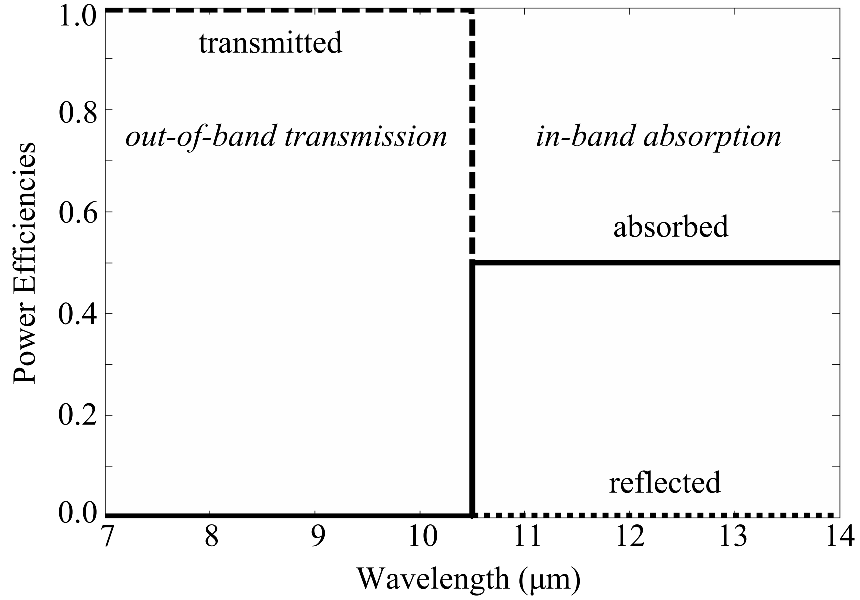

Figure 4.4: Ideal power absorption efficiencies for in-band absorption and out-of-band transmission using the configuration in Figure 4.2. These are assumed for 2-color detection. Notice that maximum power absorption efficiency is 0.5.

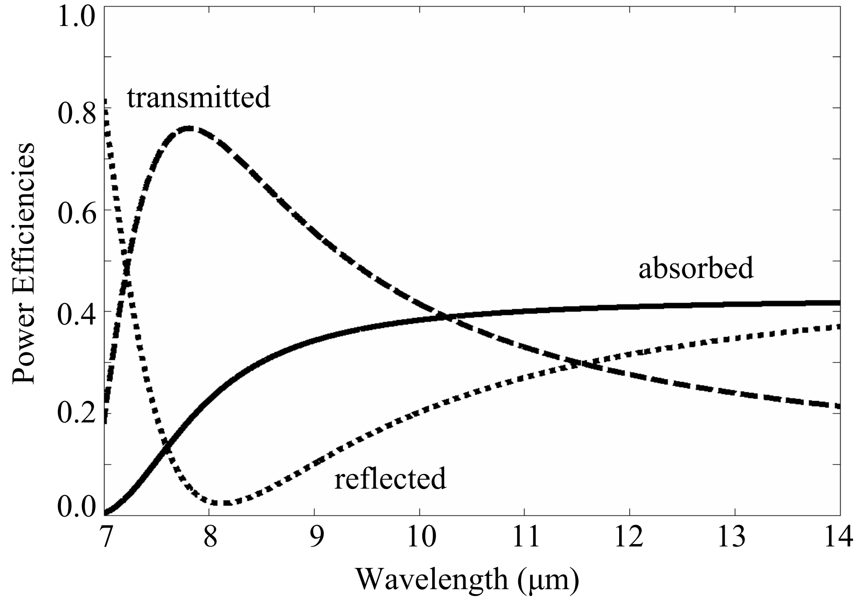

Figure 4.5: Spectral response of the planar multimode detector without a mirror. The solid, dashed, and dotted lines are power absorption efficiency, power transmission efficiency, and power reflection efficiency, respectively. (a=6.9μm, g=3.5μm, w=2.5μm, and R_s =60Ω).

4.3 Stacked Planar Multimode Detectors

In the previous section 4.2, we discussed that the planar multimode detectors are stackable. Figure 4.6 and 4.7 show the stacked planar multimode detectors and correspondent equivalent transmission line models. Here the design goal is for each stacked array to maintain strong absorption at a specified center wavelength within the 7~14μm infrared band while minimizing the absorption at the same center wavelength by the other stacked array; this leads to a ten parameter design search, the period a_1, the gap width g_1, the post width w_1, the bolometer sheet resistance R_{s1}, the distance between the top and bottom arrays d_1, a_2, g_2, w_2, R_{s2}, and the distance between the bottom array and the mirror d_2, where subscripts 1 and 2 represent the top and bottom multimode arrays, respectively. This goal makes it possible for stacked arrays to have enough wavelength selectivities to clearly distinguish two colors in the given band.

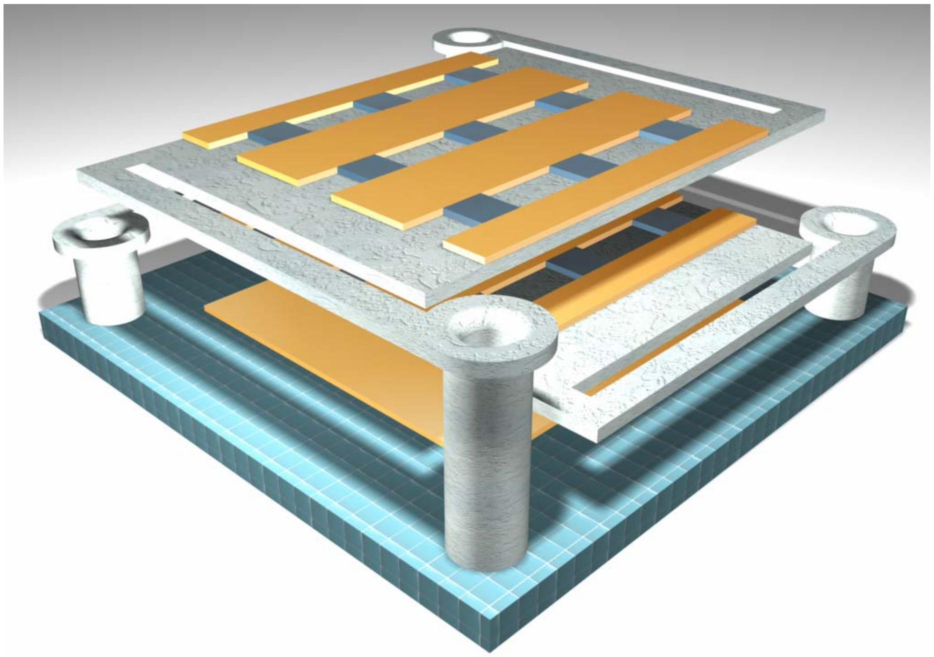

Figure 4.6: Stacked planar multimode detectors for the 2-color wavelength selectivity. Each layer absorbs its own designated wavelength band.

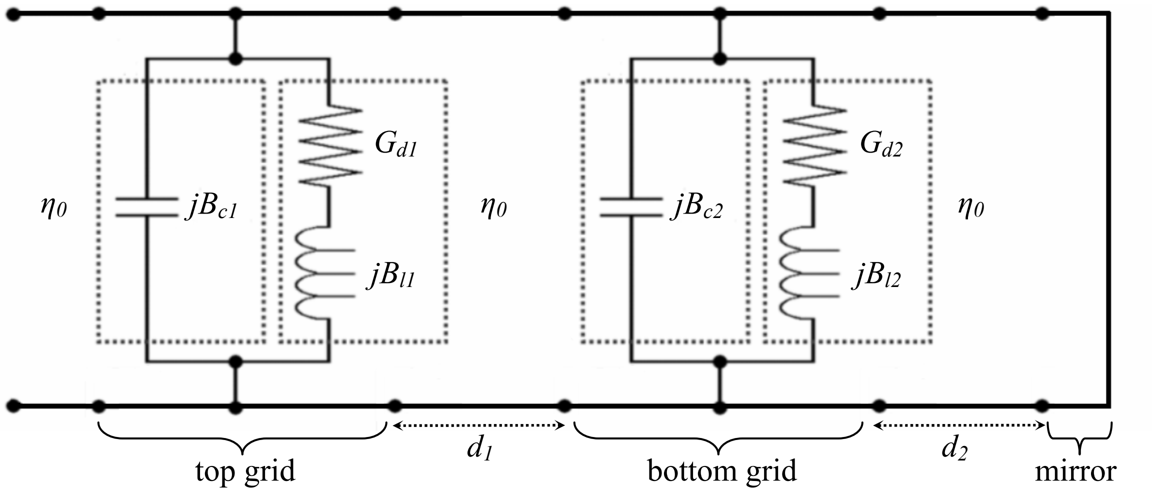

Figure 4.7: Transmission line model of the stacked planar multimode detectors in Figure 4.6.

We selected the center wavelengths of 8.5 and 12.5μm for two channels. The corresponding cost function for the GA is as follows. For the cost function to achieve the design goal, we define H_1 and H_2 as

$$\begin{aligned} H_1 &= \eta_{8.5\mu m}(8.5\mu m) - \eta_{12.5\mu m}(8.5\mu m) \\ H_2 &= \eta_{12.5\mu m}(12.5\mu m) - \eta_{8.5\mu m}(12.5\mu m) \end{aligned} \qquad \text{Eq. 4.5}$$

where $\eta_{\text{designated } \lambda}$ (λ) is the power absorption efficiency at the designated center wavelengths. In a simple manner, the design goal can be achieved by maximizing the sum of H_1 and H_2 so that the cost function is defined as

$$cost = \frac{1}{H_1 + H_2}. \qquad \text{Eq. 4.6}$$

Note that the lower the cost, the better the design. In the optimization process using this cost function, the cost is easily dominated by one factor, H_1 or H_2. This means that one layer has good wavelength selectivity but the other does not. To make both layers have good wavelength selectivities in their center wavelengths, both high and balanced H_1 and

H_2 are required. The following cost function has been defined to accomplish these requirements.

$$\begin{cases} \text{if } H_1 > 0 \text{ and } H_2 > 0, & cost = (\log_{10} H_1)^2 + (\log_{10} H_2)^2 \\ \text{otherwise}, & cost = \infty \end{cases} \qquad \text{Eq. 4.7}$$

Figure 4.8 illustrates the GA optimized results using this cost function. As expected both H_1 and H_2 are well balanced and reasonably high. The top multimode array absorbs short wavelength band and the bottom multimode array absorbs long wavelength band within 7 to 14μm infrared band while each stacked array would have enough wavelength selectivity to clearly distinguish two colors. a_1, g_1, w_1, R_{s1}, d_1, a_2, g_2, w_2, R_{s2}, and d_2 are 5.85μm, 4.25μm, 3.98μm, 980.9Ω, 2.10μm, 5.74μm, 3.38μm, 0.35μm, 37.4 Ω, 4.25μm, respectively. In addition, the vertically stacked multimode arrays are more compact and highly integrated structures than the Salisbury Screens located in parallel for the multi-spectral infrared detection.

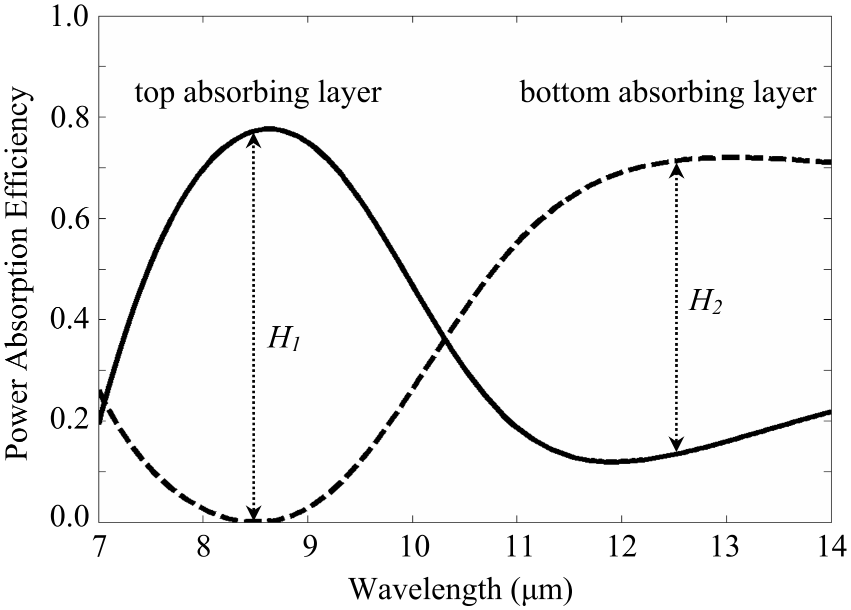

Figure 4.8: Two-color design found by optimizing stacked two different planar multimode detectors. Power absorption efficiencies are strong at the designated center wavelengths while each stacked multimode array would have enough wavelength selectivity to clearly distinguish two colors. a_1, g_1, w_1, R_{s1}, d_1, a_2, g_2, w_2, R_{s2}, and d_2 are 5.85μm, 4.25μm, 3.98μm, 980.9Ω, 2.10μm, 5.74μm, 3.38μm, 0.35μm, 37.4 Ω, 4.25μm, respectively.

As a reference we also optimize Salisbury Screens located in parallel (Figure 4.9) for 2-color infrared detection since the most common uncooled approach to both enhance coupling and produce some degree of wavelength selectivity is the use of the Salisbury Screen consisting of a microbolometer placed in front of a mirror. Figure 4.9 shows the GA optimized results using Salisbury Screens located in parallel for 2 channel infrared detections. Similarly as above, the optimization goal is for each Salisbury Screen to maintain strong absorption at 8.5 or 12.5μm center wavelengths while minimizing the absorption at the same center wavelength by the other Salisbury Screen. The solid line in Figure 4.9 is designed to absorb a band centered at 8.5μm wavelength while the dashed line in Figure 4.9 is designed to absorb a band centered at 12.5μm. Around 12.5μm wavelength, the system shows good wavelength selectivity. However, it reveals big overlapped regions over 7 to 9μm and 10 to 12μm band, which results in the ambiguity of absorbed wavelengths. Here the sheet resistances of the absorption layers for both Salisbury Screens are 377Ω, and the distance to the mirror for 8.5μm and 12.5μm center wavelengths are 6.38μm and 9.38μm, respectively. These air gaps are made by deposition of sacrificial layers. From the perspective of fabrication, it is hard and time consuming to deposit this thick sacrificial layer. Consequently the multi-spectral system using the Salisbury Screens located in parallel is not suitable for the wavelength selectivities. In addition, parallel locating occupies a lot of spaces, lowering the compactness of the structure.

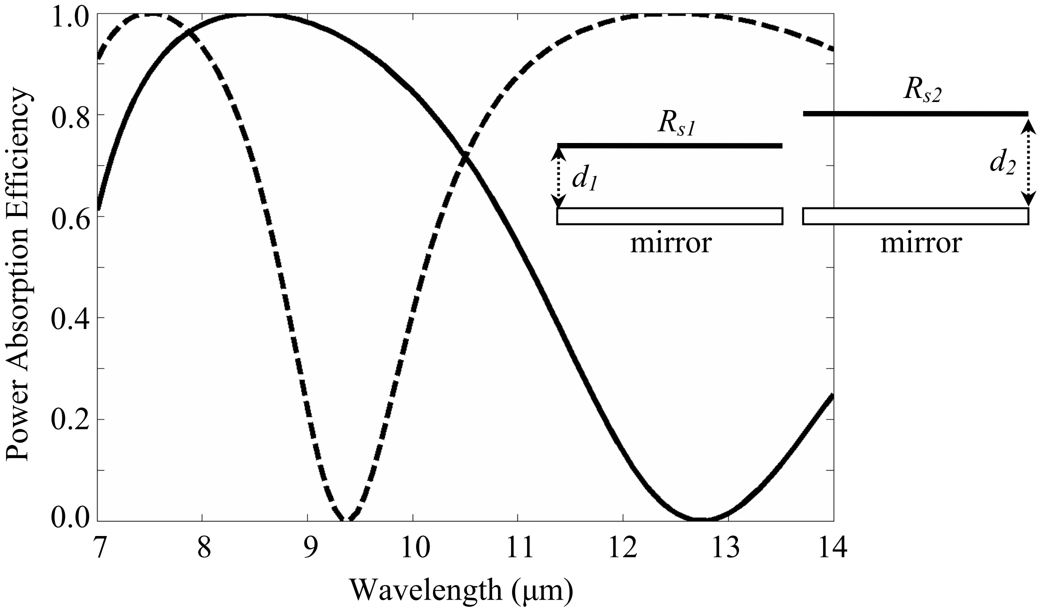

Figure 4.9: Design of two-spectral infrared detection using the conventional Salisbury Screens located in parallel. The solid line is designed to absorb a band centered at 8.5μm wavelength while the dashed line is designed to absorb a band centered at 12.5μm. It is not suitable for the wavelength selectivity because of the ambiguity of absorbed wavelengths over 7 to 9μm and 10 to 12μm. The sheet resistance of the absorption layer for both microbolometers is 377Ω, and the distance to the mirror for 8.5μm and 12.5μm center wavelengths are 6.38μm and 9.38μm, respectively.

Chapter 5: Broad Band Or Wavelength Selective Salisbury Screens And Jaumann Absorbers

Conventional infrared microbolometers are usually designed for use on only one infrared band. Here we consider various bolometer layer stacks and use a Genetic Algorithm (GA) to find designs that achieve maximized broad band spectral response over the entire mid and long wavelength bands (3~13µm). Multi-color narrow-band Salisbury Screen and Jaumann Absorbers using optimized thickness Germanium (Ge) layers are also designed that produce wavelength selectivity in 7~14µm wavelength band. The Jaumann Absorbers can be used as a vertically stacked pixel structure to save space and enhance resolution compared to frequency selective Salisbury Screen pixels lying in a common plane.

5.1 DIELECTRIC COATED SALISBURY SCREEN FOR BROAD BAND ABSORPTION

A simple Salisbury Screen microbolometer can actually produce fairly broad spectral absorption in 3~13µm infrared band. The thick solid line in Figure 5.1 shows the power absorption efficiency of a basic Salisbury Screen microbolometer GA-designed to maximize the integrated absorption over the entire mid and long infrared bands, using only two design parameters: the sheet resistance R_s of the absorbing sheet and the distance *d* to the mirror. Here the GA-optimization gives R_s =300Ω/□ and *d* = 1.35µm. In this case, the optimized R_s is not 377Ω/□ because we maximize the integrated absorption over 3~13µm instead of maximizing the power absorption at a single wavelength. The broad band absorption of the Salisbury Screen is accomplished by producing a quarter wave resonance in the shorter wavelength region, here at 5.4µm (four times the distance to the mirror), while the long wavelength tail still produces good absorption out to 13µm, producing an overall integrated absorption efficiency of 88%.

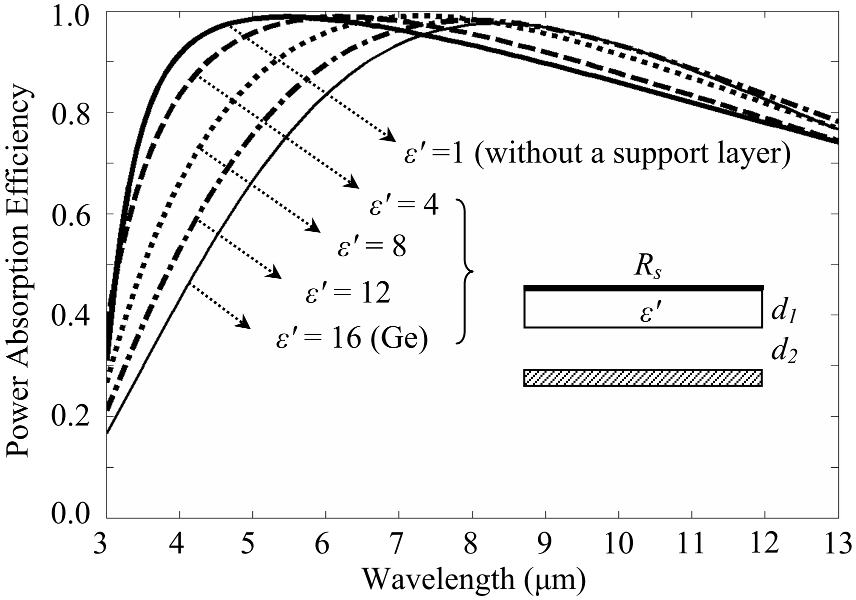

Figure 5.1: Effects of supporting material on broad band absorption of bolometric layer. Corresponding GA-optimized integrated efficiencies to ε' =1, 4, 8, 12, and 16 (Germanium) are 88%, 88%, 86%, 83%, and 80% (Germanuium), respectively. As ε' goes up, broad band absorption deteriorates. The thick solid curve is broad band absorption without a support layer providing 88% of integrated efficiency.

From the perspective of fabrication, a real resistive bolometer layer requires a dielectric support layer of finite thickness, which will affect the power absorption due to interference effects in the dielectric and vacuum gap (required for thermal isolation). To see these effects we assume free standing Germanium (Ge) layers to support the resistive absorbing layer. There are now three design parameters: the sheet resistance R_s of the absorbing sheet, the thickness d_1 of the Ge layer, and the vacuum gap between the bottom of the Ge and the mirror, d_2. The thin solid line in Figure 5.1 shows power absorption efficiency of a GA-optimized Salisbury Screen microbolometer including a Ge support layer below the absorbing sheet. The best broadband spectral response actually occurs when d_1 is zero, i.e. no support layer. Hence during optimization the GA always selects the smallest support layer thickness allowed; here we assume that a minimum thickness of 0.1μm is required to provide the necessary mechanical rigidity. Using this constraint, the GA-optimized R_s and d_2 are $275\Omega/\square$ and 0.9μm providing 80% absorption of the incoming radiation, less than the free-standing design. Similar behavior can be observed in the more generalized Salisbury Screen shown in Figure 5.2 (a) to allow the possibility of support layers both above and below the resistive sheet. In this case, the optimization process selects finite thickness Ge layers both above and below the resistive absorbing sheet. Without the constraint of minimum thickness of the support layer for mechanical rigidity, the optimal thicknesses of both above and below Ge layers, d_1 and d_2, converge to zero for broad band absorption in 3-13μm band while GA-optimized R_s and d_3 converge to $300\Omega/\square$ and 1.35μm, respectively.

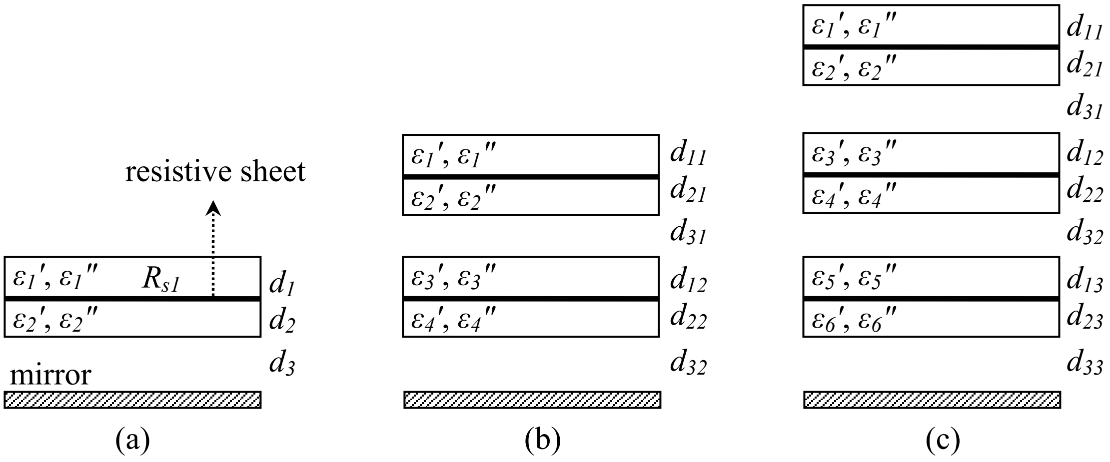

Figure 5.2: Configuration of broad band or wavelength selective pixels: (a) Dielectric-coated Salisbury Screen; (b) Two color dielectric-coated Jaumann Absorber; (c) Three color dielectric-coated Jaumann Absorber.

To see how the material for the support layer affects the broad band absorption, we set fictitious lossless material having frequency independent permittivity ε' of 1, 4, 8, 12, and 16 using configuration in Figure 5.1. Without the constraint of 0.1μm minimum thickness for the support layer, GA-optimized thickness of the support layer is zero regardless of the permittivity, i.e. regardless of the support material. Figure 5.1 shows broad band absorption with above fictitious support materials under the constraint. In Figure 5.1, corresponding GA-optimized integrated efficiencies to $\varepsilon'=1$, 4, 8, 12, and 16 are 88%, 88%, 86%, 83%, and 80%, respectively. Therefore, as the permittivity ε' goes up, broad band absorption deteriorates especially at low LWIR region. Consequently, support material with low permittivity would be better for the broad band absorption. As a reference, the thick solid curve in Figure 5.1 is broad band absorption without a support layer providing 88% of integrated efficiency. Specific designs yielding responses in Figure 5.1 are given in Table 5.1.

ε'	R_s (Ω)	d_1 (μm)	d_2 (μm)	Integrated Efficiency (%)
1	300	0.0	1.35	88
4	303	0.1	1.17	88
8	308	0.1	1.11	86
12	286	0.1	1.02	83
16	275	0.1	0.90	80

Table 5.1: Specific designs yielding responses given Figure 5.1. d_1 and d_2 are thicknesses of the support layer and an air gap.

In real materials, another possibility for support layers could be Si_3N_4 [42]. Si_3N_4 ($\varepsilon' \approx 7.5$) might be a better material than Ge ($\varepsilon' \approx 16$ [43]) for the support layer from the above observation that support materials with low ε' would be better for broad band absorption. The solid line in Figure 5.3 shows the GA-optimized broad band absorption by both bolometer and Si_3N_4 layers; 88% of integrated efficiency. The dashed and dotted lines in Figure 5.3 are power absorption efficiencies of bolometer and Si_3N_4 layers, respectively. In the low LWIR region, lossy Si_3N_4 acts like lossless, but it has high absorption in the high LWIR region. This is due to Si-N stretching vibrations generating strong power absorption at 10.4μm and 11.9μm wavelengths in LWIR [42]. Compared to 80% of integrated efficiency with Ge support layer shown in Figure 5.1, lossy Si_3N_4 with

88% of integrated efficiency is better than Ge as a support layer for broad band absorption. R_s, d_1, and d_2 of the design in Figure 5.3 are 320Ω/□, 0.1μm, and 1.2μm, respectively. Thickness of support layer d_1 is optimized under the constraint of 0.1μm minimum thickness.

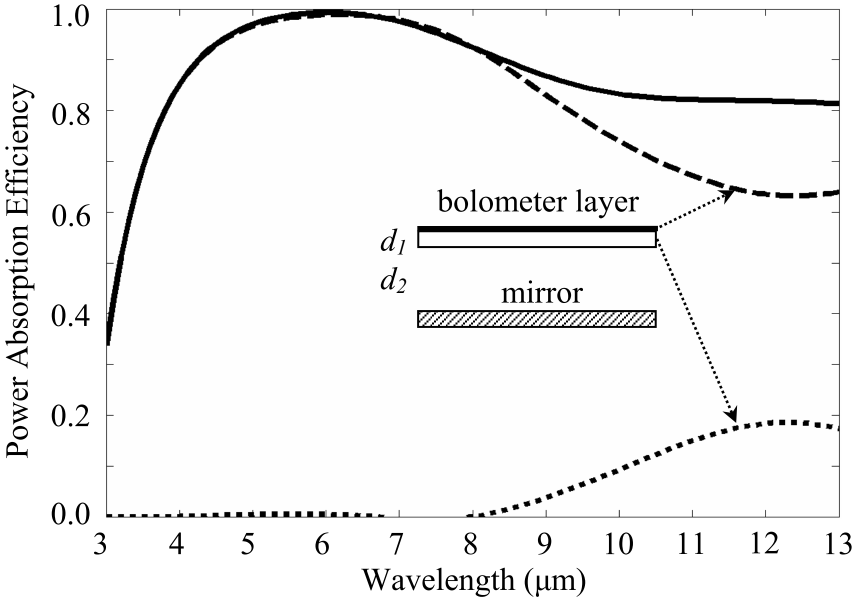

Figure 5.3: GA-optimized Salisbury Screens supported by lossy Si_3N_4 layer. Absorption by Si_3N_4 (dotted line) due to Si-N stretching vibrations deteriorates the absorption by the bolometric layer (dashed line) especially in a long wavelength region in a given range. The solid line is the sum of power absorption by both the bolometric layer and Si_3N_4 support layer. R_s, d_1, and d_2 are 320Ω/□, 0.1μm, and 1.2μm, respectively. Integrated efficiency = 88%. Solid: absorbed by the bolometric layer. Dotted: absorbed by the lossy Si_3N_4 support layer.

5.2 DIELECTRIC COATED JAUMANN ABSORBERS FOR BROAD BAND ABSORPTION

To achieve better broad band absorption bolometer layers could be stacked vertically to form a Jaumann Absorber. Again, supportive layers (Germanium) are also taken into account since they would be required in any real structure. One possibility would be to thermally isolate the bolometer layers by introducing another vacuum gap. To consider every possible support structure the configuration shown in Figure 5.2 (b) was studied. Each absorbing sheet can be supported by layers located above, below, or above and below the absorbing resistive sheet. There are now eight design parameters. The solid line in Figure 5.4 is the GA-optimized power absorption efficiency (found from the sum of each layer's absorption) for such a structure, again with the goal of achieving the highest absorption over the entire mid and long IR bands. The optimized design was R_{s1}, R_{s2}, d_1, d_2, d_3, d_4, d_5, and d_6 (refer to Figure 5.2 (b)) equal to 490Ω/□, 200Ω/□, 0.024μm, 0.007μm, 1.16μm, 0.14μm, 0.11μm, and 0.24μm, respectively. The overall response is slightly better than the previous designs: 93% absorption of the incoming radiation in 3~13μm band.

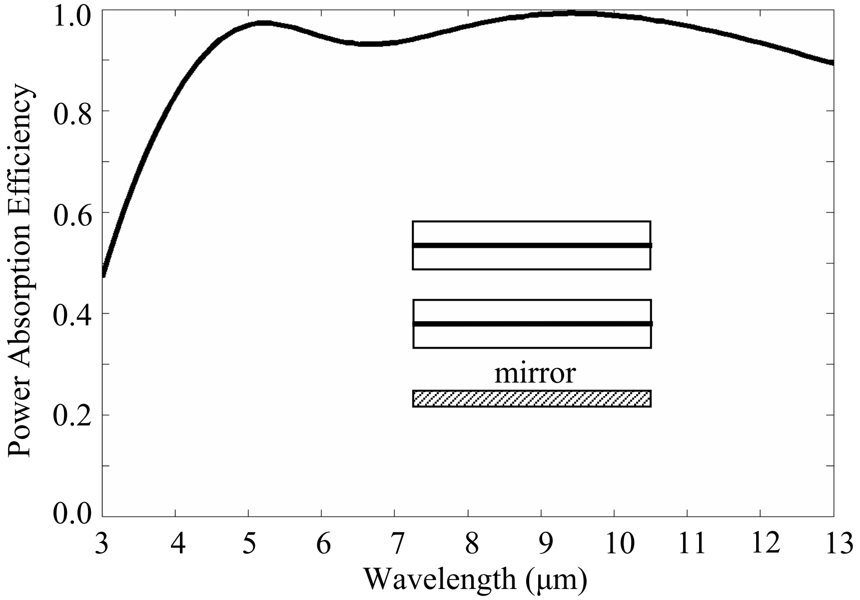

Figure 5.4: Optimized power absorption efficiencies of dielectric-coated Jaumann Absorbers producing integrated absorption of 93% over the 3~13μm band.

5.3 DIELECTRIC COATED SALISBURY SCREENS

It is hard to construct narrow band absorption by Salisbury Screen consisting of only a resistive sheet and a mirror in 7~14μm wavelength band. So we add dielectric coating in the configuration in Figure 5.2 to give more design freedom and produce wavelength selectivity. Now the generalized Salisbury Screen for each pixel consists of a resistive layer coated on both sides by transparent dielectric layers, all placed in front of a mirror (Figure 5.5 (a)).

Our wavelength selective design using the generalized Salisbury Screens is to produce three separate pixels, each with a different peak absorption wavelength in order to allow the construction of a three color "tiled" focal plane array (i.e., three separate color pixels lying in a common plane, Figure 5.5). The three pixels should have peak absorption at 8, 10, and 12μm wavelengths. For convenience, here we assume the dielectric to be Germanium (Ge), and use the infrared optical constants for that material. Ge is almost lossless in long wave infrared (LWIR) range because its extinction coefficient *k* is almost zero in that range [44]. To find the proper thickness of the Ge support layers, we use a Genetic Algorithm (GA) as an optimization scheme. To locate narrow bandwidth array designs that couple strongly at a desired wavelength, we have used a cost definition for the GA that seeks high power absorption at a specified wavelength while minimizing the power absorbed at other wavelengths. This is accomplished by minimizing the area under the absorption curve, as given by:

$$\begin{cases} \text{if } \mathrm{PAE}\big|_{\text{desired }\lambda} > threshold, & cost = \int_{7\mu m}^{14\mu m} \mathrm{PAE}(\lambda)\, d\lambda \\ \qquad \text{otherwise,} & cost = \infty \end{cases} \qquad \text{Eq. 5.1}$$

where PAE stands for power absorption efficiency. Figure 5.6 shows GA-optimized spectral responses.

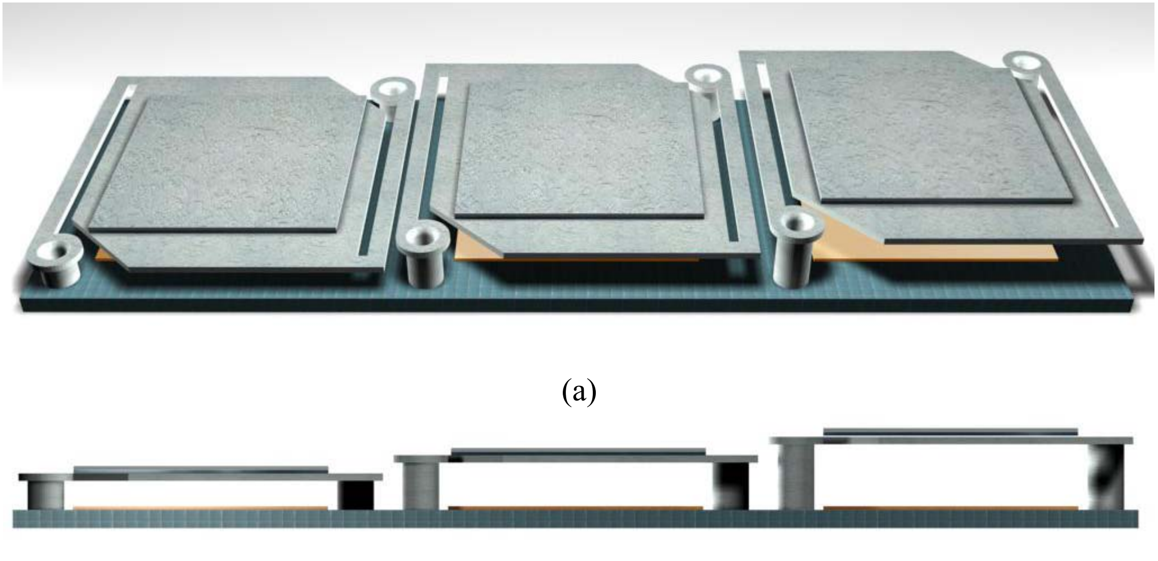

Figure 5.5: Salisbury Screens located in parallel for 2-color infrared detection. (a) Perspective view. (b) Front View.

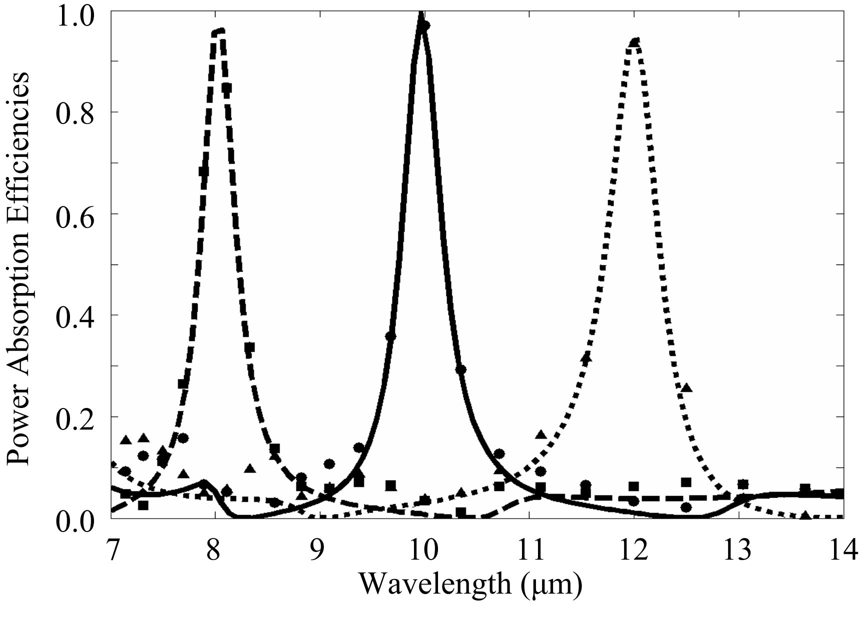

Figure 5.6: GA-optimized designs to absorb 3 colors centered at 8, 10, and 12µm wavelengths. Dashed, solid, and dotted curves are from calculation using the ABCD transmission line matrix method. Polygons are from Ansoft HFSS.

The optimized designs in Figure 5.6 have also been verified using Ansoft HFSS [24], a 3D full-wave finite element method (FEM) solver (HFSS results indicated using the points in Figure 5.6); agreement in all cases is excellent. Specific designs yielding responses in Figure 5.6 are given in Table 5.2. The results clearly show that three microbolometers with different dielectric coatings could be constructed to yield non-overlapping three color wavelength selective devices.

λ_{center}	8µm (dashed)	10µm (solid)	12µm (dotted)
R_{s1} (Ω)	444	459	535
d_1 (µm)	2.1	2.5	1.6
d_2 (µm)	0.5	0.6	0.6
d_3 (µm)	3.9	5.0	6.0

Table 5.2: Specific designs yielding responses given Figure 5.6. d_1 and d_2 are thickness of Ge support layers, and d_3 is thickness of an air gap (refer to Figure 5.2 (a)).

5.4 TUNING OF SALISBURY SCREENS BY VARYING AIR GAP

Tuning of the Salisbury Screen has been achieved several ways [45]. One of them is tuning by varying air gap thickness. From the perspective of simple fabrication processes, it might be appropriate to make thicknesses of Ge support layers identical for all three designs prepared to absorb 8, 10, and 12µm wavelengths as shown in Figure 5.8 (a) so that tuning of absorption wavelength is achieved by varying only the air gap between a bolometric layer and a mirror. First of all, we vary the air gap thickness, d_3, of the design (solid curve) shown in Figure 5.6. With fixed parameter values except air gap d_3, we shift the absorption peak along wavelength by varying air gap d_3 until the absorption peak reaches from 10µm to 8 or 12µm. Figure 5.7 is the tuned results of the solid curve in Figure 5.6 by varying d_3. The dotted line is tuned to absorb 8µm wavelength by varying d_3 from 5.0µm to 2.0µm. But its peak absorption gets low fast as it moves to the left, and tuning also results in a high ghost peak around 12μm. The dashed line is tuned to absorb 12μm wavelength by varying air gap thickness d_3 from 5.0μm to 7.6μm. But its peak absorption gets low as it moves to the right, and tuning also results in a high ghost peak around 7.5μm and 8.5μm. As figure of merits for wavelength selectivity, we compare peak absorption, in-band integrated efficiency, and selectivity of the designs shown in Figure 5.7 in Table 5.3. 'In-band integrated efficiency' is integrated efficiency in the target wavelength ± 1μm band, and 'selectivity' is 'in-band integrated efficiency' to 'out-of-band integrated efficiency' ratio; the higher, the better. In Table 5.3, the design with 5.0μm shows good wavelength selectivity, while the designs with 2.0μm and 7.6μm air gaps show poor ones. Consequently, from the perspective of 3-color wavelength selectivity, the designs in Figure 5.7 are very poor.

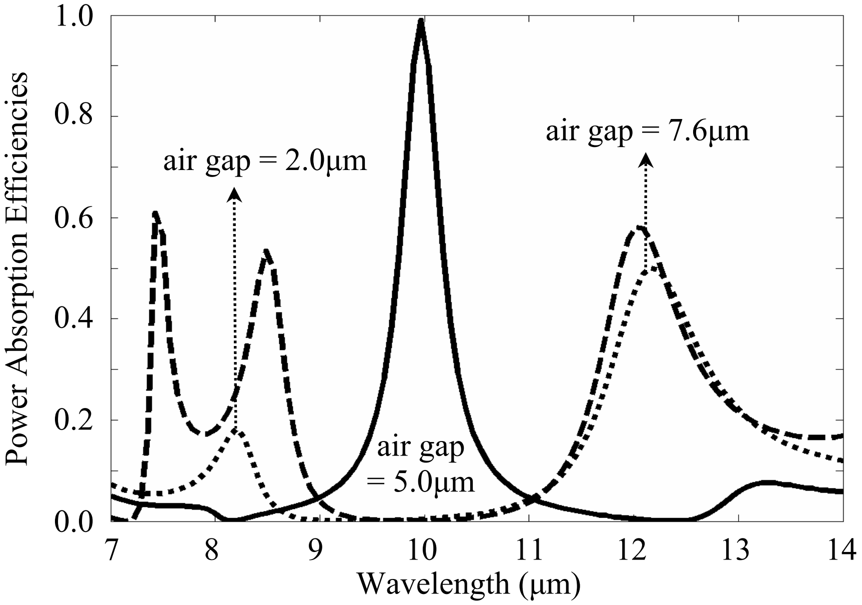

Figure 5.7: Tuning of the design illustrated in Figure 5.6 (solid line) by varying air gap thickness. From the perspective of multi-color wavelength selectivity, these are very poor designs. The dotted line is tuned to absorb 8μm wavelength by varying d_3 from 5.0μm to 2.0μm. The dashed line is tuned to absorb 12μm wavelength by varying air gap thickness d_3 from 5.0μm to 7.6μm. Here d_1=2.5μm, R_{s1}=459Ω/□, d_2=0.6μm, d_{31}=2.0μm, d_{32}=5.0μm, and d_{33}=7.6μm (refer to Figure 5.8 (a) for the notations).

Air gap	Peak power absorption	In-band integrated efficiency	Selectivity
2.0μm	18.2%	7%	0.2
5.0μm	99.0%	30%	6.0
7.6μm	58.1%	32%	1.3

Table 5.3: Figure of merits for wavelength selectivity of spectral responses shown in Figure 5.7. ‘In-band integrated efficiency’ is integrated efficiency in target wavelength ± 1μm band, and ‘Selectivity’ is ‘in-band integrated efficiency’ to ‘out-of-band integrated efficiency’ ratio. Based on the ‘Selectivity’, designs with 2.0μm and 7.6μm air gap have poor wavelength selectivity.

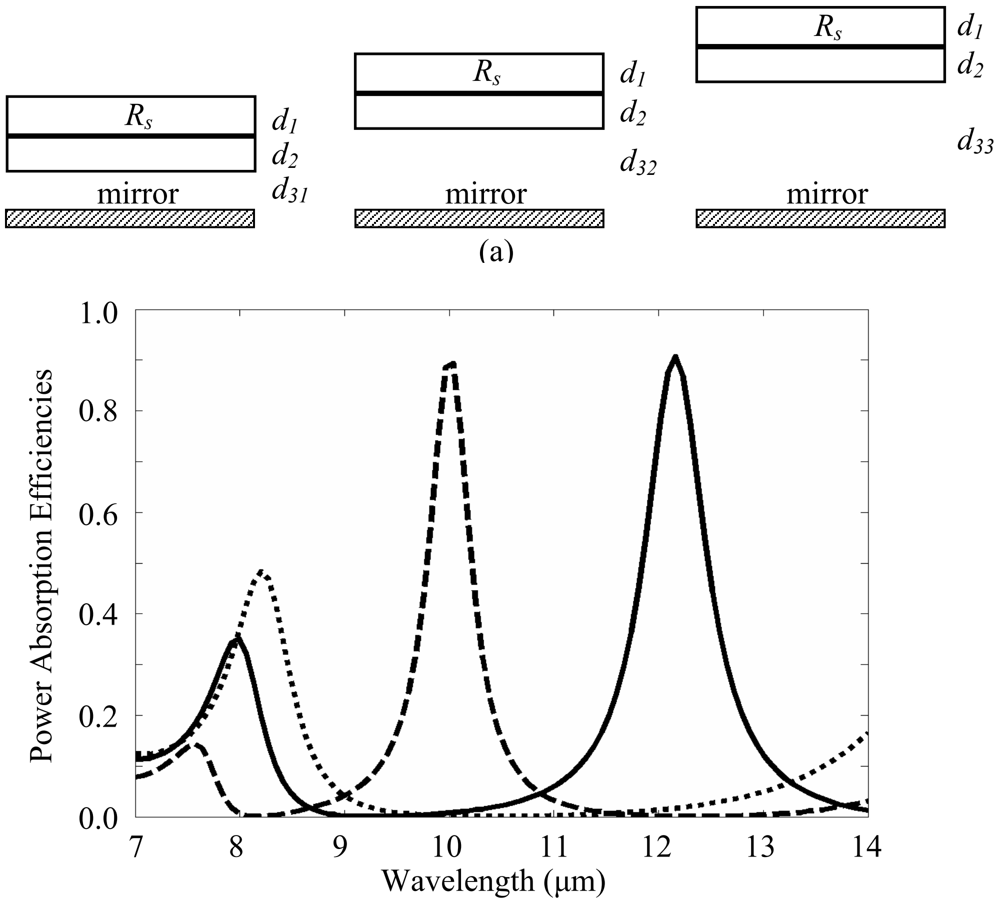

(a)

(b)

Figure 5.8: Tunable Salisbury Screen. To achieve tuning of absorption wavelength, thicknesses of Ge support layers are fixed for all three designs prepared to absorb 8, 10, and 12μm wavelengths. (a) Configuration. (b) Spectral responses of optimized designs. Dashed, solid, and dotted curves are calculated from ABCD matrix analysis. Polygons are calculated from Ansoft HFSS and provided as verification of ABCD matrix analysis.

Secondly, we try to optimize the Salisbury Screen to achieve tuning by varying the air gap. This leads to a six parameter design search, R_s, d_1, d_2, d_{31}, d_{32}, and d_{33} (refer to Figure 5.8 (a)). As a cost definition for optimization, we set up ideal power absorption efficiencies for 3-color wavelength selectivity, and then try to minimize the difference between ideal and real curves. Ideal power absorption efficiency curves are normalized Gaussian distribution curves with average=8, 10, and 12 and standard deviation σ=0.5. Figure 5.8 (b) shows optimized results. Spectral response curves in Figure 5.8 (b) show good wavelength selectivity of 10 and 12μm wavelengths. However, wavelength selectivity of 8μm wavelength is a little ambiguous due to ghost absorption peak by another pixel. Figure of merits for the designs shown in Figure 5.8 (b) are listed in Table 5.4. 'Selectivity' in Table 5.4 is higher than that in Table 5.3 (Figure 5.7). So we can say that the designs in Figure 5.8 (b) are better than those in Figure 5.7 from the perspective of wavelength selectivity. Specific designs yielding responses in Figure 5.8 (b) are given in Table 5.5.

Air gap	Peak power absorption	In-band integrated efficiency	Selectivity
2.0μm	40.1%	20%	7.8
5.0μm	89.5%	28%	6.2
7.6μm	91.3%	39%	2.9

Table 5.4: Figure of merits for wavelength selectivity of spectral responses shown in Figure 5.8 (b). 'In-band integrated efficiency' is integrated efficiency in target wavelength ± 1μm band, and 'Selectivity' is 'in-band integrated efficiency' to 'out-of-band integrated efficiency' ratio. From the comparison of 'Selectivity' in Table 5.3 (Figure 5.7) and that in Table 5.4 (Figure 5.8 (b)), the designs in Figure 5.8 (b) show much better wavelength selectivity.

λ_{center}	8µm (dashed, *j*=1)	10µm (solid, *j*=2)	12µm (dotted, *j*=3)
d_1 (µm)	1.4		
R_s (Ω/□)	644		
d_2 (µm)	0.6		
d_{3j} (µm)	3.1	4.9	6.4

Table 5.5: Specific designs yielding responses given Figure 5.8 (b). d_1 and d_2 are thickness of Ge support layers, and d_3 is thickness of an air gap (refer to Figure 5.8 (a)).

5.5 WAVELENGTH SELECTIVE 2-COLOR JAUMANN ABSORBERS

Using dielectric coated Jaumann Absorbers here we design a true 2-color stacked microbolometer that would produce a separate signal for each band (centered at 8.5µm and 12.5µm wavelengths) (Figure 5.9). "Stacking" (pixels locating vertically) can save space and enhance resolution of images compared to the "tiling" described in section 5.3. A vacuum-gap between the two absorbing layers would thermally isolate them, hence producing separate signals for each color. Our design goal is for each of the separated absorbing layers in the stacked pixel to maintain strong absorption at a specified center wavelength while minimizing the absorption at other wavelengths; this leads to an eight parameter design search, R_{s1}, d_1, d_2, d_3, R_{s2}, d_4, d_5, and d_6. As a cost definition, we set up ideal power absorption efficiencies for 2-color wavelength selectivity, and then try to minimize the difference between ideal and real curves. Figure 5.10 illustrates GA-optimized designs showing the best 2-color wavelength selectivity we could achieve using this structure. Again the design in Figure 5.10 is verified with Ansoft HFSS in Figure 5.11, which shows the sum of power absorption by both top and bottom pixels. Specific designs yielding responses in Figure 5.10 are given in Table 5.6.

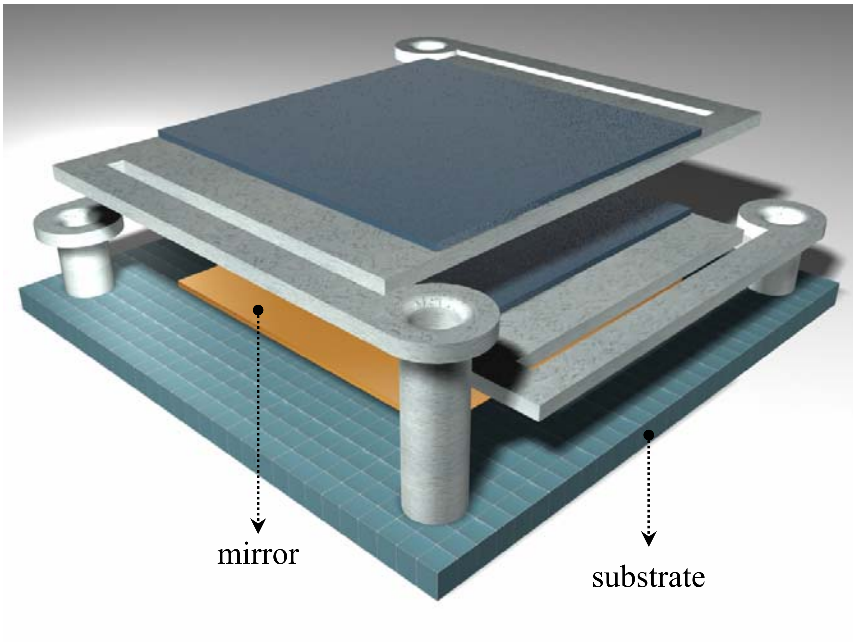

Figure 5.9: Jaumann Absorber for 2-color wavelength selectivity. Each layer absorbs its own designated wavelength band.

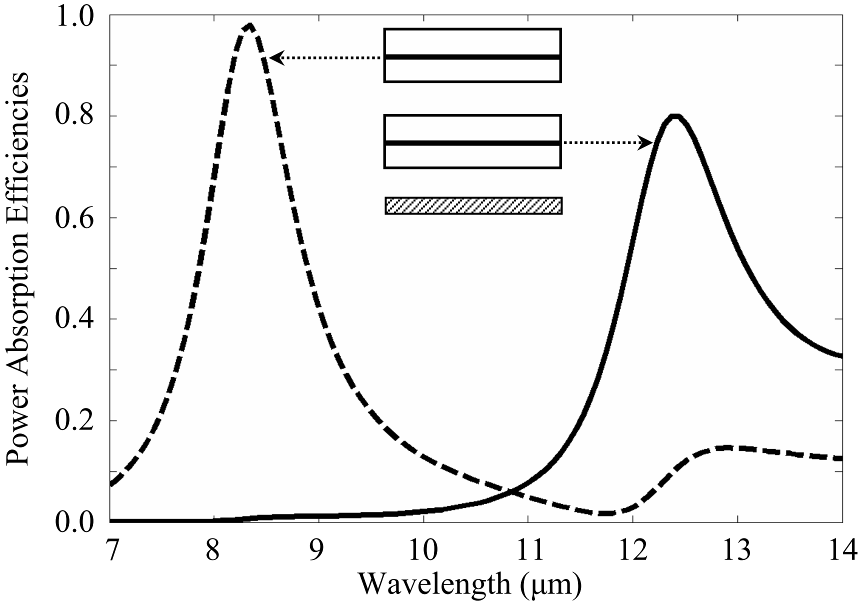

Figure 5.10: GA-optimized vertically stacked pixels to absorb 2 colors centered at 8.5 and 12.5μm wavelengths. Solid: absorbed by top absorbing layer. Dashed: absorbed by bottom absorbing layer.

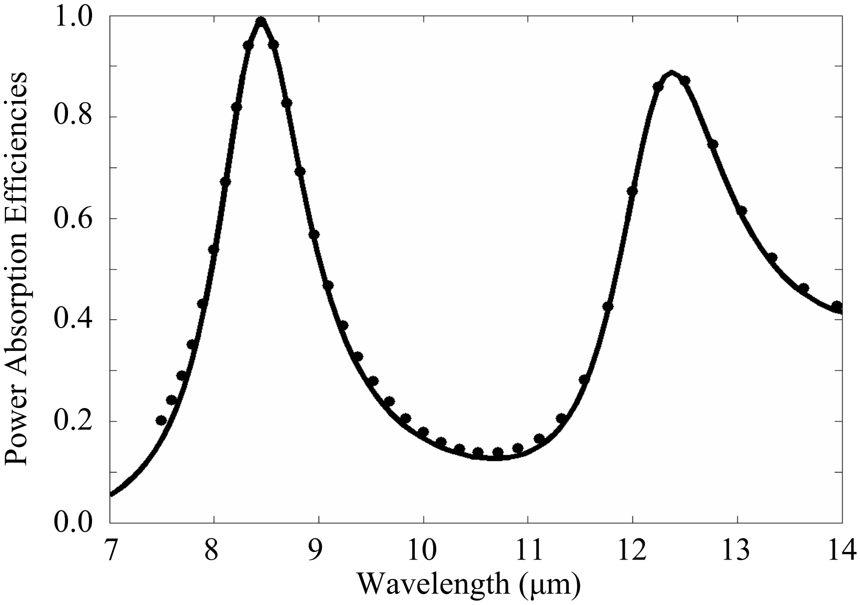

Figure 5.11: Sum of power absorption by the design described in Figure 5.10. Solid curve is calculated using the ABCD matrix analysis, and circles are from Ansoft HFSS calculations.

	Stack 1 (*j*=1)	Stack 2 (*j*=2)
d_{1j} (µm)	1.0	0.0
R_{sj} (Ω)	468	724
d_{2j} (µm)	1.2	0.7
d_{3j} (µm)	1.1	0.3

Table 5.6: Specific designs yielding responses given Figure 5.10. (refer to Figure 5.2 (b) for notation).

The Jaumann Absorber can also be applied to 2-color infrared detection in different wavelength bands such as 3~5µm, mid infrared band. Figure 5.12 shows a 2-color design found by optimizing Jaumann Absorbers in 3~5µm wavelengths. R_{s1}, R_{s2}, d_1, d_2, d_3, and d_4 are 939.5 Ω, 415.9 Ω, 2.48µm, 0.89 m, 0.89µm, and 0.81µm respectively where the dielectric constant for the dielectric coating is 7.5.

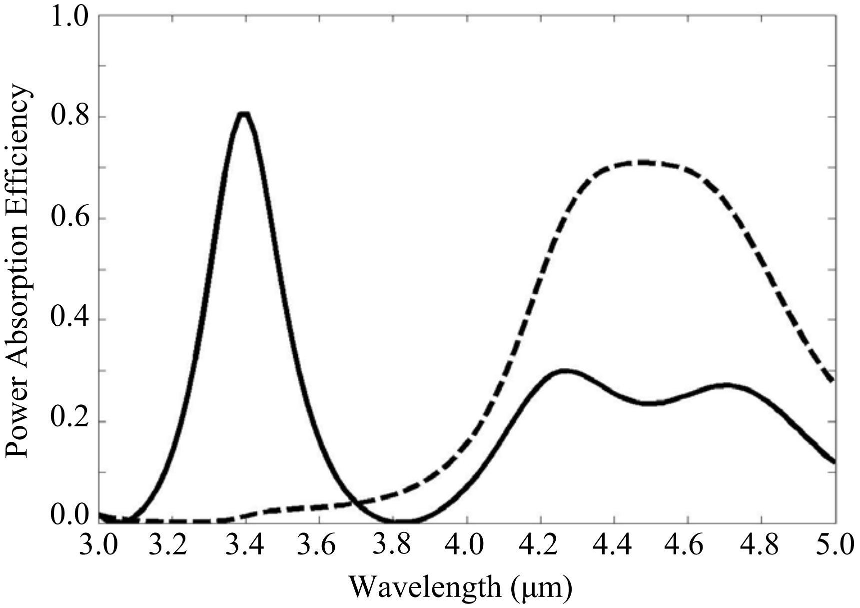

Figure 5.12: 2-color design found by optimizing Jaumann Absorbers in 3~5μm wavelengths, mid IR band.

Similarly, the Jaumann Absorber can be used for 2-color infrared detection in 3~13μm covering both mid and long infrared bands. Figure 5.13 shows 2-color design found by optimizing Jaumann Absorbers in 3~13μm wavelengths covering both mid and long IR bands. One color is for mid IR band, 3~5μm, and the other is for long IR band, 8-12μm. The solid and dashed lines are power absorption efficiencies absorbed by the top and bottom absorbing sheets, respectively. GA-optimized R_{s1}, R_{s2}, d_1, d_2, d_3, and d_4 are 700Ω, 150Ω, 0.9μm, 0.1μm, 0.6μm, and 0.1μm respectively where the dielectric constant for the dielectric coating is 7.5.

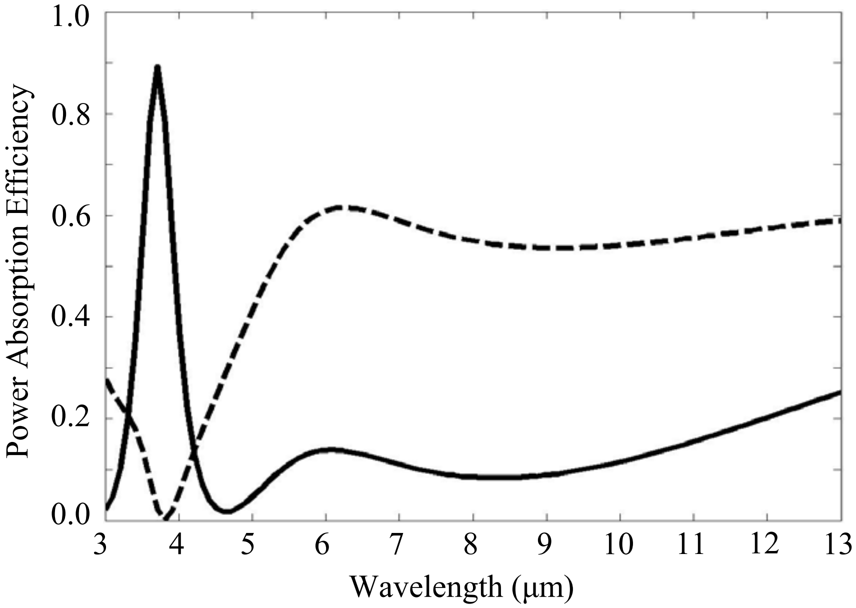

Figure 5.13: 2-color design found by optimizing Jaumann Absorbers in 3~13µm wavelengths, mid and long IR bands. One color is for mid IR band, 3~5µm, and the other is for long IR band, 8-12µm.

5.6 WAVELENGTH SELECTIVE 3-COLOR JAUMANN ABSORBERS

We finally design 3-color stacked pixels (centered at 8µm, 10µm and 12µm) using generalized dielectric coated Jaumann Absorbers (Figure 5.2 (c)). Again the design goal is for each absorbing layer in the stacked pixel to maintain strong absorption at a specified center wavelength while minimizing the absorption at other wavelengths; this leads to a twelve parameter design search, R_{s1}, d_1, d_2, d_3, R_{s2}, d_4, d_5, d_6, R_{s3}, d_7, d_8, and d_9, as illustrated in Figure 5.2 (c). Figure 5.14 shows a GA-optimized design producing 3-color wavelength selectivity. The optimized design in Figure 5.14 is verified with Ansoft HFSS where Figure 5.15 shows the sum of power absorption by all the layers in the pixel. By comparing Figures 5.6, 5.10, and 5.14, it is clear that as the number of layers in the stack goes up, the wavelength selectivity gets worse. Therefore, placing more than 4 separate absorbing layers in a stack actually reduces wavelength selectivity and does not produce useful four color wavelength selectivity. This has been verified by attempting such a GA-optimized design: the results are clearly inferior to the three color design in terms of overlap in absorption between the layers. Specific designs yielding responses in Figure 5.14 are given in Table 5.7.

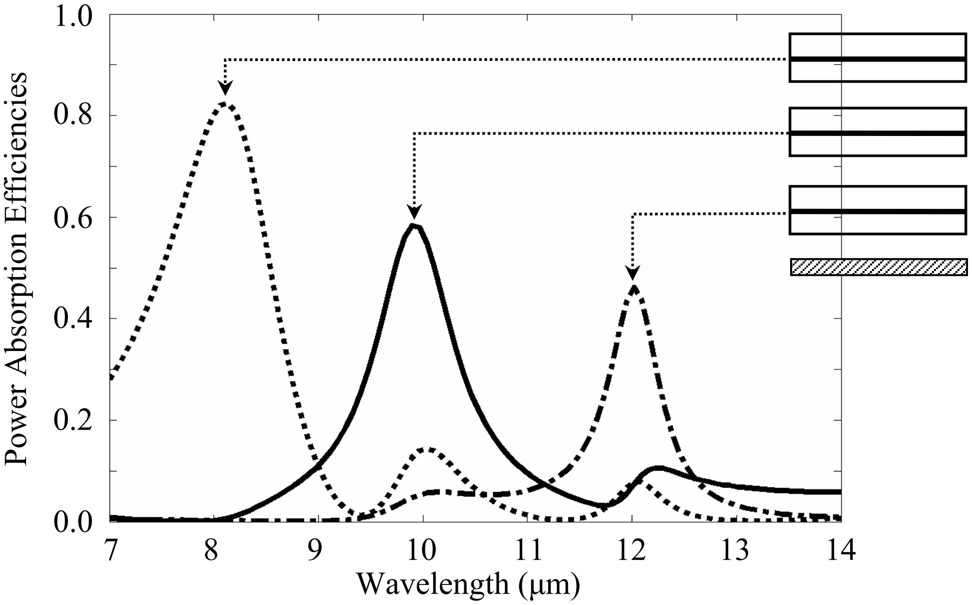

Figure 5.14: GA-optimized vertically stacked pixels to absorb 3 colors centered at 8, 10, and 12μm wavelengths. Dotted: absorbed by top pixel. Solid: absorbed by middle pixel. Dash-dotted: absorbed by bottom pixel.

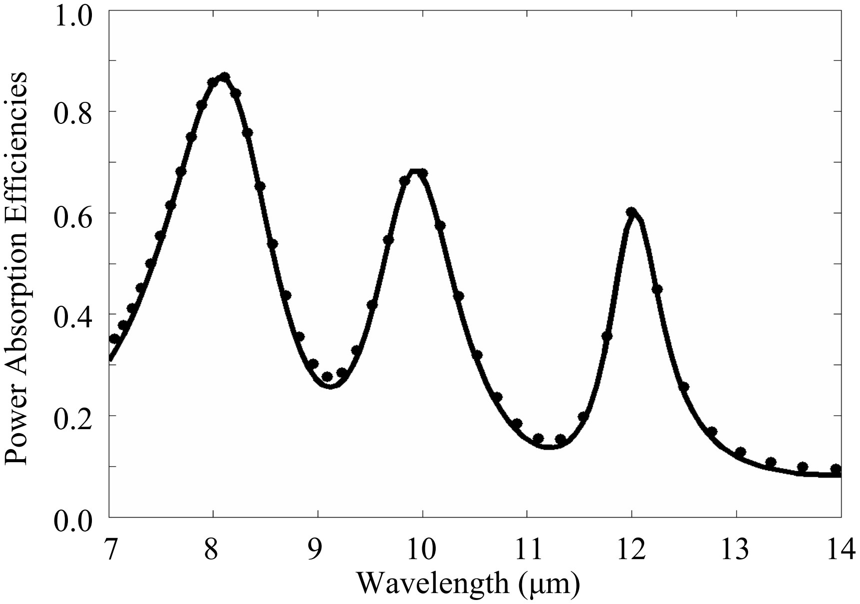

Figure 5.15: Sum of power absorption by the design described in Figure 5.14. Solid curve is calculated using ABCD matrix analysis, and circles are simulated from Ansoft HFSS for verification.

	Stack 1 (*j*=1)	Stack 2 (*j*=2)	Stack 3 (*j*=3)
d_{1j} (μm)	0.2	1.0	0.0
R_{sj} (Ω)	568	221	930
d_{2j} (μm)	0.9	0.5	1.7
d_{3j} (μm)	1.1	0.9	1.2

Table 5.7: Specific designs yielding responses given Figure 5.14. (refer to Figure 5.2 (c) for notation).

Chapter 6: Modified Planar Multimode Detectors for High Sensitivity

In this chapter, we modify the original planar multimode detectors for the high sensitivity and better thermal behaviors as shown Figure 6.1~6.3. The original planar multimode detectors have an interwoven grid of metallic and resistive layers located on the support layers such as Si_3N_4 (Figure 2.6). In the original planar multimode detectors, the thermal contact between the absorbing resistive layers and the support layers incurs the thermal loss. The thermal isolation of the absorbing resistive layers from the support layers can prevent this thermal loss.

In the modified planar multimode detectors, we air-bridge only absorbing resistive layers instead of the whole interwoven grid with its support layer to prevent the thermal loss described above (Figure 6.1~6.3). Here the metal strips act as antennas, and then focus the absorbed power into small regions. This generates non-uniform thermal distribution along the absorbing resistive bars. Depending on the shape of the absorbing resistive bars, there are different numbers of thermal sources, thermally focused regions, along the bar. N is defined as the number of thermal sources on each bar. In Figure 6.1, the incident power is uniformly distributed along each bar so that N equals to 1. On the other hand, each absorbing resistive bar in Figure 6.2 and 6.3 has three and nine thermally focused regions so that N equals to three and nine, respectively. These different configurations result in different sensitivities, and they will be analyzed throughout Chapter 6.

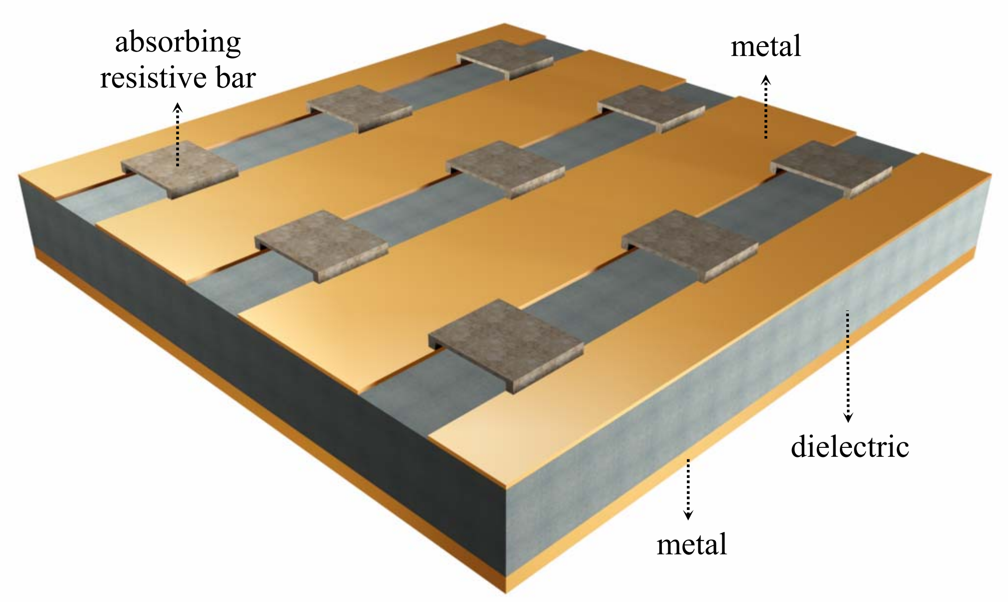

Figure 6.1: Air-bridge microbolometer when N=1, where N is the number of thermal sources along each absorbing resistive bar.

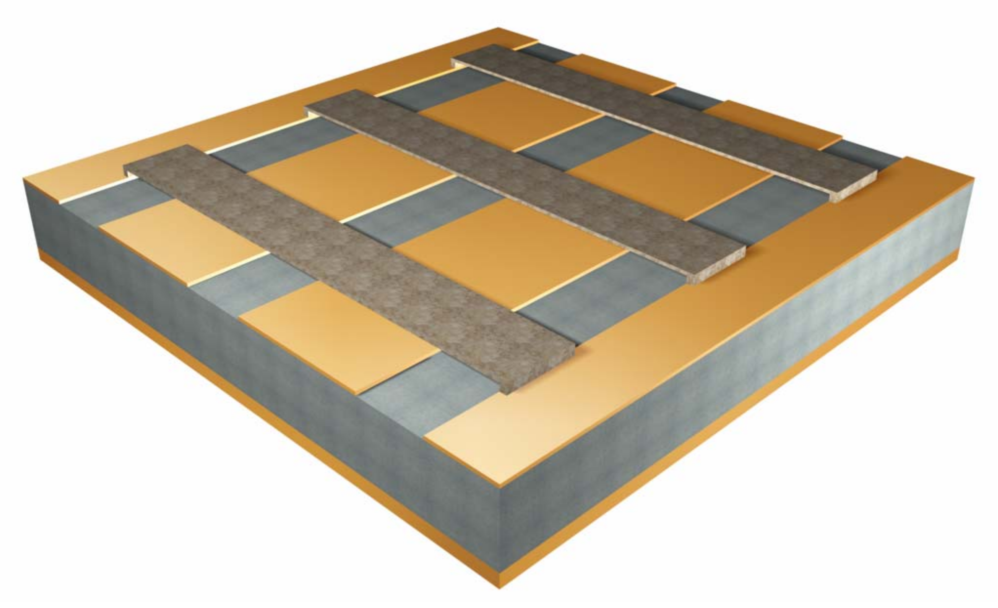

Figure 6.2: Air-bridge microbolometer when N=3.

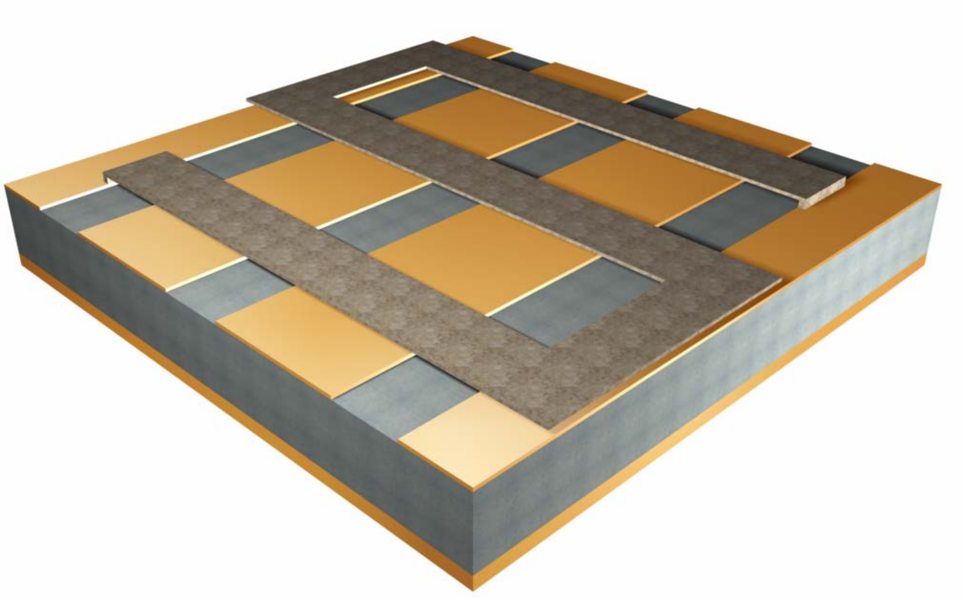

Figure 6.3: Air-bridge microbolometer when N=9.

6.1 SIMPLE THERMAL MODELS

A microbolometer's performance can be improved by increasing its thermal impedance. The air-bridge bolometer does this by suspending the device in the air above the substrate as in Figure 2.1. The only conduction path is now out the ends of the detector into heat sinks. We can model this bolometer in a particularly simple manner: a uniform bar of material in which power is dissipated uniformly, and whose ends are attached to perfect heat sinks (Figure 6.4).

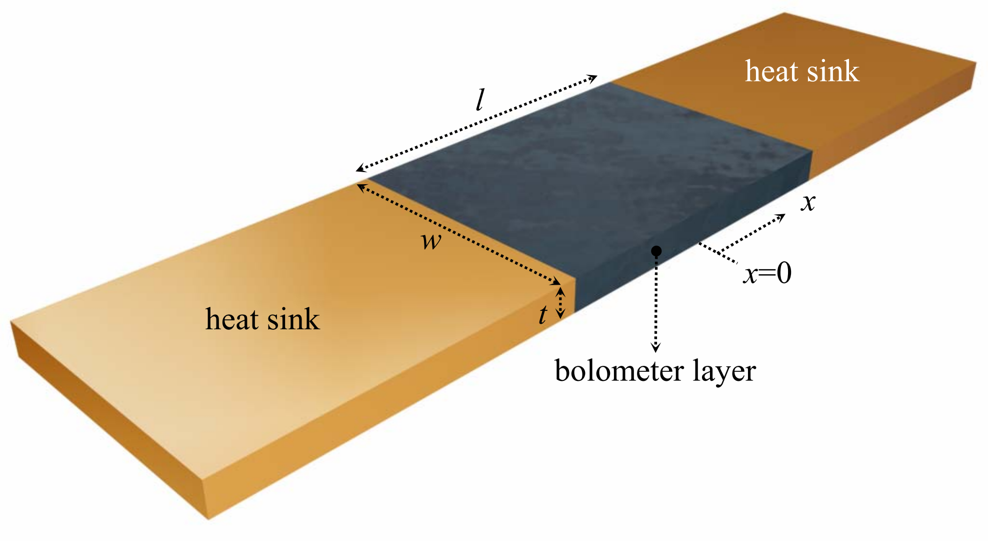

Figure 6.4: Simple thermal model of the air-bridge bolometer with only conduction path to the heat sinks.

The thermal diffusion equation describing the temperature rise ϕ in the device shown in Figure 6.4 is

$$\frac{\partial^2 \phi}{\partial x^2} = \frac{\rho_{bolo} C_{bolo}}{\kappa_{bolo}} \frac{\partial \phi}{\partial t} - \frac{P_{incident}}{l \cdot t \cdot w \cdot \kappa_{bolo}} \quad \text{Eq. 6.1}$$

$$P_{incident=} \frac{P_0}{2}\left(1 + e^{j\omega t}\right) \quad \text{Eq. 6.2}$$

where ρ_{bolo}, κ_{bolo}, and C_{bolo} are density, thermal conductivity, and specific heat of the bolometer material, and P_0 is the peak power dissipated in the bolometer. This equation is solved subject to the boundary condition that ϕ is zero at the ends of the detector. The solution is

$$\phi(x,t) = \frac{P_0}{2 \cdot l \cdot t \cdot w \cdot \kappa_{bolo}} \left[\frac{l^2}{8} - \frac{x^2}{2} + j \frac{\kappa_{bolo}}{\rho_{bolo} \cdot C_{bolo} \cdot \omega} \cdot e^{j\omega t} \cdot \left\{ \frac{\cosh(\gamma x)}{\cosh(\gamma \cdot l / 2)} - 1 \right\} \right] \quad \text{Eq. 6.3}$$

where

$$\gamma \equiv \sqrt{\frac{j\omega \rho_{bolo} C_{bolo}}{\kappa_{bolo}}}. \quad \text{Eq. 6.4}$$

For example, when the bolometer layer is Bismuth (Bi) and l is 2.4μm, w=1.0μm, and t=0.1μm, the temperature rise profile is shown in Figure 6.5. Here, ρ_{Bi}=9.86×10^{6}g·m^{-3}, C_{Bi}=0.12J·g^{-1}·K^{-1}, κ_{Bi}=13.5W·m^{-1}·K^{-1}, σ=867,100S·m^{-1}, λ=10μm, and P_0=0.39×10^{-6}W.

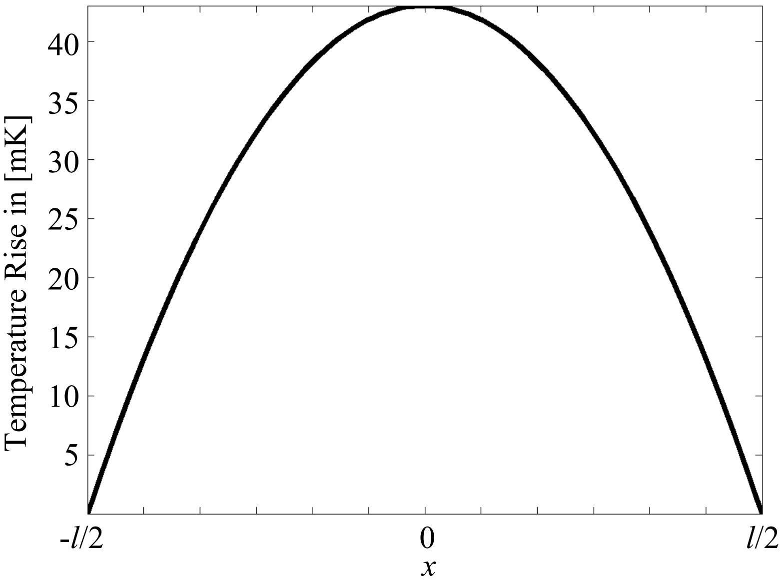

Figure 6.5: Temperature rise $\phi(x)$ along a bar. The bolometer material is Bismuth and l is 2.4μm, w=1.0μm, and t=0.1μm.

The solution is integrated over x to obtain the average temperature rise $\langle\phi\rangle$ in the device.

$$\langle\phi(x)\rangle = \frac{1}{l}\int_{-l/2}^{l/2}\phi(x)dx = \frac{P_0}{24\cdot t\cdot w\cdot\kappa_{bolo}}\left[1+24\cdot\frac{1}{(\gamma\cdot l)^3}\cdot e^{j\omega t}\cdot\left\{\frac{\gamma\cdot l}{2}-\tanh\left(\frac{\gamma\cdot l}{2}\right)\right\}\right] \qquad \text{Eq. 6.5}$$

In the above example using Bismuth as the bolometer material, the average temperature rise corresponding to input IR power P_0=0.39×10^{-6}W is about 28.7mK.

The ratio of time varying temperature to time varying input power yields the thermal impedance of the air-bridge bolometer.

$$Z_{thermal}(\omega) = 2\frac{l}{t\cdot w\cdot\kappa_{bolo}}\cdot\frac{1}{(\gamma\cdot l)^3}\cdot\left\{\frac{\gamma\cdot l}{2}-\tanh\left(\frac{\gamma\cdot l}{2}\right)\right\} \qquad \text{Eq. 6.6}$$

At low frequency, a length of bar is much less than thermal diffusion length, $L_{thermal}$.

$$|\gamma| \cdot l = \frac{l}{L_{thermal}} = \left| \sqrt{\frac{j \cdot \omega \cdot \rho \cdot C}{\kappa}} \right| \cdot l << 1 \qquad \text{Eq. 6.7}$$

$$\left\langle \phi^{low\ frequency} \right\rangle \approx \frac{P_0 \cdot l^2}{24 \cdot l \cdot t \cdot w \cdot \kappa_{bolo}} \cdot \left(1 + e^{j\omega t}\right) \qquad \text{Eq. 6.8}$$

$$Z_{thermal}^{low\ frequency} = \frac{\langle \phi \rangle}{P} \approx \frac{l}{12 \cdot t \cdot w \cdot \kappa_{bolo}} \qquad \text{Eq. 6.9}$$

Notice that the thermal impedance is independent of frequency.

At high frequency, a length of bar is much longer than thermal diffusion length, $L_{thermal}$.

$$|\gamma| \cdot l = \frac{l}{L_{thermal}} = \left| \sqrt{\frac{j \cdot \omega \cdot \rho \cdot C}{\kappa}} \right| \cdot l >> 1 \qquad \text{Eq. 6.10}$$

$$\left\langle \phi^{high\ frequency} \right\rangle \approx \frac{P_0}{2 \cdot l \cdot t \cdot w \cdot \kappa_{bolo}} \cdot \left(\frac{l^2}{12} - j \frac{\kappa_{bolo}}{\rho_{bolo} \cdot C_{bolo} \cdot \omega} \cdot e^{j\omega t} \right) \qquad \text{Eq. 6.11}$$

$$Z_{thermal}^{high\ frequency} = \frac{\langle \phi \rangle}{P} \approx \frac{1}{t \cdot w \cdot l \cdot \rho_{bolo} \cdot C_{bolo}} \cdot \frac{1}{j \cdot \omega} \qquad \text{Eq. 6.12}$$

These are the same limiting values as a thermal circuit consisting of a thermal resistance in parallel with a thermal capacitance.

$$R_{thermal} = \frac{l}{12 \cdot t \cdot w \cdot \kappa_{bolo}} = \frac{1}{12} \cdot \frac{\sigma_{bolo}}{\kappa_{bolo}} \cdot R_{bolo}^{electrical} \qquad \text{Eq. 6.13}$$

$$C_{thermal} = t \cdot w \cdot l \cdot \rho_{bolo} \cdot C_{bolo} \qquad \text{Eq. 6.14}$$

The thermal resistance is directly proportional to electric resistance, regardless of material. The speed of the detector is determined by

$$speed = \frac{1}{R_{thermal} \cdot C_{thermal}} = \frac{12\kappa_{bolo}}{\rho_{bolo} \cdot C_{bolo} \cdot l^2} \qquad \text{Eq. 6.15}$$

Note that the speed depends on only one dimension of the bolometer, the length *l*. *l* should be large since high thermal resistance $R_{thermal}$ can increase temperature rise. On the contrary l should be small for high speed. Therefore l has a tradeoff between temperature rise and the speed.

6.2 THERMAL MODEL FOR THE TEMPERATURE PROFILE

The temperature profile along the absorbing resistive bar would be helpful to calculate the responsivity, *NEP*, detectivity, and so on to characterize the microbolometers. In this section, we present the thermal model to determine the temperature profile affected by both incident IR power and the Joule power due to the bias heating.

6.2.1 Temperature Rise Due to IR Power Absorption

The metal layers act as antennas and then focus the incoming radiated power into a part of the absorbing resistive sheets. Here we assume that the locally focused power is uniformly dissipated in the focused region. In Figure 6.1, the temperature rise due to IR power absorption ϕ_{IR} along the absorbing resistive bar can be calculated using thermal diffusion equation as discussed in section 6.1. Notice that the thermal diffusion equation in section 6.1 is assumed that power is dissipated uniformly along a uniform bar of material. The thermal diffusion equation is

$$\frac{\partial^2 \phi}{\partial x^2} = \frac{\rho_{bolo} \cdot C_{bolo}}{\kappa_{bolo}} \cdot \frac{\partial \phi}{\partial t} - \frac{P_0\left(1 + e^{j\omega t}\right)}{2 \cdot l \cdot t \cdot w \cdot \kappa_{bolo}}. \qquad \text{Eq. 6.16}$$

And the temperature rise ϕ_{IR} along the bar is derived as

$$\phi(x,t) = \frac{P_0}{2 \cdot l \cdot t \cdot w \cdot \kappa_{bolo}} \left[\frac{l^2}{8} - \frac{x^2}{2} + j \frac{\kappa_{bolo}}{\rho_{bolo} \cdot C_{bolo} \cdot \omega} \cdot e^{j\omega t} \cdot \left\{ \frac{\cosh(\gamma x)}{\cosh(\gamma \cdot l/2)} - 1 \right\} \right]. \qquad \text{Eq. 6.17}$$

where

$$\gamma \equiv \sqrt{\frac{j\omega \rho_{bolo} C_{bolo}}{\kappa_{bolo}}} \qquad \text{Eq. 6.18}$$

So the average temperature rise can be determined by integrating $\mathrm{Re}[\phi_{IR}(x,t)]$ over x as

$$\left\langle \phi_{IR}(x,t) \right\rangle = \frac{1}{l}\int_{-\frac{l}{2}}^{\frac{l}{2}} \phi_{IR}(x,t)dx = \frac{1}{24}\cdot\frac{P_0 \cdot l}{t \cdot w \cdot \kappa}. \qquad \text{Eq. 6.19}$$

However, in Figure 6.2 and 6.3, the incoming power is not uniformly distributed along bars. The air-bridge absorbing resistive bar in Figure 6.2 can be redrawn as Figure 6.6.

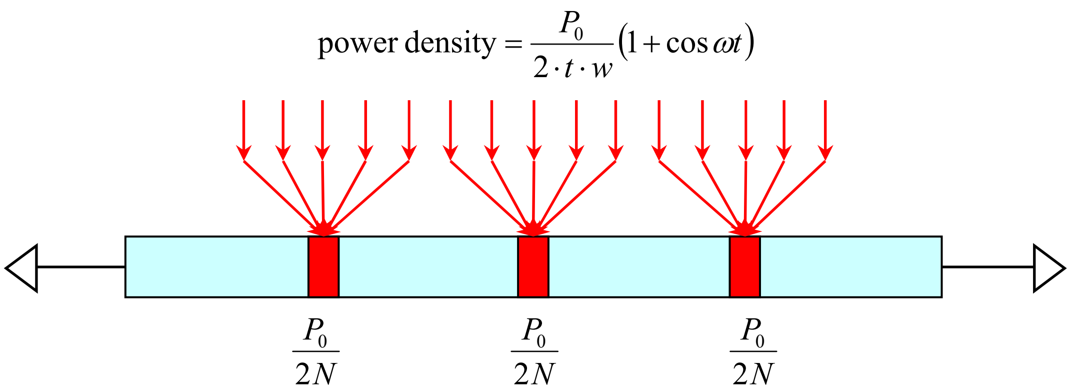

Figure 6.6: Thermal model for the air-bridge resistive bar in Figure 6.2.

The thermal model can be converted into the electrical model. In this case, the power P, thermal resistance R_{th}, and temperature rise ϕ are corresponding to the current I, electrical resistance R, and voltage V, respectively. Therefore, the thermal model in Figure 6.6 can be converted into the electrical model in Figure 6.7.

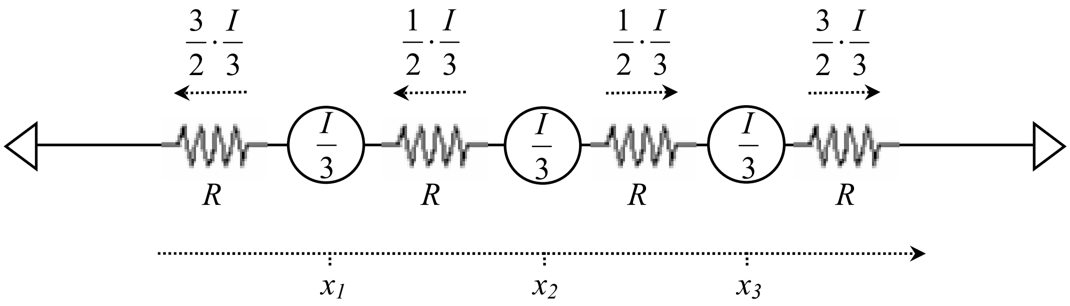

Figure 6.7: Electrical model for the air-bridge resistive bar converted from the thermal model in Figure 6.6.

In Figure 6.7, the temperature rises at the current sources are determined as

$$\phi_{1,IR} = \phi_{3,IR} = \frac{3}{2} \cdot \frac{P_0}{2 \cdot 3} \cdot R_{th} \qquad \text{Eq. 6.20}$$

$$\phi_{2,IR} = \frac{3}{2} \cdot \frac{P_0}{2 \cdot 3} \cdot R_{th} + \frac{1}{2} \cdot \frac{P_0}{2 \cdot 3} \cdot R_{th} \qquad \text{Eq. 6.21}$$

where $\phi_{1,IR}, \phi_{2,IR}, \text{and}\, \phi_{3,IR}$ are the temperature rises due to IR power absorption at $x=x_1$, x_2, and x_3, respectively. In this model, the number of thermal sources is fixed at 3. Based on the above derivations, the temperature rise profile $\phi_{n,IR}$ for N thermal sources due to IR power absorption can be derived as

$$\phi_{n,IR} = \frac{n}{2}(N - n + 1) \cdot \frac{P_0}{2N} \cdot \frac{l}{\kappa \cdot t \cdot w \cdot (N+1)} \qquad \text{Eq. 6.22}$$

where n=1, 2, ⋯ , N.

This generalized model can be verified using the thermal diffusion equation. In the above equation, when N equals infinity, the incoming power is distributed uniformly along the bar. In this case the average temperature rise can be determined as

$$\left\langle \phi_{IR}\big|_{N=\infty} \right\rangle = \frac{1}{l} \int_{-\frac{l}{2}}^{\frac{l}{2}} \phi_{IR}\big|_{N=\infty} dx = \frac{1}{24} \cdot \frac{P_0 \cdot l}{t \cdot w \cdot \kappa} \qquad \text{Eq. 6.23}$$

This equation is exactly the same as that derived from the thermal diffusion equation as above. Consequently, we can find the temperature rise profile along the bar ϕ_{IR} due to IR absorption.

6.2.2 Temperature Rise Due to the Bias Heating

In the section 6.2.1, we derive temperature rise along the bar assuming that the conductivity is independent of the temperature. In reality, the conductivity is dependent on the temperature. As the temperature goes up, it makes the conductivity change. This changed conductivity affects the temperature rise again. These two parameters interact with each other continuously. Therefore the feedback temperature rise due to temperature dependent conductivity needs to be considered.

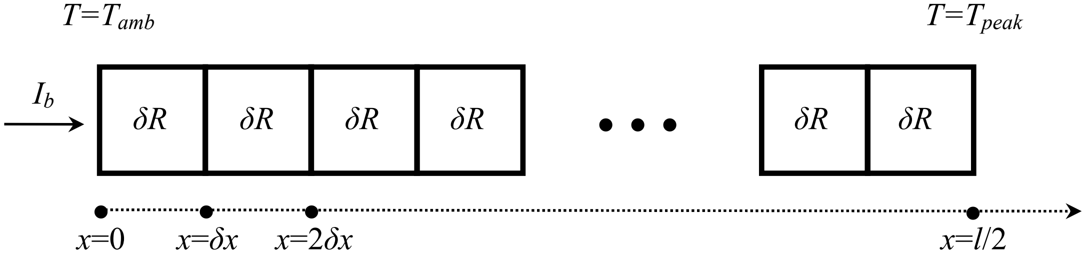

Figure 6.8: Discretized resistive bar to consider the feedback temperature rise due to temperature dependent conductivity.

In this section we only consider the bias heating due to the bias current I_b assuming no IR power absorption. For the numerical approach, let's discretize the bar as in Figure 6.8. We only simulate a half of the bar since it is symmetric. The initial temperature rise at $x=\delta x$, $\phi_{bias}(x=\delta x)$ is determined by the product of the thermal resistance of the δx long segment of the bar, δR_{th}, and the power going through the δx long segment of the bar, $P_{\delta x}$.

$$\begin{aligned}\phi_{bias}(x=\delta x) &= P_{\delta x}\cdot\delta R_{th} = I_b^2(R-\delta R)\cdot\frac{\delta x}{\kappa\cdot t\cdot w}\\ &= I_b^2\cdot\int_{\delta x}^{\frac{l}{2}}\frac{1}{\sigma\left(T|_{x=0}\right)\cdot t\cdot w}dx\cdot\frac{\delta x}{\kappa\cdot t\cdot w} = I_b^2\cdot\frac{l/2-\delta x}{\sigma\left(T|_{x=0}\right)}\cdot\frac{\delta x}{\kappa\cdot t\cdot w}\end{aligned} \qquad \text{Eq. 6.24}$$

where R is the total electrical resistance of the bar. And the temperature at $x=\delta x$ is

$$T|_{x=\delta x,bias} = T_{amb} + \phi_{bias}(x=\delta x). \qquad \text{Eq. 6.25}$$

Similarly, the initial temperature rise at $x=2\delta x$ is determined by

$$\begin{aligned}\phi_{bias}(x=2\delta x) &= P_{2\delta x}\cdot\delta R_{th} = I_b^2(R-2\delta R)\cdot\frac{\delta x}{\kappa\cdot t\cdot w}\\ &= I_b^2\cdot\int_{2\delta x}^{\frac{l}{2}}\frac{1}{\sigma\left(T|_{x=\delta x,bias}\right)\cdot t\cdot w}dx\cdot\frac{\delta x}{\kappa\cdot t\cdot w} = I_b^2\cdot\frac{l/2-2\delta x}{\sigma\left(T|_{x=0}\right)}\cdot\frac{\delta x}{\kappa\cdot t\cdot w}\end{aligned} \qquad \text{Eq. 6.26}$$

and the temperature at $x=2\delta x$ is

$$T|_{x=2\delta x,bias} = T|_{x=\delta x,bias} + \phi_{bias}(x=2\delta x). \qquad \text{Eq. 6.27}$$

In this way, the initial temperature profile from x=0 to x=l/2 can be determined. To consider the temperature dependent conductivity, the temperature profile along the bar needs to be recalculated based on the initial temperature profile. Now the temperature rise at x=δx is determined by

$$\begin{aligned}\phi_{bias}(x=\delta x) &= P_{\delta x}\cdot\delta R_{th} = I_b^2(R-\delta R)\cdot\frac{\delta x}{\kappa\cdot t\cdot w}\\ &= I_b^2\cdot\int_{\delta x}^{\frac{l}{2}}\frac{1}{\sigma[T_{bias}(x)]\cdot t\cdot w}dx\cdot\frac{\delta x}{\kappa\cdot t\cdot w}\end{aligned}\qquad \text{Eq. 6.28}$$

and the temperature at x=δx is

$$T\big|_{x=\delta x,bias} = T_{amb}+\phi_{bias}(x=\delta x). \qquad \text{Eq. 6.29}$$

Similarly, the temperature rise at x=2δx is determined by

$$\begin{aligned}\phi_{bias}(x=2\delta x) &= P_{2\delta x}\cdot\delta R_{th} = I_b^2(R-2\delta R)\cdot\frac{\delta x}{\kappa\cdot t\cdot w}\\ &= I_b^2\cdot\int_{2\delta x}^{\frac{l}{2}}\frac{1}{\sigma[T_{bias}(x)]\cdot t\cdot w}dx\cdot\frac{\delta x}{\kappa\cdot t\cdot w}\end{aligned}\qquad \text{Eq. 6.30}$$

and the temperature at x=2δx is

$$T\big|_{x=2\delta x,bias} = T\big|_{x=\delta x,bias}+\phi_{bias}(x=2\delta x). \qquad \text{Eq. 6.31}$$

Similarly the temperature profile from x=0 to x=l/2 can be determined. Until now we have iterated twice to find the temperature profile along the bar. But the temperature profile changed by the second iteration affects the conductivity again, and the conductivity also affects the temperature profile. So we continue the iterations until the temperature profile converges. Consequently, we can find the temperature rise profile along the bar due to bias heating. When there is no IR incident power, the total resistance of the resistive bar is

$$R_{bias} = \int_{-\frac{l}{2}}^{\frac{l}{2}}\frac{1}{\sigma[T_{bias}(x)]\cdot t\cdot w}dx \qquad \text{Eq. 6.32}$$

6.2.3 Temperature Rise Due to IR Power Absorption and Bias Heating

We have shown two temperature rise profiles. One is due to IR power absorption, and the other is due to bias heating. In these processes, we also considered the feedback temperature due to the temperature dependent conductivity. In the real microbolometers, IR power absorption and the bias heating happen simultaneously. So we combine these two temperature rise profiles.

The initial temperature rise at $x=\delta x$ is determined by

$$\begin{aligned}\phi(x=\delta x) &= \left(P_{\delta x,IR}+P_{\delta x,bias}\right)\cdot \delta R_{th}\\ &= \phi_{IR}(x=\delta x)+\phi_{bias}(x=\delta x)\\ &= \phi_{IR}(x=\delta x)+I_b^2\cdot\frac{l/2-\delta x}{\sigma\left(T\big|_{x=0}\right)}\cdot\frac{\delta x}{\kappa\cdot t\cdot w}\end{aligned} \qquad \text{Eq. 6.33}$$

and the temperature at $x=\delta x$ is

$$T\big|_{x=\delta x}=T_{amb}+\phi(x=\delta x). \qquad \text{Eq. 6.34}$$

Similarly, the initial temperature rise at $x=2\delta x$ is determined by

$$\begin{aligned}\phi(x=2\delta x) &= \left(P_{2\delta x,IR}+P_{2\delta x,bias}\right)\cdot \delta R_{th}\\ &= \phi_{IR}(x=2\delta x)+I_b^2(R-2\delta R)\cdot\frac{\delta x}{\kappa\cdot t\cdot w}\\ &= \phi_{IR}(x=2\delta x)+I_b^2\cdot\frac{l/2-2\delta x}{\sigma\left(T\big|_{x=0}\right)}\cdot\frac{\delta x}{\kappa\cdot t\cdot w}\end{aligned} \qquad \text{Eq. 6.35}$$

and the temperature at $x=2\delta x$ is

$$T\big|_{x=2\delta x}=T\big|_{x=\delta x}+\phi(x=2\delta x). \qquad \text{Eq. 6.36}$$

In this way, the initial temperature profile from $x=0$ to $x=l/2$ for both IR power absorption and bias heating can be determined. To consider the temperature dependent conductivity, the temperature profile along the bar needs to be recalculated based on the initial temperature profile. Now the temperature rise at $x=\delta x$ is determined by

$$\begin{aligned}\phi(x=\delta x) &= \left(P_{\delta x,IR}+P_{\delta x,bias}\right)\cdot \delta R_{th}\\ &= \phi_{IR}(x=\delta x)+\phi_{bias}(x=\delta x)\\ &= \phi_{IR}(x=\delta x)+I_b^2\cdot\int_{\delta x}^{l/2}\frac{1}{\sigma[T(x)]\cdot t\cdot w}dx\cdot\frac{\delta x}{\kappa\cdot t\cdot w}\end{aligned} \qquad \text{Eq. 6.37}$$

and the temperature at $x=\delta x$ is

$$T\big|_{x=\delta x}=T_{amb}+\phi(x=\delta x). \qquad \text{Eq. 6.38}$$

Similarly, the initial temperature rise at $x=2\delta x$ is determined by

$$\begin{aligned}\phi(x=2\delta x) &= \left(P_{2\delta x,IR}+P_{2\delta x,bias}\right)\cdot \delta R_{th}\\ &= \phi_{IR}(x=2\delta x)+\phi_{bias}(x=2\delta x)\\ &= \phi_{IR}(x=2\delta x)+I_b^2\cdot\int_{2\delta x}^{l/2}\frac{1}{\sigma[T(x)]\cdot t\cdot w}dx\cdot\frac{\delta x}{\kappa\cdot t\cdot w}\end{aligned} \qquad \text{Eq. 6.39}$$

and the temperature at $x=2\delta x$ is

$$T\big|_{x=2\delta x}=T_{amb}+\phi(x=2\delta x). \qquad \text{Eq. 6.40}$$

Similarly the temperature profile from $x=0$ to $x=l/2$ can be determined.

Now we iterated twice to find the temperature profile along the bar. But the temperature profile changed by the second iteration affects the conductivity, and the conductivity also affects the temperature profile. So we continue the iterations until the temperature profile converges. When there is IR incident power, the total resistance of the resistive bar is

$$R_{bias+IR}=\int_{-\frac{l}{2}}^{\frac{l}{2}}\frac{1}{\sigma[T(x)]\cdot t\cdot w}dx \qquad \text{Eq. 6.41}$$

Figure 6.9 shows the temperature profile from the initial temperature profile to converged temperature profile. l is 62μm, g=2μm, w=0.1μm, N=9, I_b=0.03mA, and P_0 =5×10^{-9}W. The bolometer material is Bismuth characterized by the following parameters. α_{Bi}=0.003K^{-1}, κ_{Bi}=1.8W·m^{-1}·K^{-1}, σ_{Bi}=133300S/m, ρ_{Bi}=9.86×10^{6}g·m^{-3}, and C_{Bi}=0.12J·g^{-1}·K^{-1}. Note that most of the temperature rise is due to the bias heating rather than IR power absorption.

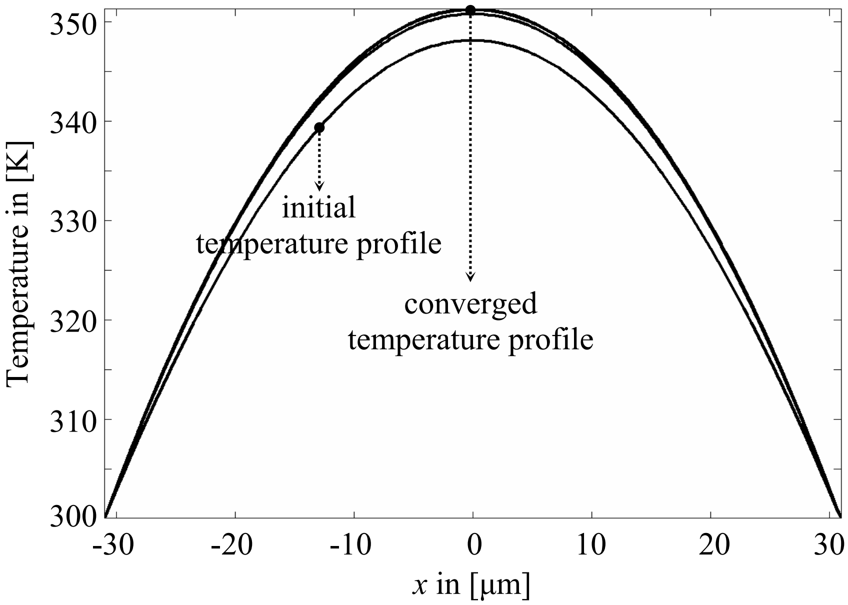

Figure 6.9: Temperature profile along the bar due to IR power absorption and the bias heating. Temperature dependent conductivity has been considered.

6.3 CHARACTERISTICS OF THE MODIFIED PLANAR MULTIMODE DETECTORS

The thermal isolation due to air-bridge absorbing resistive bars can be represented electrically by capacitance that is very small since the distance between the elevated absorbing resistive layers and metal layers is much smaller than the operating wavelengths (Figure 6.10). Therefore this thermal isolation improves the devices thermally rather than electrically. In addition, a microbolometer's performance such as the responsivity, *NEP*, detectivity, and so on can be enhanced by increasing its thermal impedance. In the presented geometries, the thermal impedances are increased by making the absorbing resistive bar long.

In the previous section 6.2, we presented the methods of analyzing the thermal behaviors along the absorbing resistive bar when the bias current I_b is applied, and the incident IR power is focused on several areas along the bar due to the antenna structures. These methods can be applied to the thermally improved planar multimode detectors in

Figure 6.1, 6.2, and 6.3 to determine several parameters such as the responsivity, *NEP*, speed, and so on.

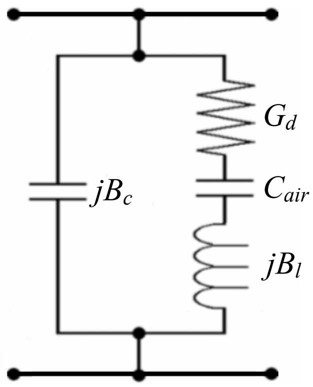

Figure 6.10: Equivalent electrical model of the grid part in Figure 6.1. The air-gap between absorbing resistive sheets and metal can be represented as the capacitor C_{air}.

6.3.1 Characteristics of Microbolometers When *N*=1

As shown in Figure 6.1, the geometry is similar to the original planar multimode detectors (Figure 2.6) except for the elevation of the absorbing resistive bars. Its number of thermal sources on each bar *N* equals 1. Figure 6.11 shows the equivalent circuit model of the interwoven grid of metallic and resistive bars. In Figure 6.11 the total resistance of the grid $R_{total,N=1}$ is determined by

$$R_{total,N=1} = 3\times\left(R_{N=1} // R_{N=1} // R_{N=1}\right) = R_{N=1} \qquad \text{Eq. 6.42}$$

where $R_{N=1}$ is the electrical resistance of each bar when *N*=1. The current passing through each bar is one third of the bias current I_b.

In Chapter 1.2.2, the responsivity is defined as

$$\Re = \frac{\Delta V}{P_{incident}} = \frac{I_b \cdot \Delta R}{P_{incident}} = \frac{I_b \cdot \left\{R_{total,N=1,bias+IR}(T) - R_{total,N=1,bias}(T)\right\}}{P_{incident}}. \qquad \text{Eq. 6.43}$$

where $R_{total,N=1,bias+IR}$ is the total resistance of a single pixel when both bias current and incident IR power are applied, and $R_{total,N=1,bias}$ is the total resistance of a single pixel when only the bias current is applied. As shown above, the total resistance of the pixel $R_{total,N=1}$ is same as the resistance of each resistive bar $R_{N=1}$. So the responsivity can be expressed as

$$\Re_{N=1} = \frac{I_b \cdot \{R_{N=1,bias+IR}(T) - R_{N=1,bias}(T)\}}{P_{incident}}. \qquad \text{Eq. 6.44}$$

$$R_{N=1,bias} = \int_{-\frac{l}{2}}^{\frac{l}{2}} \frac{1}{\sigma[T_{bias}(x)] \cdot t \cdot w} dx. \qquad \text{Eq. 6.45}$$

$$R_{N=1,bias+IR} = \int_{-\frac{l}{2}}^{\frac{l}{2}} \frac{1}{\sigma[T(x)] \cdot t \cdot w} dx. \qquad \text{Eq. 6.46}$$

where $T_{bias}(x)$ is the temperature profile when only the bias current is applied to the resistive bar, and $T(x)$ is the temperature profile when both the bias current and incident IR power are applied. Both temperature profiles can be determined using the methods discussed in the previous section 6.2.

The responsivity is proportional to the bias current I_b. So the responsivity can be enhanced by increasing the bias current. However, excessive currents generate thermal runaway. The thermal runaway is a phenomenon of electro-thermal interaction where the equipment continues to generate heat faster than it can be dissipated. The temperature will continue to rise until the equipment fails or a fire breaks out. There are many causes for the thermal runaway including defective design, improper installation and control system failure. In microbolometers with metal bolometer materials, the bias current heats up the absorbing resistive sheets, and their conductivities are changed due to the increased temperature, and then the changed conductivities increase the temperature again. With relevant bias currents, the temperature rise converges. But with excessive bias currents, the temperature rise diverges, and generates the thermal runaway. Therefore there exists an upper limit of the bias current for stable systems.

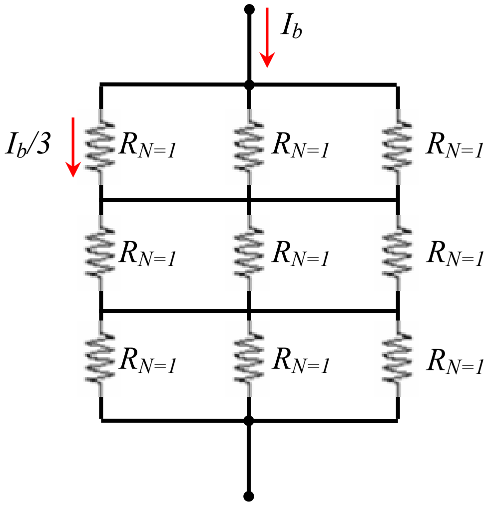

Figure 6.11: Equivalent circuit model representing the interwoven grid of the thermally improved planar multimode detectors when N=1. The whole geometry including the mirror is shown in Figure 6.1.

6.3.2 Characteristics of Microbolometers When *N*=3

To increase the thermal impedance, we connect the absorbing resistive bars in the same column of the original planar multimode detectors (Figure 2.4) in series, and elevate in the air as shown in Figure 6.2. In this case, three areas along the each resistive bar would be the thermal sources due to the metal antenna structure (Figure 6.12). Figure 6.13 shows the equivalent circuit model of the interwoven grid of metallic and resistive bars. In Figure 6.13 the total resistance of the grid $R_{total,N=3}$ is determined by

$$R_{total,N=3} = R_{N=3} // R_{N=3} // R_{N=3} = \frac{R_{N=3}}{3} \qquad \text{Eq. 6.47}$$

where $R_{N=3}$ is the resistance of each bar when the number of thermal sources on each bar, N, equals 3 (Figure 6.12). The current passing through each bar is one third of the bias current I_b.

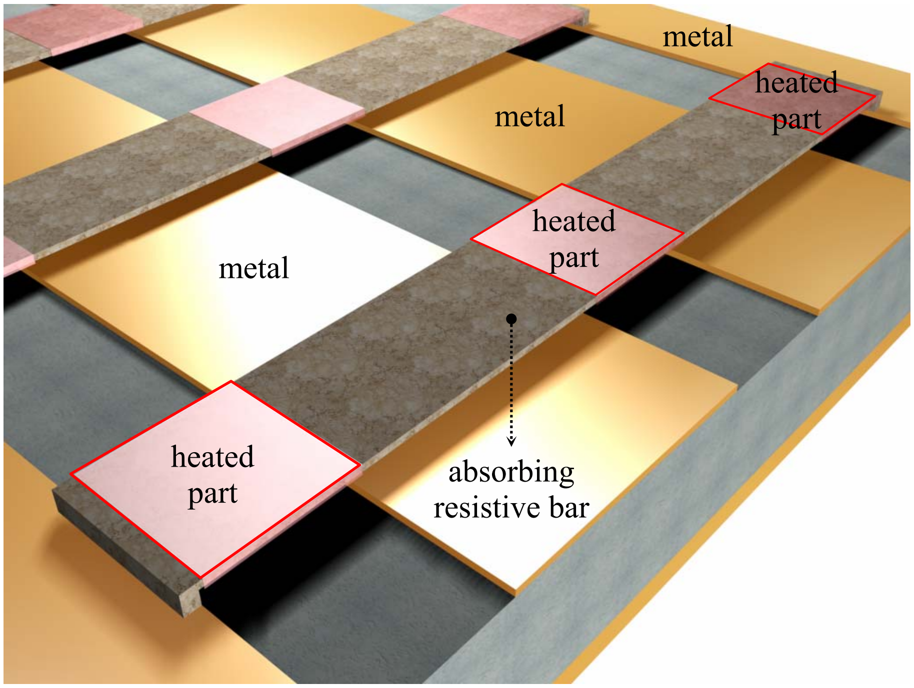

Figure 6.12: Three areas along each resistive bar are thermally heated due to the antenna structure, i.e. *N*=3. Focused and detailed from Figure 6.2.

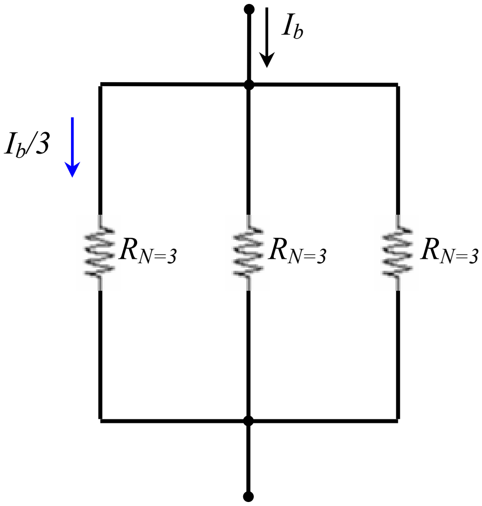

Figure 6.13: Equivalent circuit model of the thermally improved planar multimode detectors shown in Figure 6.2.

Similarly as the section 6.3.1, the responsivity can be determined as

$$\Re_{N=3}=\frac{\Delta V}{P_{incident}}=\frac{I_b\cdot\Delta R}{P_{incident}}=\frac{I_b\cdot\{R_{total,N=3,bias+IR}(T)-R_{total,N=3,bias}(T)\}}{P_{incident}} \quad \text{Eq. 6.48}$$

$$\Re_{N=3}=\frac{I_b\cdot\{R_{N=3,bias+IR}(T)-R_{N=3,bias}(T)\}}{3\cdot P_{incident}}. \quad \text{Eq. 6.49}$$

$$R_{N=3,bias}=\int_{-\frac{l}{2}}^{\frac{l}{2}}\frac{1}{\sigma[T_{bias}(x)]\cdot t\cdot w}dx. \quad \text{Eq. 6.50}$$

$$R_{N=3,bias+IR}=\int_{-\frac{l}{2}}^{\frac{l}{2}}\frac{1}{\sigma[T(x)]\cdot t\cdot w}dx. \quad \text{Eq. 6.51}$$

where $T_{bias}(x)$ is the temperature profile when only the bias current is applied to the resistive bar, and $T(x)$ is the temperature profile when both the bias current and incident IR power are applied. Both temperature profiles can be determined using the methods discussed in the previous section 5.1. The thermal runaway limits the bias current.

6.3.3 Characteristics of Microbolometers When N=9

To increase the thermal impedance, we connect all absorbing resistive bars of the original planar multimode detectors (Figure 2.6) in series, and elevate in the air as shown in Figure 6.3. In this case, nine areas along the each resistive bar would be the thermal sources due to the metal antenna structure (Figure 6.14). The total resistance of the grid $R_{total,N=9}$ is determined by

$$R_{total,N=9}=R_{N=9} \quad \text{Eq. 6.52}$$

where $R_{N=9}$ is the resistance of each bar when the number of thermal sources on each bar, N, equals to 9 (Figure 6.14). The current passing through each bar is the same as the bias current I_b. Similarly as in section 6.3.1, the responsivity can be determined as

$$\Re_{N=9}=\frac{\Delta V}{P_{incident}}=\frac{I_b\cdot\Delta R}{P_{incident}}=\frac{I_b\cdot\{R_{total,N=9,bias+IR}(T)-R_{total,N=9,bias}(T)\}}{P_{incident}} \quad \text{Eq. 6.53}$$

$$\Re=\frac{I_b\cdot\{R_{N=9,bias+IR}(T)-R_{N=9,bias}(T)\}}{P_{incident}}. \quad \text{Eq. 6.54}$$

$$R_{N=9,bias} = \int_{-\frac{l}{2}}^{\frac{l}{2}} \frac{1}{\sigma[T_{bias}(x)] \cdot t \cdot w} dx \,. \qquad \text{Eq. 6.55}$$

$$R_{N=9,bias+IR} = \int_{-\frac{l}{2}}^{\frac{l}{2}} \frac{1}{\sigma[T(x)] \cdot t \cdot w} dx \,. \qquad \text{Eq. 6.56}$$

where $T_{bias}(x)$ is the temperature profile when only the bias current is applied to the resistive bar, and $T(x)$ is the temperature profile when both the bias current and incident IR power are applied. Both temperature profiles can be determined using the methods discussed in the previous section 6.2. The thermal runaway limits the bias current.

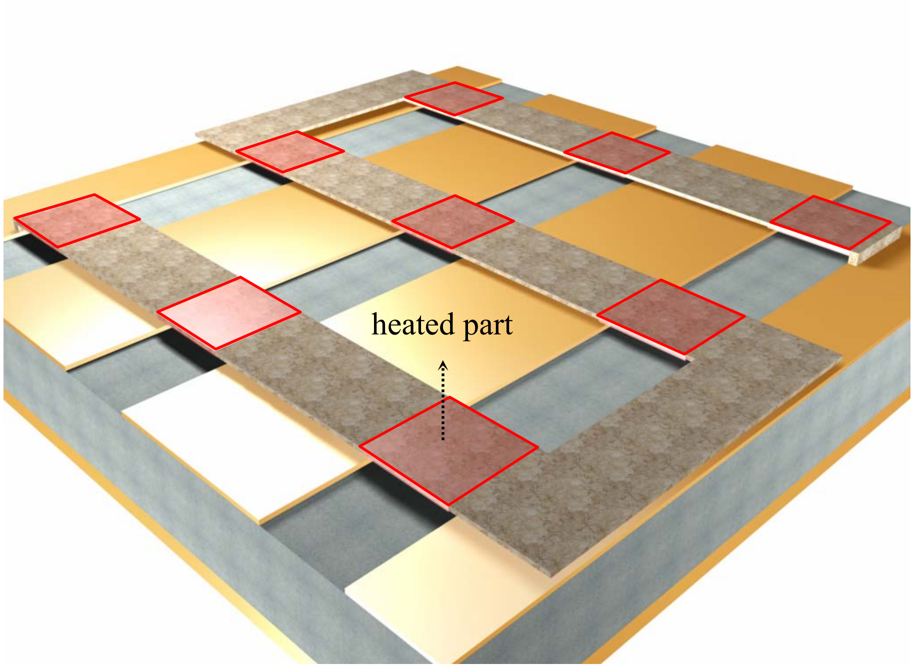

Figure 6.14: Nine areas along each resistive bar are thermally heated due to the antenna structure, i.e. N=9. Focused and detailed from Figure 6.3.

6.4 NUMERICAL RESULTS

The bias current and incident IR power are important parameters for the responsivity. First of all, we fix them for all three modified planar multimode detectors (N=1, 3, and 9). Table 6.1 shows the dimensions of the resistive bars and figures of merits. In this table, the best design is the elevated serpentine design (*N*=9). The thermal impedance is proportional to the length of the bar. Therefore, the longer length, the better design from the perspective of the responsivity, *NEP*, and detectivity. Here the basic array dimensions are the same as those of the solid line in Figure 2.6 having the strong absorption at 10μm wavelength, and the bolometer material is Platinum characterized by the following parameters. α_{Pt}=0.0028K^{-1}, κ_{Pt}=72W·m^{-1}·K^{-1}, σ_{Pt}=9.1×10^{6}S/m, ρ_{Pt}=21.5×10^{6}g·m^{-3}, and C_{Pt}=0.13J·g^{-1}·K^{-1}.

	N=1 (Figure 6.1)	*N*=3 (Figure 6.2)	*N*=9 (Figure 6.3)
l [μm]	0.6	14.4	63.2
t [μm]	0.14		
w [μm]	3		
P_0 [W]	1×10^{-8}		
I_b [A]	5.0×10^{-5}		
$\Re$ [V/W]	1.7×10^{-1}	4.9×10^{1}	6.6×10^{4}
NEP $[W/\sqrt{Hz}]$	3.6×10^{-7}	3.5×10^{-10}	1.4×10^{-12}
D^* $[cm\sqrt{Hz}/W]$	5.8×10^{4}	6.0×10^{6}	1.5×10^{9}
$NETD$ $[K]$	1.3×10^{3}	1.2×10^{1}	4.9×10^{-3}

Table 6.1: Numerical results of three modified planar multimode detectors (*N*=1, 3, and 9) when the bias currents are fixed for all three cases.

As discussed in section 6.3, each design has its own maximum bias current due to the thermal runaway. Table 6.2 shows the maximum bias current $I_{b,max}$ of each design and corresponding *NEP*s and detectivities. In this table, as the number of thermal sources on the bar *N* goes up, the maximum bias current gets smaller. The responsivity is proportional to the bias current so that high bias current leads to high responsivity.

However, in these results, it seems like the thermal impedance is more dominant than the bias current in the responsivity. Even though the highest bias current is allowed when *N*=1, the best responsivity is when *N*=9; the highest thermal impedance. Consequently, one can say that the best sensitivity is achieved by increasing the thermal impedance. In our case, the elevated serpentine (Figure 6.3) has the best sensitivity.

	N=1 (Figure 6.1)	*N*=3 (Figure 6.2)	*N*=9 (Figure 6.3)
l [µm]	0.6	14.4	63.2
t [µm]	0.14		
w [µm]	3		
P_0 [W]	1×10^{-8}		
$I_{b,max}$ [A]	1.3×10^{-2}	5.5×10^{-4}	5.0×10^{-5}
$\Re_{max}$ [V/W]	3.4×10^{2}	1.0×10^{4}	6.6×10^{4}
NEP_{min} [W]	2.5×10^{-11}	2.5×10^{-12}	1.4×10^{-12}
D^*_{max} $[cm\sqrt{Hz}/W]$	8.4×10^{7}	8.4×10^{8}	1.5×10^{9}
$NETD$ $[K]$	8.7×10^{-2}	8.7×10^{-3}	4.9×10^{-3}

Table 6.2: Numerical results of three modified planar multimode detectors (*N*=1, 3, and 9) when each design has the maximum bias current, $I_{b,max}$.

Chapter 7: Conclusions

This work has presented an approach to design antenna coupled infrared detectors (planar multimode detectors) for wavelength selectivity, and dielectric coated Salisbury Screen and Jaumann Absorber for wavelength selectivity and broad band absorption.

In Chapter 2, we presented planar multimode detectors. It was shown that planar multimode detectors can maintain strong absorption at a specified wavelength within long wave infrared (LWIR) range with diverse bandwidth. Its bandwidth can be narrow enough to construct multiple channels within LWIR range for hyper-spectral imaging. The diversity of the solutions is an advantage of this multimode detector, allowing a search for desired characteristics. The genetic algorithm (GA) was adopted as an optimization scheme. The electromagnetic behavior of the planar multimode detectors has been analyzed using a modification of waveguide post mount-analysis (so called Eisenhart and Khan's analysis) and ABCD matrix analysis, and verified by the commercial finite element method (FEM) full wave simulation program, Ansoft HFSS.

In Chapter 3, a wavelength selective three-pixel design, each pixel using different lithographically drawn dimension array period a, capacitive gap width g, and inductive post width w, with identical air gap thickness d and sheet resistance of bolometric layer R_S, was presented. Changing the wavelength selectivity of each pixel by changing only lithographical parameters should not require a fabrication process with different sacrificial layer thicknesses under different pixels in the array, resulting in a less complex fabrication process. The planar multimode detectors may be tuned by only changing the distance between grid and a mirror with the fixed array dimension (a, g, w, and R_s).

However, redundant and ambiguous power absorption resulted from long wavelength absorption and low power absorption at short wavelength region make tuning by the distance *d* unattractive even though the mechanical actuation of planar multimode detectors provides better wavelength selectivity than the conventional Salisbury Screen.

In Chapter 3, the wavelength selective microbolometers in parallel were introduced for the multi-spectral imaging. Another approach to achieve the multi-spectral imaging capabilities using microbolometer arrays would be the use of 'stackable' array. Vertically stacking bolometers is a more compact and highly integrated structure than parallel locating of those. In Chapter 4 and 5, we discussed stacked planar multimode detectors and stacked Salisbury Screens (Jaumann Absorbers) for 2 or 3-color wavelength selectivity. It was shown that vertically stacked planar multimode detectors can provide 2-color wavelength selectivity, and dielectric coated Jaumann Absorbers can also provide 2- or 3-color wavelength selectivity in LWIR range. We have shown that as the number of layers in the stack goes up, the wavelength selectivity gets worse. Therefore, placing more than 4 separate absorbing layers in a stack actually reduces wavelength selectivity and does not produce useful four color wavelength selectivity. The Jaumann Absorbers can also be used for broad band absorption covering both mid wave infrared (MWIR) and LWIR, 3~13μm wavelengths by summing the signals of every bolometric layer. The Jaumann Absorbers can generate broader bandwidth than the Salisbury Screen can.

In Chapter 6, we modified the planar multimode detectors for high sensitivity and better thermal behaviors by air-bridging only absorbing bolometric layers instead of the whole interwoven grid with its support layer. The thermal isolation due to air-bridge absorbing resistive bars can be represented electrically by capacitance that is very small since the distance between the elevated absorbing resistive layers and metal layers is much smaller than the operating wavelengths. Therefore this thermal isolation improves the microbolometers thermally rather than electrically. It was shown that air-bridged long and narrow absorbing sheets increase thermal impedance and improve responsivity, *NEP*, detectivity, speed, and so on.

The next step in this work would be to fabricate the GA-optimized designs, and to measure them. In conclusion, we have outlined some of the important considerations for designing wavelength-selective or broadband infrared detectors in long wave infrared and/or mid wave infrared range. This scheme will hopefully provide guidance for fabricating devices.

Appendix A

Planar Multimode Detector with a Mirror

```
% This program handles the planar multimode detector with a mirror discussed in
% Chapter 2.

% Assumption: An array period 'a' can not be greater than the operating wavelength. This
%             limit is imposed by the possibility that the structure may act as a grating,
%             diffracting energy into new reflected or transmitted waves of into surface
%             waves.

clear;close all

a=6.90e-6;     % array period in [m]
w=3.00e-6;     % inductive post width in [m]
g=0.20e-6;     % capacitive gap width in [m]
d=3.29e-6;     % air gap between the grid and mirror in [m]
Rs=53.49;      % sheet resistance of the absobing sheet in [ohm]

lambda_band=linspace(7,14,200)*1e-6;     % wavelength band in [m]

eps0=1/(36*pi)*1e-9;     % perimittivity of free space in [F/m]
mu0 =4*pi*1e-7;          % permeability of free space in [H/m]
c=3e8;                   % light of speed in [m/sec]

eps_r=1.0;     % relative permittivity (dielectric constant) of free space
mu_r =1.0;     % relative permeability of free space
Z0=377;        % characteristic impedance of free space in [ohms]

% Calculate a normalized capacitive susceptance

for n1=1:length(lambda_band)
    lambda=lambda_band(n1);
    jB_c(n1)=0;

    for n=1:10
        if mod(a,g)==0
            jB_c(n1)=jB_c(n1)+0;
        else
            jB_c(n1)=jB_c(n1)+(sin(n*pi*g/a)/(n*pi*g/a))^2…
                    *(1/sqrt(n^2-(a/lambda)^2)+eps_r…
                    /sqrt(n^2-(a/(lambda/sqrt(eps_r)))^2));
        end
```

```
        end

        % jB_c: admittance of the capacitance of the grid
        jB_c(n1)=+j*sqrt(eps0/mu0)*2*(1-g/a)*a./lambda*jB_c(n1);
end

% Calculate a normalized inductive susceptance

for n1=1:length(lambda_band)
        lambda=lambda_band(n1);
        m_sum(n1)=0;
        for m=1:10
                n_sum(m)=0;
                for n=1:10
                        n_sum(m)=n_sum(m)+2*(sin(n*pi*g/a)/(n*pi*g/a))^2*…
                                        (((a/lambda)^2-m^2) /sqrt((a/lambda)^2-m^2-n^2)…
                                        +((a/(lambda/sqrt(eps_r)))^2-m^2)/sqrt((a/(lambda…
                                        /sqrt(eps_r)))^2-m^2-n^2));
                end
                m_sum(n1)=m_sum(n1)+(sin(m*pi*w/a)/(m*pi*w/a))^2…
                                *((sqrt((a/lambda)^2-m^2)+sqrt((a/(lambda…
                                /sqrt(eps_r)))^2-m^2))+n_sum(m))^-1;
        end

        jB_l(n1)=-(2*a/lambda*sqrt(mu0/eps0)*m_sum(n1))^-1;
end

G_d=1/(Rs*g/w);      % electric resistance of the absorbing resistive sheet

% Determine the power absorption efficiency

for n1=1:length(lambda_band)

        lambda=lambda_band(n1);      % operating wavelength

        % Y_grid : admittance of the grid
        Y_grid=jB_c(n1)+G_d*jB_l(n1)/(G_d+jB_l(n1));

        % 'M1' is the ABCD matrix for the grid part.
        M1=[1,0;Y_grid,1];

        beta=2*pi/lambda;
        % 'M3' is the ABCD matrix for the air gap between the grid and mirror.
        M2=[cos(beta*d),j*Z0*sin(beta*d);j/Z0*sin(beta*d),cos(beta*d)];
        V3=0;      % in [V]
```

```
    I3=1;     % in [A]

    V2I2=M2*[V3;I3];
    V2=V2I2(1);
    I2=V2I2(2);
    P2=0.5*real(V2*I2');

    V1I1=M1*[V2;I2];
    V1=V1I1(1);
    I1=V1I1(2);
    P1=0.5*real(V1*I1');
    V1p=0.5*(V1+Z0*I1);

    P_abs=P1-P2;     % power absorbed by the absorbing layer
    P_ins=0.5*(abs(V1p))^2/Z0;     % incident power

    P_abs_effi(n1)=abs(P_abs/P_ins);     % power absorption efficiency
end

figure(1)
plot(lambda_band*1e6,P_abs_effi,'r','LineWidth',3)
xlabel('Wavelength {\it\lambda} in [{\it\mum}]');ylabel('Power Absorption Efficiency')
axis([lambda_band(1)*1e6 lambda_band(end)*1e6 0 1])

% Reference
% D.B.Rutledge and S.E.Schwarz, 'Planar Multimode Detector Arrays for Infrared and
% Millimeter-Wave Applications',IEEE journal of Quantum Electronics, Vol. QE-17,
% No. 3, Mar 1981.
```

References

1 P. W. Kruse, "Uncooled thermal imaging: arrays, systems, and applications," vol. TT51, SPIE Press, Bellingham, WA, 2001.

2 Roglaski, *Infrared Detectors*, Gorden and Breach Science Publishers, 2000.

3 P. W. Kruse and D. D. Skatrud, *Uncooled Infrared Imaging Arrays and Systems*, Academic Press, 1997.

4 www.x20.org

5 J. L. Tissot, "IR detection with uncooled sensors," *Infrared Physics & Technology*, 2004

6 S. P. Langley, "The bolometer," *Nature* **25**, 14-16, 1881.

7 T. L. Hwang, S. E. Schwarz, and D. B. Rutledge, "Microbolometers for infrared detection," *Applied Physics Letter*, vol. 34, pp. 773, 1979.

8 Xingjian Yi, Changhong Chen, Luqin Liu, Yingrui Wang, Bifeng Xiong, Hongchen Wang, and Sihai Chen, "A new fabrication method for vanadium dioxide thin films deposited by ion beam sputtering," *Infrared Physics & Technology*, vol. 44, no. 2, April 2003, Pages 137-141.

9 D. Zintu, G. Tosone and A. Mercuri, "Dual ion beam sputtering vanadium dioxide microbolometers by surface micromachining," *Infrared Physics & Technology*, vol. 43, no. 3-5, June 2002, Pages 245-250.

10 A. Jahanzeb, C. M. Travers, Z. Celik-Butler, D. P. Butler, S. G. Tan, "A semiconductor YBaCuO microbolometer for room temperature IR imaging," *IEEE Transactions on Electron Devices*, vol. 44, no. 10, Oct. 1997, pp.1795-1801.

11 C. M. Travers, A. Jahanzeb, D. P. Butler, Z. Celik-Butler, “Fabrication of semiconducting YBaCuO surface-micromachined bolometer arrays,” *Journal of Microelectromechanical Systems*, vol. 6, no.3, Sept. 1997, pp. 271-276.

12 R.C. Jones, Proc. IRE 47, 1495 (1959).

13 J. Lewis, *Far Infrared and Sub-Millimeter Wavelength Microbolometer Detectors*, PhD. Dissertation, The University of Texas at Austin, 1994.

14 S. E. James, S. J. Yoo, J. C. Warner, D. P. Neikirk, and J. T. McDevitt, “Lithographically Patterned Superconductor Bolometer Detector for Visible and Near Infrared Radiation Incorporating Wavelength Selective Light Absorbing Element,” *SPIE 44th annual meeting: SPIE*, vol. 3790, Denver, Colorado, July 23, 1999.

15 Sangwook Han, Junwan Kim, Youngsoo Sohn, and Dean P. Neikirk, “Design of Infrared Wavelength-Selective Microbolometers Using Planar Multimode Detectors”, Electronics Letters, vol. 40, Issue: 22, pp. 1410-1411, 28 Oct. 2004.

16 W. W. Salisbury, “Absorbent body for electromagnetic waves,” U. S. Patent 2 599 944, June 10, 1952.

17 R. A. Wood, “High-performance infrared thermal imaging with monolithic silicon focal planes operating at room temperature,” Electron Devices Meting, 1993. Technical Digest., International, 5-8 Dec. 1993, pp. 175-177.

18 J. T. Caulfield, “Next generation IR focal plane arrays and applications,” Applied Imagery Pattern Recognition Workshop, 2003. 32nd Proceedings, 15-17 Oct. 2003

19 D. P. Neikirk, D. B. Rutledge, and W. Lam, "Far-Infrared Microbolometer Detectors," *International Journal of Infrared and Millimeter Waves*, vol. 5, 1984, pp. 245-277.

20 C. A. Balanis, *Antenna Theory: analysis and design*, John Wiley & Sons, Inc., 1997.

21 D. B. Rutledge, and S. E. Schwarz, “Planar multimode detector arrays for infrared and millimeter-wave application,” *IEEE Journal of Quantum Electronics*, vol. QE-17, no. 3, Mar. 1981.

22 R. L. Eisenhart and P. J. Khan, “Theoretical and experimental analysis of a waveguide mounting structure,” *IEEE Trans. Microw. Theory Tech.*, 1971, MTT-19, pp 706-719.

23 D. M. Pozar, *Microwave Engineering*, Addison-Wesley, 1993.

24 www.ansoft.com

25 S. W. Han and Dean P. Neikirk, “Design of Infrared Wavelength-Selective Microbolometers Using Planar Multimode Detectors”, *Proceedings of SPIE*, vol. 5836, ‘Smart Sensors, Actuators, and MEMS’, SPIE Europe International Symposium on Microtechnologies for the New Millennium 2005, Sevilla, Spain, May 9-11, 2005, pp. 549-557.

26 A. J. Stead and M. Missous, “Multicolour infrared detection with $In_{0.1}Ga_{0.9}As/A_{10.33}Ga_{0.67}As$ double and triple-coupled quantum well infrared photodetectors,” High Performance Electron Devices for Microwave and Optoelectronic Applications Symp. (EDMO), London, UK, Nov. 1999, pp. 119-124.

27 Y. Zhengmao *et al.*, “A normal-incidence InAs self-assembled quantum-dot infrared photodetectors with a high detectivity,” *IEEE J. Quantum Electron.*, 2002, 38, (9), pp. 1234-1237.

28 H. Hara, N. Kishi, and H. Iwaoka, “Silicon bolometer and micro variable infrared filter for CO_2 measurement,” Optical MEMS. 2000 IEEE/LEOS Int. Conf., Rio Grand, Puerto Rico, Aug. 2000, pp. 139-140.

29 T. R. Schimert *et al.*, “Low-cost low-power uncooled 120x160 a-Si-based microinfrared camera for law enforcement applications”, *Proc. SPIE*, vol. 4232, pp. 187-194, Feb. 2001.

30 S. J. Yoo, *Micromachined wavelength selective microbolometer sensors operating at room temperature*, PhD. Dissertation, The University of Texas at Austin, Dec. 2000.

31 J. W. Kim and D. P. Neikirk, "Infrared wavelength selective micromachined microbolometers," *Proc. of SPIE*, vol. 5116 Smart Sensors, Actuators, and MEMS, SPIE's First International Symposium on Microtechnologies for the New Millennium 2003, Maspalomas, Gran Canaria (Canary Islands), Spain, May 19-21, 2003, pp. 514-522.

32 http://www-lep.gsfc.nasa.gov/code693/tdw03/proceedings/docs/session_2/Ngo.pdf

33 J. M. Johnson, Y. Rahmat-Samii, “Genetic algorithm optimization for aerospace electromagnetic design and analysis,” IEEE Aerospace Applications Conference, 1996. Proceedings., 1996, vol. 1, 3-10 Feb. 1996, pp. 87-102.

34 E. Michielssen, J. M. Sajer, S. Ranjithan, R. Mittra, “Design of lightweight, broad-band microwave absorbers using genetic algorithms,” *IEEE Transactions on Microwave Theory and Techniques*, vol. 41, Issue 6, June-July 1993 pp.1024-1031.

35 D. S. Weile, E. Michielssen, and D. E. Goldberg, "Genetic algorithm design of pareto optimal broadband microwave absorbers," *IEEE Trans. Electromagnetic Compatibility*, vol. 38, Aug. 1996, pp. 518-525.

36 J. H. Holland, *Adaptation in Natural and Artificial Systems*, Ann Arbor, The University of Michigan Press, 1975.

37 K. A. De Jong, "An analysis of the behavior of a class of genetic adaptive systems," (Doctoral Dissertation, University of Michigan). *Dissertation Abstracts International*, 36(10), 5140B. (University Microfilms No. 76-9381), 1975.

38 Y. Rahmat-Samii and E. Michielssen, *Electromagnetic Optimization by Genetic Algorithms*, John Wiley & Sons, New York, 1999.

39 M. Sundaram, S. C. Wang, M. F. Taylor, A. Reisinger, G. L. Milne, K. B. Reiff, R. E. Rose, R. R. Martin., "Two-color quantum well infrared photodetector focal plane arrays," *Infrared Physics and Technology*, vol. 42, no. 3-5, June, 2001, pp. 301-308.

40 Lin, Jiang, S. S. Li, W. S. Liu, N. T. Yeh, J. I. Chys, "A two-stack, multi-color in 0.5Ga0.5As/GaAs and InAs/GaAs quantum dot infrared photodetector for long wavelength infrared detection," *Infrared Physics and Technology*, vol. 46, no. 3, January, 2005, pp. 249-256.

41 S. M. Kim, J. S. Harris, "Multispectral operation of self-assembled InGaAs quantum-dot infrared photodetectors," Applied Physics Letters, vol. 85, no. 18, Nov 1, 2004, pp. 4154-4156.

42 Gunde, M. Klanjsek, Macek, M., "Infrared optical constants and dielectric response functions of silicon nitride and oxynitride films," Physica Status Solidi (A) Applied Research, vol. 183, no. 2, Feb, 2001, pp. 439-499.

43 W. H. Emerson, “Electromagnetic wave absorbers and anechoic chambers through the years,” *IEEE Trans. on Antennas and Propagation*, vol. AP-21, no. 4, July 1973.

44 G. J. Hawkins, “Spectral Characterisation of Infrared Optical Materials and Filters”, PhD Thesis, The University of Reading, Department of Cybernetics, 1998.

45 Y. Wang, B. Potter, M. Sutton, R. Supino, and J. Talghader, “Step-wise tunable microbolometer long-wavelength infrared filter,” TRANSDUCERS '05 - 13th International Conference on Solid-State Sensors and Actuators and Microsystems, Seoul, Korea, June 5-9 2005, pp.1006-1009.

Vita

Sangwook Han was born in Daejon, Korea (Republic of Korea) on February 28, 1974, the son of Dal-Soo Han and Soon-Ja Bae. After graduating from Chamshil High School, Seoul, Korea, he attended Hongik University, Seoul, Korea, in 1993. He graduated with a Bachelor's degree in Radio Science and Communication Engineering in 1999, and wed Jinhee Lee in May of 2000. In September, 2000, he entered the Graduate School of The University of Texas at Austin. He received the degree of Master of Science in Electrical and Computer Engineering in December of 2001, and was admitted to candidacy in the Doctoral program at the University of Texas at Austin in October 2004.

Permanent address: 4600 Seton Center Pkwy. #518, Austin, TX 78759
This dissertation was typed by the author.